CONTROLLING NANOPARTICLE MORPHOLOGIES IN PARTICLE-LADEN DROPLETS THROUGH ATOMIZATION

A Dissertation

by

SHADI SHARIATNIA

Submitted to the Graduate and Professional School of
Texas A&M University
in partial fulfillment of the requirements for the degree of

DOCTOR OF PHILOSOPHY

Chair of Committee,	Dorrin Jarrahbashi
Co-Chair of Committee,	Amir Asadi
Committee Members,	Waruna Kulatilaka
	Iman Borazjani
	Mohammad Naraghi
Head of Department,	Guillermo Aguilar

December 2021

Major Subject: Mechanical Engineering

ABSTRACT

Achieving desired nanoparticle (NP) morphologies upon evaporation of particle-laden droplets is very challenging due to the complex behavior involving particle-particle, particle-substrate, and particle-fluid interactions. Controlling the patterns of deposited NPs can be exploited to fabricate tailored nanostructures that add functionality and engineer the properties of the manufactured components. Nanoparticle spray deposition is an effective method of delivering particle-laden droplets that place desired particles on substrate. This technique finds numerous applications in electronics, food, drug, manufacturing, and energy industries. Various spray deposition techniques such as spray drying, thermal, and electrosprays are common practice for NP deposition. However, they all lack the required precision in controlling the droplet attributes as atomization is inherently a random process. In addition, NPs tend to accumulate along the pinned droplet contact lines during droplet evaporation, a phenomenon known as the coffee ring effect (CRE). Eliminating or exploiting CRE requires costly and multi-step processes. Moreover, NPs of interest in engineering applications are typically hydrophobic and tend to agglomerate in water, and thus cannot be directly sprayed. A novel nanoparticle spray deposition system is designed and built by integrating supercritical CO_2 assisted atomization of aqueous nanoparticle suspensions. The supercritical CO_2 boosts liquid atomization by reducing the liquid surface tension and enabling dissolved gas atomization mechanisms. The combined effects results in controllable creation of micron-size droplets with a narrow size distribution that directly affect the evaporation rate which in turn dictates the NP self-assembly mechanism. A nanoparticle-agnostic approach is introduced that allows the fabrication of multi-material nanostructures with precisely engineered patterns. Evaporative droplets of aqueous suspensions of Carbon Nanotubes, Graphene

Nanoplatelets and Boron Nitride Nanotubes representing NPs of different elemental composition, sizes and shapes are investigated. Cellulose nanocrystal (CNC) is used as a platform to make hybrid systems of CNC and the secondary NP. Fundamental understanding of repulsive-attractive interactions in this hybrid system is capitalized to explain their effects on the final pattern. It is shown that formation and thickness of deposited patterns of CNC-bonded NPs after evaporation of droplets depends only on the concentration and mass ratio of the NPs and not their shape and size or NP.

DEDICATION

To my loving husband, Hasan, for his unconditional love, constant support, patience, guidance, and encouragement!

ACKNOWLEDGEMENTS

I would like to thank my committee chair, Dr. Jarrahbashi, and my committee co-chair, Dr. Asadi, who have been amazing mentors to me. Besides their deep knowledge in various aspects of my research, their passion for solving challenging problems has constantly inspired me during my PhD. They give their students a lot of freedom in their research, which in turn nurtures self-esteem and creativity. Their great support and constant encouragement meant so much to me and I will be forever grateful to them.

I would also like to thank the time and help of my committee members Dr. Kulatilaka, Dr. Borazjani, and Dr. Naraghi. Their feedbacks and recommendations have significantly improved the quality of my dissertation.

I would like to extend my gratitude to the Department of Mechanical Engineering at Texas A&M University for supporting my doctoral studies through various Fellowships and Scholarships and resources that one can only find in a top U.S. university. I appreciate the help of staff members in Material characterization and AggieFab nanofabrication facilities, as well as Microscopy and imaging center for training and helping me with my experiments. I am also grateful to my amazing friends and colleagues with whom I have shared wonderful memories, and who have always been there to support and encourage me.

Finally, my deepest gratitude goes to my beautiful family, Zohreh, Hasan, Shabnam, Omid and the other Hasan (!) for their unconditional love, support, and encouragement. None of this would have been possible if it wasn't for them.

CONTRIBUTORS AND FUNDING SOURCES

Contributors

This work was supervised by a dissertation committee consisting of Professors Jarrahbashi [advisor], Kulatilaka, and Borazjani of Mechanical Engineering, and Professor Asadi [co-advisor] of Department of Engineering Technology and Industrial Distribution, as well as Professor Naraghi of Department of Aerospace Engineering. All the work conducted for this dissertation is completed by the student independently.

Funding Sources

Graduate study was also supported by several fellowships and scholarships from Texas A&M University.

NOMENCLATURE

a	Acceleration
A	Area
Bo	Bond Number
C	Correlation coefficient
Ca	Capillary Number
C_v	Saturated water vapor concentration
D	Diffusion coefficient
D_{32}	Sauter Mean Diameter
D_S	Surface Diameter
D_V	Volume Diameter
DV_{10}	10% cut-off point of volume-based size distribution
DV_{50}	50% cut-off point of volume-based size distribution
DV_{90}	90% cut-off point of volume-based size distribution
E’	Storage modulus
f	Focal Length
g	Gravitational acceleration
H	Relative humidity
h_0	Initial droplet height
I_{Max}	Maximum light intensity
I_{Min}	Minimum light intensity
K	Wavenumber
L	Characteristic length

M	Modulation
$\dot{m}$ (t)	Evaporation rate of droplet
Oh	Ohnesorge number
P	Pressure
Pe	Peclet number
P_{inj}	Injection pressure
R	Contact line radius
r	Droplet radius
Re	Reynolds number
T	Temperature
t	Time
Tanδ	Ratio of the loss to the storage modulus
T_g	Glass transition temperature
T_{inj}	Injection temperature
t_σ	Capillary breakup time
u_l	Ligament velocity
v	Velocity
V	Volume
We	Weber number
Wt%	Weight percent
λ_{jet}	Wavelength of jet instabilities
λ_l	Wavelength of ligament instabilities
λ_{RT}	Wavelength of Rayleigh-Taylor instabilities

ρ_g	Density of gas
ρ_l	Density of liquid
θ	Droplet contact angle
λ	Wavelength of instabilities
μ	Viscosity
ξ	Zeta potential
ρ	Density
σ	Surface tension
ω	Temporal growth rate

TABLE OF CONTENTS

LIST OF FIGURES

LIST OF TABLES

1. INTRODUCTION

1.1 Objectives

Nanofabrication processes for constructing engineered nanostructures with specific properties and functionalities form the foundation of nanomaterials research with various applications in electronics, [1-4] pharmaceuticals and healthcare, [5-7] energy harvesting and storage, [8-10] sensing, [11, 12] coatings, [13-15] and many more. Nanofabrication techniques generally divide in top-down and bottom-up categories. [16, 17] Photolithography, [18, 19] including UV, [20-22] focused ion beam (FIB), [23-25] electron-beam, [26, 27] and X-ray lithography, [28-30] FIB milling, [31, 32] nanoimprint lithography 35-39 (stamping), [33-37] dip-pen nanolithography, [38-40] and scanning probe lithography [41, 42] are among the primary top-down nanofabrication techniques. These methods are specifically used for planar structures (e.g., chip making) with features of micro/nanoscale resolution, depending on the wavelength of the source beam, and are not suitable for complicated 3D geometries. Bottom-up nanofabrication techniques are based on the self-assembly of unit compounds that use physical and chemical forces available to form larger structures. [43] Atomic layer deposition, [44-46] chemical [47, 48] and physical vapor deposition, [49, 50] sol-gel, [51, 52] and DNA scaffolding [53, 54] are among the most prominent bottom-up nanofabrication methods.

Self-assembly which is the backbone of bottom-up fabrication techniques is the result of random collision of components within a solvent that reach an equilibrium state. [55, 56] This equilibrium can be either static or dynamic. [57, 58] Static systems, which might need some initial formation energy like stirring, sonication or heating, reach a local/global stability state, when no further energy is being dissipated, and remain in that state. Dynamic self-assembly systems on the

other hand, form structures/patterns while the system is dissipating or receiving energy and the structure disassembles when the flux of energy is removed. [59] In a self-assembly process, the repulsive and attractive interactions between components, which can be molecules, functional groups, colloids, etc., should be 'weak' enough such that undesired interactions easily detach, and allow the system to probe various possible arrangements and gradually identify the optimum configuration among different components with least amount of free energy. [60] Van der Waals, π-π, charged and polarized bonds are among the 'weak' interactions that enable the assembly and are preferred over 'strong' coulomb interactions, covalent, conventional ionic, metallic and hydrogen bonds. The small components, nanoparticles (NPs) or colloids, involved in self-assembly have a large surface to volume ratios that make surface chemistry an important property with a defining role in the final structure. Mass and shape of the particles that are dissolved in a solvent, as well as chemical, electrical and magnetic properties of these particles play a critical role in formation of the final assembly.

Achieving desired functionality and performance through bottom-up nanofabrication is still a challenge. The main objective of this research is deep understanding of nanoparticles interactions and their properties in defining the final structure that unravels the knots of unknowns for advancement of bottom-up fabrication and enables programming of smart and efficient self-assembly systems. In addition to this fundamental understanding, developing a high throughput particle-laden droplet creation and delivery system to scale up the deposition and nanostructure engineering process is needed. This is the second main objective of this work that will be elaborated on in the next sections.

1.2 Literature Review

Deposition of NPs and self-assembly of nanostructures through evaporation of particle-laden droplets is the basis of many manufacturing techniques such as inkjet printing and coating. [61, 62] However, as depicted in **Fig. 1(a)** in this process NPs tend to accumulate along the edge of the droplet due to a capillary flow (illustrated in **Fig. 1(b)**) from the center toward the pinned contact line of droplet as evaporation over the surface advances; a phenomenon known as the coffee ring effect (CRE). [63] This capillary flow from the center of the droplet towards the contact line initiates to compensate the mass loss at the droplet's periphery. [63] This flow drags the particles and accumulates them along the edge of the droplet leaving a ring-shaped trace of particles on the substrate [64] that varies with shape, size and chemistry of the particles, as well as the operating conditions during evaporation. [64, 65] The state-of-the-art methods of eliminating or exploiting the CRE requires costly and multi-step processes such as imposing an external force (electrical, thermal, magnetic, sonic, etc.), addition of surfactants, and chemical manipulation of particle/substrate. [66, 67] In addition, these methods are strongly dependent on the shape and type of the NPs. Nanoparticle-agnostic process to control the fabrication of tailored nanostructures through evaporation of nano-colloidal droplets is still missing and fundamental understanding of the interactions of nanoparticles with each other is required to fill this knowledge gap.

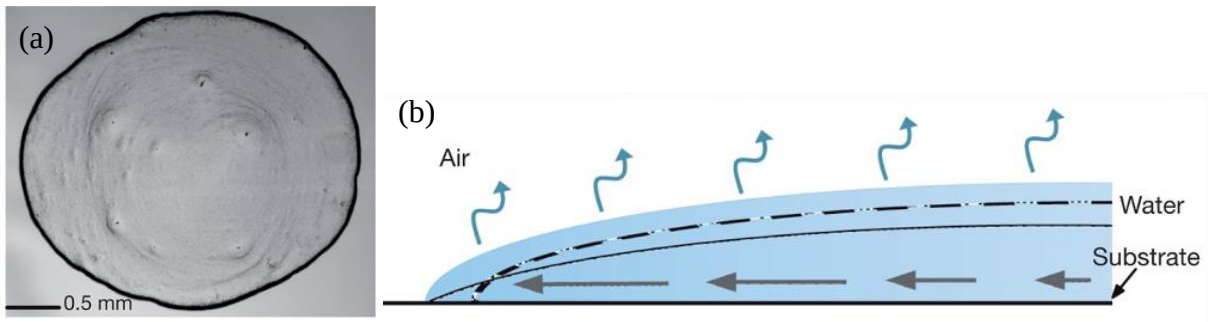

Figure 1. (a) Final distribution of particles upon evaporation of the solvent. (b) Schematic illustration of the capillary flow from the center of droplet towards the pinned edge of droplet as evaporation advances over the surface area. Reprinted with permission from [68].

Deposition of nanoparticles via spray atomization and self-assembly of nanoparticles upon evaporation is one of the main deposition techniques with several practical applications in food, [69-71] drug delivery, [72, 73] manufacturing, [74, 75] energy, [76-78] electronics, [79, 80] and surface coating. [15] Spray deposition is a simple one-step, safe and low-cost method for coating large surface areas within few seconds which promotes the efficiency and scalability, while reducing materials usage. In nanoparticle spray deposition, a colloidal suspension is atomized to create droplets containing nanoparticles of interest that subsequently evaporate and leave the particles on the target surface. Various configurations of thermal sprays, [81-83] electrical sprays, [84, 85] inkjet printing, [62, 86-88] and aerosol jet printing [89, 90] are among the most common spray deposition methods that have been extensively studied.

Thermal spray systems such as warm, [91, 92] plasma, [93-95] and electrical sprays [96, 97] are among the most popular thermal spray coating techniques that use a heat source, either through chemical reaction, plasma discharge, or electricity to melt the feedstock material and spray them on a substrate using a high-speed jet. **Figure 2** shows a schematic illustration of a thermal spray coating system. [81] Cold spray systems where solid powders (rather than a melted material)

are accelerated in a de Laval nozzle towards the substrate, falls under thermal spray category as well. [82] Due to the harsh conditions in these sprays, coatings as well as substrates are limited to materials that can withstand large impact forces and are compatible with high temperature (and/or temperature gradients). [98] Metals and metallic alloys, ceramics, glasses, polymers and plastics are commonly used as the coating material in such systems. [82] These coatings are often utilized to prevent chemical and mechanical damage to different structures depending on the functionality of the part. [99] Thermal sprays are very cost effective and can cover large surface areas in a short period of time with a thickness that can range from ~20 micrometers to several millimeters. [100] However, thermal methods lack the precision needed for coatings in micro/nanometer scales. [97]

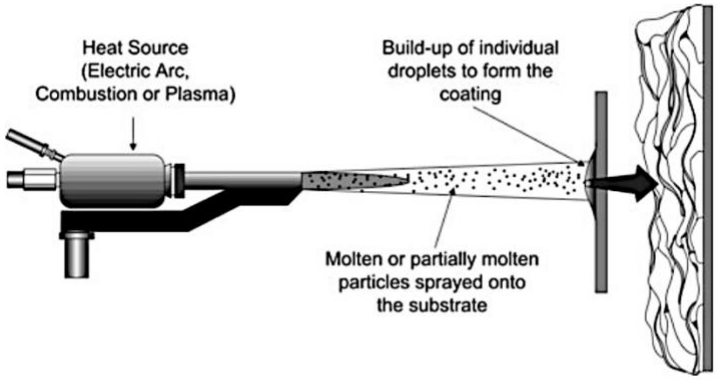

Figure 2. Schematic illustration of thermal spray coating system. Reprinted with permission from [81].

Inkjet printing (IJP) is a precisely controlled technique that is utilized for depositing colloidal droplets on a targeted location. [62, 101] IJP finds numerous applications in electronics [102-107] and life sciences. [108-110] The contact line of the ink droplets that are printed pins to the substrate. As the droplet evaporation advances, the contact angle between the droplet and substrate decreases. As a result, the coffee ring effect (CRE) can occur that can be exploited or

suppressed to enforce a specific particle pattern on the substrate depending on the application. [63] **Figure 3** indicates the application of IJP in depositing a CNT nanowire that can be used in electronic circuits. *[86]* Suppression of the CRE requires costly and multi-step processes such as the use of flammable, toxic and hazardous surfactants to the solvent, [66, 111, 112] physical and chemical modification of the substrate, [113, 114] and imposing external electrical, magnetic or acoustic forces. [115-117] In addition, IJP is limited to deposition of a single or a few droplets at a time that covers a small surface area which limits the scalability of this technique.

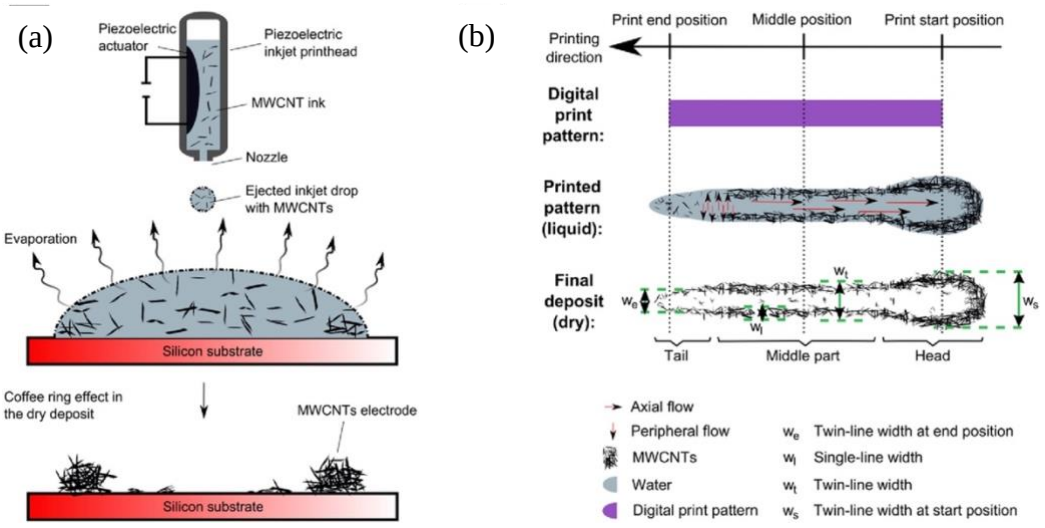

Figure 3. (a) cross-sectional and (b) top view of a twin line CNT nanowire deposition through inkjet printing. Reprinted with permission from [86].

Aerosol jet printing (AJP) utilizes an air-assisted atomization technique for breakup of a liquid jet stream and a specific directed nozzle for targeted deposition. [118] This technique is faster than IJP and is compatible for deposition on any substrate and capable of handling a wide range of materials in moderate operating conditions (i.e., low temperatures and pressures). [119]

It provides precise control over thickness/profile of deposition on one go, and by having multiple feed lines to the same nozzle, material selection can be on-demand for each deposition site at the same print. Multiple process parameters (i.e., nozzle geometry, injection pressure and temperature, working distance) make this technique more complicated, but also enable customization of the final print. [120] However, the internal design of the nozzle directly affects the quality and dimensional resolution of the print and is often times very complicated to accurately focus the jet. [121] While AJP is superior to IJP in printing straight lines, they still lack the required precision in printing single dot/square sites. [122] Solubility of different particles in the solvent and controlling droplet sizes are other challenges of this method. Although AJP is a faster process compared to IJP, it is still not appropriate for large scale printing/deposition. [123]

Spray atomization, which is used as the delivery method of nanoparticle deposition in our work, is a critical element in several practical applications in combustion of liquid fuels, [124] energy systems, [125] materials processing, [126] electronics, [80] and pharmaceuticals. [127] Atomization of a liquid jet into multiple small droplets upon injection into a quiescent gaseous medium encompasses primary and secondary breakup mechanisms. The former involves the growth of the interfacial instabilities very close to the nozzle that results in formation of ligaments and droplets. [128] The secondary atomization is referred as the additional fragmentation of droplets that results in creation of even smaller droplets at distances further away from the injection nozzle. [129]

In the gas-assisted atomization systems [130] where a secondary fluid (mainly gas) is used to generate sufficient shear to break up the main liquid jet, the atomization mechanisms become more perplex. These systems typically involve injection of a two-phase bubbly flow or a fluid that

contains dissolved gas through a twin-fluid atomizer. Air-blast atomization systems, effervescent, [131] and dissolved-gas atomization [132] are among the most common twin-fluid atomization mechanisms that have been extensively studied. Flash-boiling is another atomization mechanism that rather than using two fluids, exploits the phase change of a single fluid during the injection process. [133] Atomizer design indicates whether the interaction between the liquid and atomizing gas occurs within the atomizer body, as in internal mixing, or outside the atomizer as in external mixing mode. [134] In the internal-mix atomizers, the two fluids enter separately and interact in the mixing chamber to form a two-phase flow before exit from the orifice. The characteristics of the two-phase fluid such as liquid/gas type, viscosity, surface tension, and particularly gas-to-liquid ratio (GLR) have a profound effect on the atomization outcome. In an external-mix two-fluid atomizer, the mixing of gas and liquid occurs outside of the nozzle head. The liquid flow is usually in the center and the gas comes in contact with the liquid concentrically to promote the breakup. [135] These atomizers are specifically useful for liquids that would otherwise evaporate in internal mix chambers. [136]

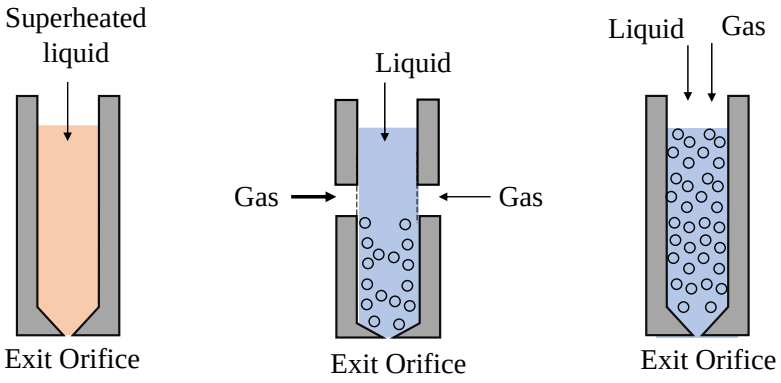

Figure 4. Schematic illustration of (a) flash-boiling, (b) Effervescent, and (c) Dissolved-gas, atomization systems.

Dissolved-gas atomization, where the atomization gas is dissolved in the liquid before injection, takes advantage of the solubility of the atomizing gas in the liquid that further emerges as bubbles that expand and explode downstream of the orifice and by imposing a relatively large force, promote the liquid breakup. [137] Dissolved-gas atomization is specifically useful in micronization [138] and powder generation applications [139] where a solution that contains solid particles of interest is atomized and micron/submicron powders are created after droplet evaporation. Many studies have shown the considerable effect of the nozzle design and geometry as well as rheological and chemical properties of the solvent on the final size of the droplets created by this method. [140] The efficiency of this system strongly depends on the solubility of the atomizing gas in the liquid that can impose a constraint on material selection and operating conditions as the solubility is strongly dependent on the system pressure and temperature.

Possessing hybrid gas-like and liquid-like properties, supercritical fluids offer many advantages that make them a plausible candidate for assisting atomization. Their sensitivity to slight changes in temperature and pressure along with low viscosity, high density, and high diffusivity results in an enhanced gas dissolution in liquid and lower surface tension before injection. [141] Particularly, in micronization and powder manufacturing applications involving dissolution of solid particles in a specific supercritical solvent, low solubility and possible decomposition of solid particles in the solvents impose limitations and make the material selection a crucial part of designing supercritical fluid atomization systems.

Supercritical CO_2 (SCO_2) is a viable candidate used to assist atomization as it is highly miscible in water and most organic solvents. In addition, it is non-toxic, degradable,

nonflammable, and abundant and has a moderate critical temperature (31.7 ºC) and a relatively low critical pressure (7.38 MPa) that extend its application to temperature-sensitive applications as in biotechnology and pharmaceutical industries. [142] Depending on the phase behavior and solubility of the material to be atomized in the supercritical medium, supercritical fluid atomization systems fall under various categories. [143] Among them, supercritical-assisted atomization (SAA) has been shown to generate very fine particles with desired morphology and more uniform size distribution. [144] SAA is a technique originally invented by Reverchon [145] for controlled fabrication of micron and nano-size solid particles through atomization of a ternary mixture comprised of SCO_2, organic/inorganic liquid solvents, and solid solutes. **Figure 5** schematically shows this system. The mixture is injected into a temperature-controlled precipitator that is equipped with a stream of warm gas to promote the evaporation of solvent droplets and a stainless-steel frit is deployed at the bottom of the atomizer to collect the nano-size dry powders for later use. The SAA technique allows for sufficient contact between SCO_2 and liquid suspension before injection that maximizes the dissolution of SCO_2 in the liquid solvent and leads to surface tension reduction. The combined effects result in formation of fine droplets with narrow size distribution that makes SAA a viable method for dry powder fabrication with tremendous applications in food, pharmaceutical, and chemical industries. [146]

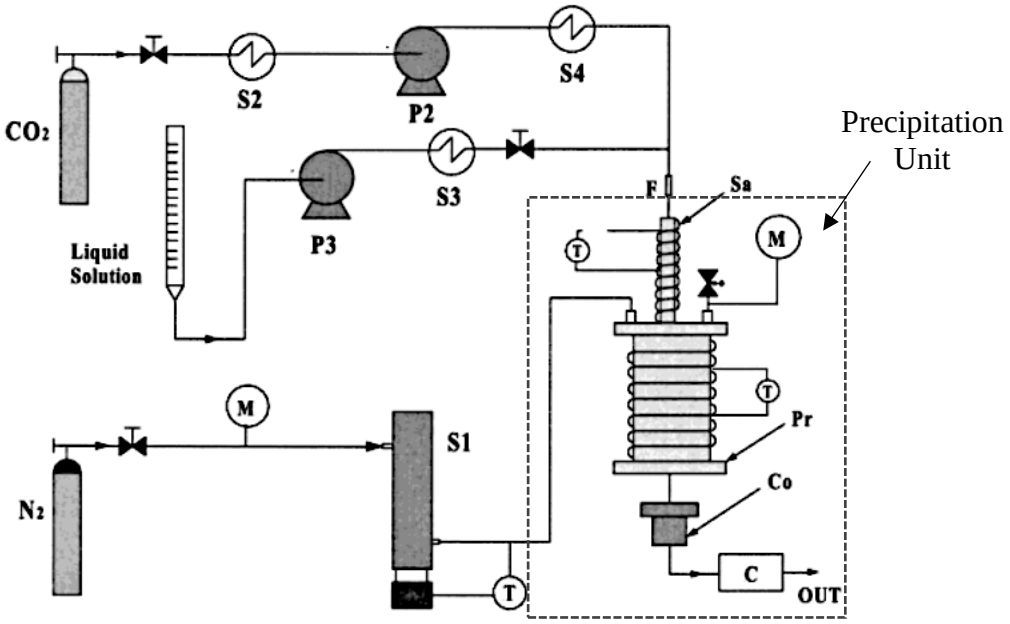

Figure 5. Schematic illustration of supercritical assisted atomization (SAA) system developed for fabrication of dry powder. Reprinted with permission from [147].

There are several experimental studies on gas-assisted atomization including effervescent [148] and dissolved-gas atomization systems [149] that focuses on the relationship between the primary break up regimes and the governing non-dimensional parameters driving the instability mechanisms [150, 151] and their effects on the ligament structures, spray formation and spatio-temporal distribution of the droplets. [152] However, these studies did not involve the dissolution of supercritical fluid in the liquid. The most relevant reports on resolving the SCO_2-assisted atomization mechanisms are reported by Reverchon et al. [153] They used SCO_2 and N_2 as dissolved gases to assist the atomization of water and ethanol and studied the effects of spray parameters such as GLR, injection pressure, nozzle diameter and axial distance from the injection nozzle on the mean droplet sizes measured by means of a laser diffraction technique. The authors suggested that SCO_2 promoted jet breakup through two simultaneous effects: (1) the dissolved-gas

atomization since a fraction of SCO_2 dissolves in the liquid and (2) the effect of undissolved CO_2 that squeezes the liquid ligaments. The combined effects accommodate achieving fine droplets with a narrow size distribution. [153] However, no evidence of such behavior was reported in these studies and the underlying atomization mechanisms behind the promotion of the flow instabilities leading to ligament breakup were not revealed. In addition, the effect of rheological properties of the atomization gas and the liquid mixture on the final droplet sizes have not been investigated to date. One of the objectives of this study is to unravel the role of dissolved supercritical fluid and its thermophysical properties on promoting the jet instabilities to pinpoint the breakup mechanisms governing the SAA.

Several analytical models in the literature predict the final Sauter mean droplet sizes (SMD) for the general air-assisted (twin-fluid) atomizers as well as specific models for effervescent atomization systems. [154, 155] These models are mainly focused on certain nozzle geometries or specific experimental conditions. Lund [156] was a pioneer in developing a predictive model for SMD using near-nozzle images of an effervescent atomization system. They adopted the maximum growth rate equation based on Weber's instability analysis for jet breakup, [157] which showed a good agreement with their experimental measurements. The unstable wavelengths in this analysis are only a function of fluids' properties (i.e., density, surface tension, viscosity). However, their model suffers from neglecting two important effects: (1) the relative velocity between the gas and liquid phases and (2) the secondary breakup. Sutherland et al. further improved this model by considering the aerodynamic effect of the gas surrounding a ligament and the relative velocity between the gas and liquid phases. [158] They obtained the wavelength of the fastest growing disturbance from the instability analysis developed for a capillary jet by Sterling and Sleicher [159]

that takes the aerodynamic interaction between the jet and the surrounding medium into account; however, the secondary atomization was not considered in that model. To surpass the shortcomings of the existing models, CFD simulations using particle tracking methods have been employed to obtain SMD for the effervescent atomization systems. [160] Even though the analytical and numerical SMD prediction models for effervescent atomizers differ in their scope and range of application, they all signify the important role of surface tension and density on SMD for a wide range of GLRs while they agree that droplet sizes are not very sensitive to the liquid viscosity. However, to the best of our knowledge, there is no analytical, empirical, or numerical model specifically developed to predict the SMD resulted from the dissolved-gas atomization, and particularly for supercritical-assisted atomization. Based on the experimental results, we develop an empirical SMD prediction model that can be used for validating future numerical models developed for dissolved gas atomization. To accomplish these objectives, we designed and built an SAA system and resolved the jet breakup and spray characteristics via utilizing different optical diagnostics. For this purpose, the spray formation process using either CO_2 or Nitrogen (N_2) as the atomization fluid is portrayed via shadowgraphy and laser diffraction techniques. Furthermore, we leverage the linear instability analysis to delineate the dominating instability mechanisms at different flow conditions.

Despite plethora of studies on nanoparticle deposition using evaporative droplets in the literature, there are several knowledge gaps that impose limitations in the main two parts of this process and motivated the current research: (*i*) Carrier Agents: creation and delivery of fine and homogenously sized particle-laden droplets to a substrate, and (*ii*) Pattern Engineering: controlling

the self-assembly of nanoparticle during evaporation to tailor the final deposition pattern that is left on the substrate.

(i) Carrier Agents: There are several spray-based techniques to create and release nanoparticles through atomization of colloidal solutions, such as spray pyrolysis [161] and spray drying [162] that are widely used in manufacturing, pharmaceutical and food industries. [7, 163, 164] Their adoption is owed to the compatibility of these techniques with large variety of materials and their high throughputs. However, due to the inherent uncertainties, randomness and wide size distribution of droplets created by atomization, these systems lack the precision and control over the formation and homogeneity of produced nanoparticles. [165] To overcome these limitations, supercritical assisted atomization (SAA) has been introduced as a method that utilizes a gas above its thermodynamic critical point to assist the atomization process. [166] Although SAA provides great control over process parameters, it is limited to solely manufacturing of micro/nanoparticles that are collected in a precipitator in the form of dry powder after atomization. A potentially important application of SAA is the direct deposition of nanoparticle-laden droplets resulting from atomization of nano-colloidal suspensions exposed to SCO_2 on a substrate. However, due to complex underlying atomization mechanisms in a dissolved supercritical fluid assisted system, this potentially important application has not been explored in the literature to date.

(ii) Pattern Engineering: Although self-assembly of nanoparticles comprises the core of bottom-up fabrication techniques, an effective procedure to control and program this process has not been developed yet. Water is one of the most important solvents used for self-assembly; and the tendency of particles to attract or repel water molecules (i.e., hydrophilicity or hydrophobicity) is exactly the type of 'weak' interaction that drives the assembly of dissolved NPs. Cellulose

nanocrystals (CNCs) are abundant plant-based (linear chain glucose units, $C_6H_{10}O_5$), biodegradable and spindle-shaped NPs that possess both hydrophilic (hydroxyl and ester) and hydrophobic (hydrocarbons) characteristics. [167] We have utilized this unique amphiphilic property of CNCs to create hybrid nanoparticle systems (HNPS) of CNC and desired NP to engineer self-assembly of evaporative aqueous droplets and eliminate time and cost inefficient lab-scale post processing. Graphene Nanoplate (GNP), Carbon Nanotube (CNT) and Boron Nitride Nanotube (BNNT) are the NPs used to build multi/mono-layer structures, which have various size, shape (nanotube vs. nanoplatelet) and chemical composition (carbonaceous vs. ceramic). CNC is exploited as a platform that can alter amphiphilic degree and surface charge of the nano-colloids dissolved in water, which in turn controls the Van der Waals interaction between nanoparticles as well as their attractive/repulsive forces with the solvent and substrate and the final pattern left after evaporation.

As a result, this research dives deep into (1) fundamental understanding of underlying jet breakup and spray formation mechanisms of SAA system as a novel and scalable method of creating and delivering fine and homogenously sized droplets; and (2) principals of evaporation induced self-assembly of nanoparticles and engineering the pattern of deposited nanostructures. The proposed spray deposition technique has the potential be adopted for several practical applications involving CNCs and other nanoparticles with desired functionalities and properties (i.e., structural, electrical, thermal, etc.) that can be tailored to the requirements of each specific application.

Section 2 demonstrates different experimental setups that have been designed and built for each stage (i.e., $^{(i)}$ feasibility studies, fundamental understanding of SAA, $^{(ii)}$ deposition of CNC

carrier droplets created through SAA, and [iii] morphology of nanostructures fabricated through evaporation induced self-assembly of colloidal droplets) of this research, and discusses diagnostic methods, post processing, materials, and characterization techniques that have been utilized. Section 3 discusses the results of various tests and analysis performed for each stage, while section 4 summarizes the main conclusions and takeaways. Finally, section 5 elaborates on future directions of this research.

2. METHODS AND EXPERIMENTS

2.1 Experimental Setup

Figures 6-9 illustrate different experimental setups that have been utilized in this study. **Figure 6** shows an internal mix air-atomizing spray system integrated with an open-frame 3D printer, to atomize an aqueous suspension of CNC. This setup was used to perform feasibility experiments that will be discussed in Section 3.1. The suspension was delivered to an internal chamber of the nozzle to mix with pressurized and dry air stream using an impeller pump (SCC pumps Inc., IL, USA). The mixture was then injected through a 1 mm-nozzle to form a spray of CNC-carrier liquid droplets that further evaporate and release nanoparticles between adjacent layers of 3D printed ABS parts. Once a layer was printed, the spray system was activated to deposit CNC. All the specimens were printed on a consumer level, desktop 3D printer, LulzBot TAZ6 3D Printer (Colorado, USA). The printing area was enclosed to minimize the environmental effects on the printing process. The printing directions were controlled by editing the parameters in the slicing software. Each specimen was printed at the same position on the bed to ensure uniformity

across all the samples. The bed temperature was set at 110 °C, slightly higher than the glass transition temperature of ABS to increase the adhesion. [168, 169] The extruder temperature was maintained at 240°C to optimize the polymer coalescence, entanglement, and bonding strength. [170] **Table 1** summarizes the test conditions and experimental samples that were prepared using this setup, and Section 3 discusses the result of various tests performed on these samples.

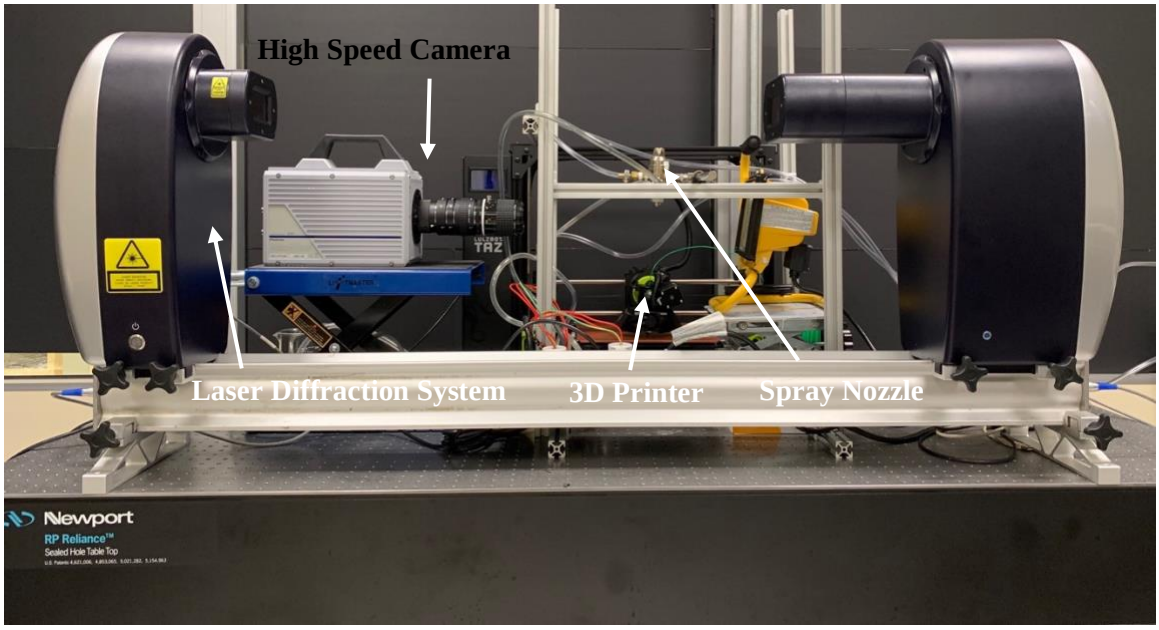

Figure 6. Image of spray coating and diagnostic systems (feasibility study #1)

Figure 7 is schematic illustration of another experimental setup that was utilized for further series of proof-of-concept experiments in collaboration with Georgia Institute of Technology that is elaborated on in Section 3.2. In this system, the aqueous suspension of CNC is delivered to the internal chamber of the nozzle using an impeller pump (SCC Pumps Inc. IL, USA) to be mixed with pressurized and dry air. The tertiary mixture then passes through a single-orifice nozzle to generate micron-sized droplets that further evaporate and deposit CNC particles on glass fibers.

Glass fibers are attached to a flat plate, and a rail-and-motor is used to move them across the spray for the whole length of the fiber to be coated. An Arduino is implemented to control the speed of this axial movement. **Table 2** presents the test cases for these experiments.

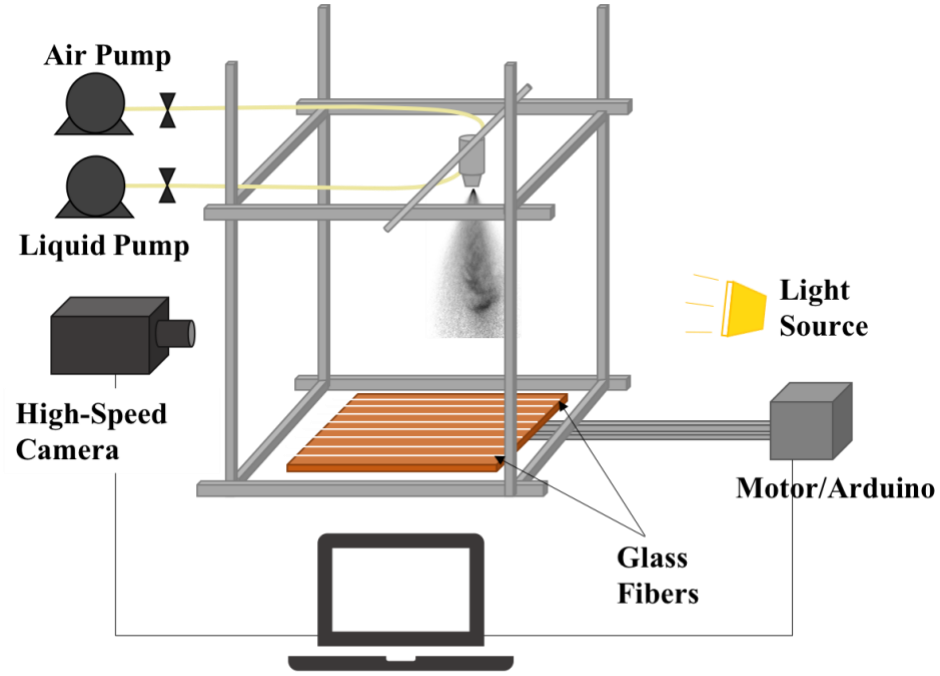

Figure 7. Schematic illustration of spray coating system (feasibility study #2)

Figure 8 illustrates the schematic of spray and optical system used for this study. It consists of three feed lines that deliver CO_2, Nitrogen, and the liquid to a pressure vessel. An HPLC pump (single head, piston pump from Cole-Parmer, IL, USA) feeds the liquid into a pressure vessel (20MPa from Parr Instruments, IL, USA). A dual piston pump (supercritical class from Teledyne SSI, PA, USA) connects CO_2 tank to the pressure vessel and Nitrogen stream from tank is directly connected to the vessel and is controlled by a pressure regulator. Temperature of the mixture in the vessel is also controlled by a heater (Omega Engineering, CT, USA), while pressure is

monitored by several pressure gauges along the feeding lines as well as in the pressure vessel. The multiphase mixture is then injected in ambient condition through a gasoline direct injection (GDI) atomizer (BOSCH, Gerlinger, Germany) with 125 μm orifice. The GDI injector is actuated and controlled using an Arduino that is programmed to operate down to 1 millisecond resolution.

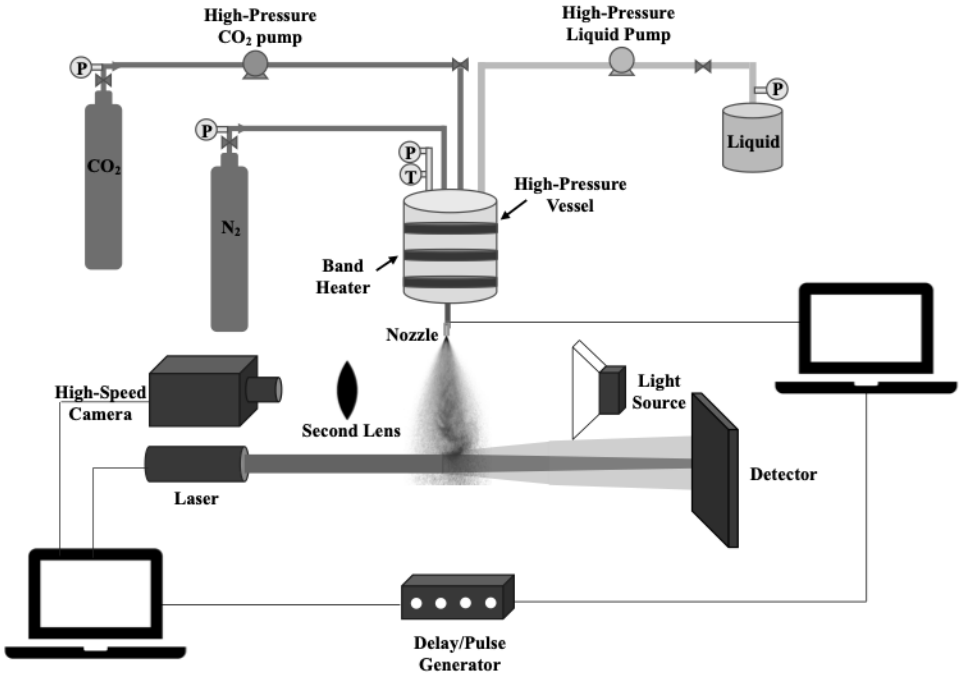

Figure 8. Schematic illustration of SAA system

We employ high speed diffuse back illumination (DBI) (i.e., shadowgraphic) imaging and laser diffraction techniques to probe along the longitudinal and cross-sectional areas of the spray. DBI imaging for direct visualization of the jet is a well-known and nonintrusive technique that provides great information on break-up, liquid penetration length, shape and angle of the spray, [171, 172] especially in a dilute medium. Phase doppler and laser diffraction are among the most commonly used interferometry techniques for droplet size measurement within the cross section

of spray. [173] High velocity, turbulent condition, very small-scale area of interest and the difficulties of finding the appropriate lighting make direct visualization of primary and secondary breakup of a jet challenging. We combine both high-speed imaging and laser diffraction techniques in our characterization measurements to compensate for limitations of each method.

The system allows investigation of spray parameters such as pressure, temperature, and gas to liquid ratio on size and size distribution of the droplets that form, as well as spray dimensions (i.e., liquid core length/width and spray angle). **Table 3** shows different cases that have been studied and the corresponding test parameters.

In order to prepare aqueous suspension of HNPS, CNCs, CNTs, GNPs and BNNTs were dispersed in deionized (DI) water with various concentrations and ratios and probe-sonicated for 2 hours at 20 kHz and 75% amplitude. **Table 4** summarizes all the suspensions that were prepared and tested. For each sample, six droplets were deposited on the glass substrate (micro cover glass No. 1.5) using a 0.1 µL pipette (Eppendorf, Germany). The substrates were thoroughly washed with acetone, isopropanol, and DI- H_2O prior to deposition. Droplet evaporation time was ~16 min at 23˚C ±0.1 and 50% humidity. **Figure 9** schematically demonstrates the preparation of hybrid NPs systems and their deposition on the substrate.

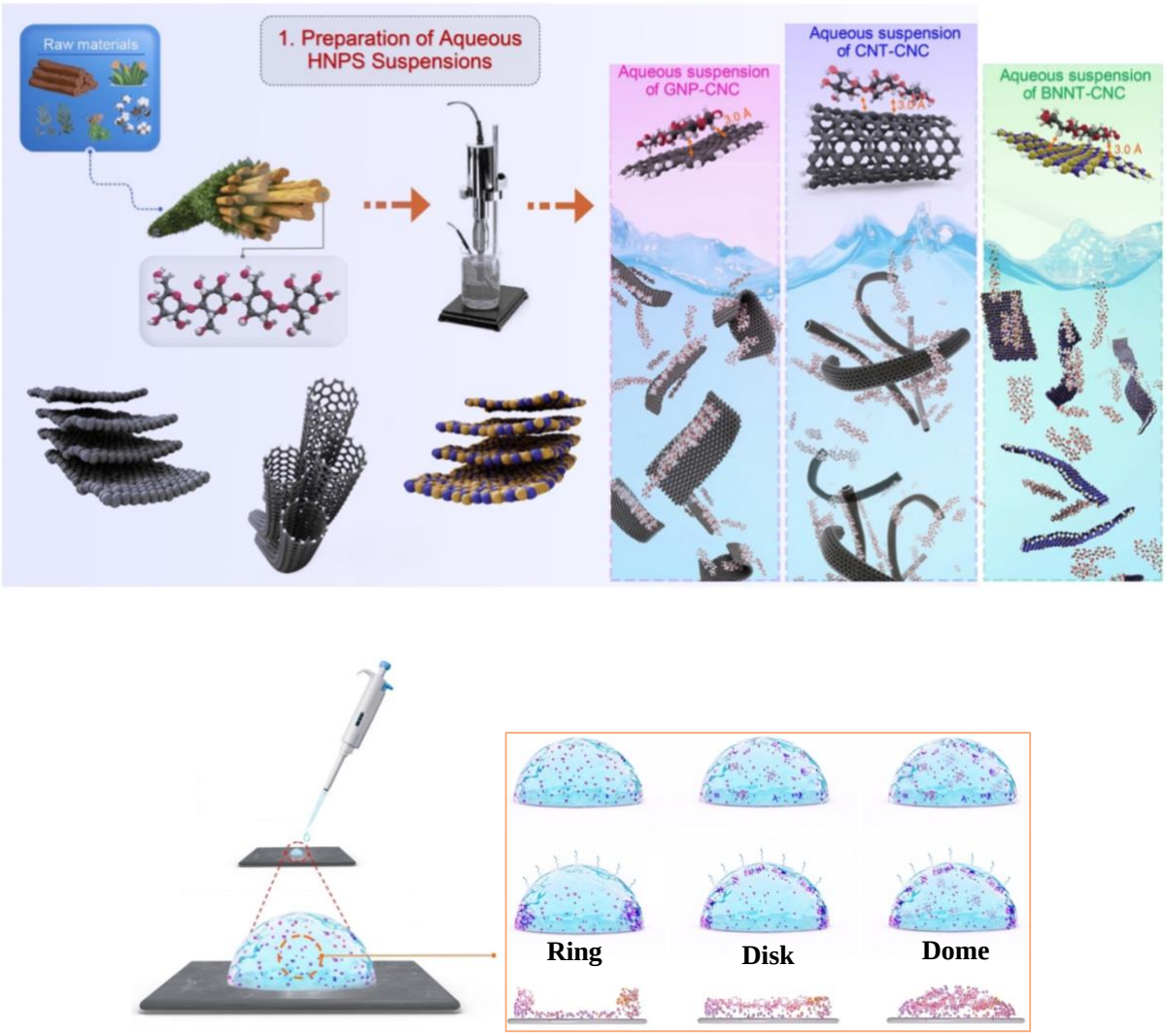

Figure 9. Schematic illustration of fabricating 3D nanostructures. (a) preparation of aqueous suspension of HNPS by sonication; and (b) Deposition of HNPS on substrate to create 3D nanostructures (Ring, Disk, and Dome) upon evaporation of water.

2.2 Spray Diagnostics and Post Processing

High speed images were taken by a Photron Fastcam SA5 camera (CA, USA) equipped with a Nikon Micro lens (Tokyo, Japan) using a high-power LED light source (OR, USA) that is synced with the camera using a Berkeley nucleonics digital pulse/delay generator (CA, USA). The

image processing for background removal, brightness, and gamma factor adjustment, and binarization was developed in R-Studio. The background noise was removed by dividing the intensities of raw image by those of an image taken prior to injection. Binary images were then obtained by imposing a global intensity threshold above which the intensity was set to 1 while the remaining pixel intensities were set to 0. Imaging micron sized features at high velocities during the primary jet break up is challenging and requires high resolving power. Even at high shutter speeds, the field of view gets limited at high magnifications. In order to avoid using costly and complicated microscopic lenses that usually have long working distances and entail additional light sources, a double lens system was deployed. [174] In addition to the macro lens attached to the camera (f = 200 mm) a positive lens (f = 50 mm) was mounted at a focal point distance from the object and aligned with the first lens as illustrated in the schematic. This multi-lens system provides additional magnification, allows for resolving larger field of view and increasing light throughput. [175] The resolving power (RP) of the multi-lens system, which is the smallest feature that the optical system can detect, and an indicative of the system's performance was then calculated to be 20 μm from modulation transfer function (MTF), using a standard resolution test target as follows:

$$MTF = \frac{M_{image}}{M_{object}} \qquad (1)$$

$$M = \frac{I_{max} - I_{min}}{I_{max} + I_{min}} \qquad (2)$$

A Malvern Panalytical's laser diffraction system (Malvern, UK) was deployed for real-time measurements of the droplet sizes in the cross section of the spray at different axial locations with 0.1 μm resolution.

2.3 Materials and Characterization Techniques

2.3.1 Materials

The CNCs used in this work are NCV-100 CNCs (CelluForce, QC, Canada) with diameter of 2.3-4.5 nm and length of 44-108 nm. The pristine GNPs (Sigma Aldrich, Germany) have a length, width and thickness of 5 μm, 15 μm, and 6 nm, respectively. The pristine multi-walled CNTs are NC7000 (Nanocyl, Belgium) produced via catalytic CVD with ~90% carbon purity, average diameter of 9.5 nm, length of 1.5 μm and number of walls of 10. The BNNTs (Bnnano, USA) have an average diameter of 80 nm and a length of 2 μm.

2.3.2 Microscopy

A Leica DM6B (Leica Microsystems Inc., Germany) motorized microscope equipped with 2x-40x objectives is used to study the nanostructured patterns after evaporation of aqueous droplets. Samples were also imaged in polarized light mode in order to capture the crystalline CNCs that are otherwise transparent to brightfield lighting.

2.3.3 Scanning Electron Microscopy (SEM)

A high-resolution focused ion beam (FIB) SEM (TESCAN Ferra-3, Czech Republic) at an acceleration of 5 kV in an in-beam SE mode was used to study the morphology and structure of hybrid nanoparticle systems (HNPS) after evaporation of solvent in droplets. A JCM-5000

NeoScope tabletop SEM at 10 and 15 kV acceleration voltage and high vacuum mode was used to study the fracture surface of 3D printed samples. In addition, LEO1530 SEM at an acceleration of 5 and 3 kV was used to capture the micrograph of freeze-dried CNCs. Prior to imaging, a Cressington plasma sputter was used to apply gold coating on the sample surfaces.

2.3.4 Zeta potential and dynamic light scattering (DLS)

Zeta potential (ζ-potential) and particle size distribution of 0.01 wt% suspensions of hybrid nanoparticles systems (CNC-GNP, CNC-CNT, CNC-BNNT) in DI-H_2O were measured at 25 °C using a Malvern Zetasizer Nano ZS (Malvern Instruments, UK). Suspensions were sonicated for 15 min at 200 rpm prior to measurement to make sure samples were taken from a homogenously dispersed solution. The same instrument was used to measure the hydrodynamic diameter of nanoparticles at a fixed angle of 90° at 25 °C. All experiments were carried out for at least six samples and the average zeta potential and DLS values were reported.

2.3.5 Profilometry

Bruker DektakXT Surface Profiler (Bruker Corp., USA.), which is a stylus-based surface profilometer with vertical resolution of 1 Å, was used to map the nanostructures formed on the surface of the glass substrates after droplet evaporation. All experiments were carried out for at least six samples and the average height profile was reported.

2.3.6 Surface tension and contact angle measurement

Thin films of CNC-GNP, CNC-CNT and CNC-BNNT were prepared by controlled evaporation (in an oven at 180°F for 4 hours) of aqueous suspensions of these hybrid systems on a Teflon substrate attached to a glass slide. Water droplets (of 5μL volume) were placed on these

thin films for contact angle measurements (according to ASTM D7334 standard) using a 22-gauge needle on a KSV instruments CAM 200 goniometer (KSV Instruments, Finland) equipped with a motorized camera and video analysis software. The same instrument was used for pendant droplet surface tension measurements. All experiments were carried out for at least six samples and the average surface tension and contact angle were reported.

2.3.7 Atomic force microscopy (AFM)

Bruker Dimension Icon (Bruker Corp., USA.) with a 0.01-0.025 ohm-cm Antimony (n) doped Si tip and a cantilever of 150kHz frequency and 6 N/m stiffness was used to measure the intermolecular forces among different HNPSs. Force measurements were performed with an HNPS coated tip on an HNPS film in air and water. The tip is coated by immersion in a 5wt% solution of HNPS in water for 1 hour, and HNPS films are also fabricated by depositing the same solution (i.e., 5wt%) dried on a smooth glass substrate. In order to measure the intermolecular forces in water, a large DI-water droplet (~5mL) is placed on the HNPS film prior to approaching the coated tip. All the required accessories and software settings are adjusted for the fluid-immersion force mapping in this mode. All experiments were carried out for at least six samples and the average force was reported.

2.3.8 Electrical resistance measurement

Droplets containing various concentration and ratios of HNPS were deposited on a glass substrate and a Miller FPP-5000 four-point probe (Veeco, USA) was used to measure sheet electrical resistivity of the nanostructures upon evaporation of water. Pure pristine CNT and GNP

were fabricated as a film for comparison measurement as well. All experiments were carried out for at least six samples and the average sheet resistivity was reported.

2.3.9 Thermal stability

Thermogravimetric analysis (TGA) was performed using a TGA Q500 from TA Instruments to study the CNC content deposited on the printed ABS samples. The samples were heated from 40 ℃ to 650 ℃ with a 20 ℃/min ramp in an inert atmosphere. The specific densities of samples were measured using water displacement method according to ASTM D-792. Each data point is at least an average of three measurements.

2.3.10 Dynamic mechanical analysis (DMA)

A DMA Q800 TA Instruments device with a dual cantilever beam clamp was used to perform dynamic mechanical analysis. Storage, rubbery (storage modulus above glass transition temperature) and loss moduli in addition to the glass transition temperature (T_g) were measured in the 25 ℃ to 160 ℃ range at a heating rate of 2 ℃/min and 1 Hz frequency. A preload of 1 N and an initial amplitude of 1 μm were applied on rectangular-shaped (35×15×5 mm) specimens. The printing direction for DMA samples was angle-ply (the default of the printer). Each data point is the average of at least three measurements.

2.3.11 Mechanical testing

The tensile properties of the CNC-ABS samples were determined according to ASTM D638 for dog-bone samples with a gauge length of 50 mm, width of 21 mm and thickness of 3 mm using a Universal United STM testing system equipped with 10 kN load cell at a displacement rate of 2 mm/min. The modulus was calculated between the strain values of 0.03 and 0.05. Two

unidirectional printing directions, i.e., longitudinal and transverse, were used for tensile samples. Every data point is the average of at least seven measurements.

2.3.12 Interlayer shear strength (ILSS) measurement

Short beam shear (SBS) test of transverse and longitudinal printed samples was carried out to determine the adhesion between the printed layers with and without CNC through measuring the interlayer shear strength (ILSS). The SBS test was conducted on a Universal United STM testing system equipped with 10 kN load cell in three-point bending mode according to ASTM D2344. The displacement rate and the span-to-thickness ratio was set at 2 mm/min and 4 mm/min, respectively. The printing direction for SBS samples was longitudinal and transverse. Every data point is the average of at least seven samples.

2.3.13 Transmission electron microscopy (TEM)

Electron Microscopy Sciences® CF300-Cu copper TEM grids with carbon film were used in a JEOL 2010 TEM at 200kV to study the morphology of individual CNCs with a diluted concentration of 0.01 mg/ml in DI-water. The wet samples were stained for one minute with uranyl acetate58 and dried in the open air.

2.4 Test Conditions

Tables 1-4 summarize experimental conditions and different variables that have been studies in different phases of this research. **Table 1** indicates the samples that were prepared for the first feasibility study and the conditions under which these samples were created. **Table 2** is

similar information for the second feasibility study that was performed to analyze the efficiency of nanoparticle spray deposition.

Table 1. Spray coating operation parameters (Feasibility study #1)

Spray pattern	Full cone
Spray angle	20 deg
CNC concentration in coating suspensions	0.5 wt%, 1 wt%, 1.5 wt%
Inlet air pressure	148.3kPa – 244.8 kPa
Inlet air temperature	25℃
Inlet liquid pressure	96.5 kPa
Operating temperature	25℃

Table 2. Spray coating operation parameters (Feasibility study #2)

Atomization air pressure	100 kPa, 200 kPa
Liquid pressure	100 kPa
Operating temperature	25 ℃
Coating suspensions	1wt% CNC – 99wt% DI-Water
	2wt% CNC – 98wt% DI-Water
	5wt% Epoxy – 95wt% DI-Water
	1wt% CNC – 5wt% Epoxy - 94wt% DI-Water
	2wt% CNC – 5wt% Epoxy - 93wt% DI-Water
Rail speed	5 mm/s, 10 mm/s, 15 mm/s

Table 3. Test conditions of SAA system

Atomization Gas	Injection Pressure (MPa)	Liquid Temperature (°C)	GLR
CO_2	3	19, 25, 31.5, 35	0.02, 0.05, 0.075, 0.1, 0.2, 0.5, 1, 2, 3, 4
	6	19, 25, 31.5, 35	
	7.5	19, 25, 31.5, 35	
	9	19, 25, 31.5, 35	
N_2	3	19, 25, 31.5, 35	
	6	19, 25, 31.5, 35	
	7.5	19, 25, 31.5, 35	
	9	19, 25, 31.5, 35	

Table 3 demonstrates all different parameters that was investigated to characterize the SAA system, while **Table 4** presents the HNPS systems that were prepared and studied for fundamental understanding of evaporation induced self-assembly of nano-colloidal droplets. All reported data points in the coming sections are the average of at least five realizations. In addition, one or two-way analysis of variance (ANOVA) with a significance level of 5% (i.e., 95% confidence level) has been performed to ensure statistically significance of the reported results.

Table 4. Concentration and ratio of HNPS test cases

Nanoparticles in the Hybrid System	Concentration of Nanoparticles in suspension	Ratio of Nanoparticles in the Hybrid System
CNC-GNP	0.2 wt% 0.05 wt%	1:20, 1:10, 1:7, 1:5, 1:3, 1:2, 1:1, 2:1, 4:1, 6:1, 8:1
CNC-CNT	0.2 wt% 0.05 wt%	1:1, 2:1, 3:1, 4:1, 9:1, 10:1, 11:1
CNC-BNNT	0.2 wt% 0.05 wt%	1:15, 1:8, 1:6, 1:4, 1:2, 1:1, 2:1, 4:1, 6:1, 8:1, 10:1, 15:1, 20:1

3. RESULTS AND DISCUSSION

3.1 Nanoparticle Spray Deposition in 3D Printing [176][1]

In order to investigate the feasibility of targeted deposition of functional nanoparticles through atomization, a spray system working with high-pressure air was integrated within an FDM printer to enable spraying aqueous suspensions of CNC between polymer layers during printing. Upon injection of the aqueous CNC suspension through a cylindrical nozzle, a high-pressure liquid jet forms and undergoes severe instabilities due to the large pressure drop between the injector and ambient atmospheric conditions. The growth of instabilities between the liquid and air breaks up (i.e., atomizes) the liquid jet first into several long and slender liquid structures (ligaments) and further breaks up the ligaments into a large number of micron-size droplets at a small distance (4 -5 mm) downstream of the nozzle. [177]

[1] Reprinted with permission from "Atomization of cellulose nanocrystals aqueous suspensions in fused deposition modeling: a scalable technique to improve the strength of 3D printed polymers", by Shadi Shariatnia, et al., 2019. *Composites Part B: Engineering*, 177, Copyright 2019 by Elsevier.

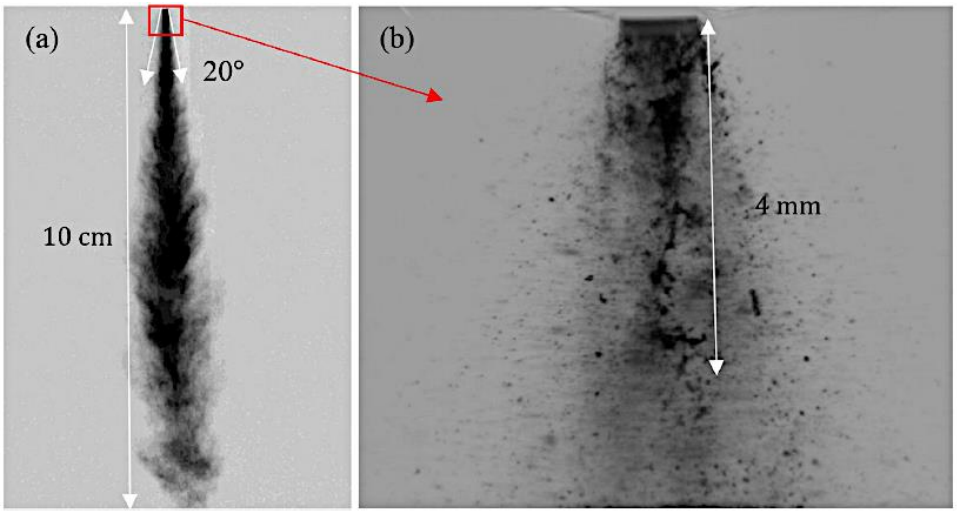

Figure 10. High-speed shadowgraph of (a) the overall spray taken at time t =0.5 ms; (b) a magnified region of the spray shown in (a) in the vicinity of the injector (red square shows the magnified window).

3.1.1 Spray Characterization

High-speed imaging results shown in **Figure 10** present the surface area and tip of the spray as well as a small area in the vicinity of the injector. **Figure 10 (a)** demonstrates the overall structure of the spray 500 μs after the start of injection. Post-processing of the images indicates the spray penetration length and spray spreading angle. Spray penetration length represents the farthest point with respect to the nozzle that the spray is in the liquid phase, after which the liquid evaporates entirely. Adjustment of the distance between the nozzle and the print bed according to the measured liquid penetration length assures complete evaporation of the aqueous CNC mixture before deposition of CNC particles on the ABS samples to minimize the moisture in the printed samples. This distance for the sprayer nozzle has been set to 10 cm so that it covers the width of the samples (12-19 mm) as well. The spreading angle represents the angle between the injector and the furthest point where the spray edge is detectable in the image. The spreading angle,

measured at 20º in **Figure 10 (a**), elucidate the maximum surface area of the printed ABS samples covered by the CNC particles at the time 500 μs, that the image has been taken. Further stabilization of spray with time leads to an increase in this angle as can be seen in **Figure 12**. **Figure 12 (b)** shows a magnified region of **Figure 10 (a)** in the vicinity of the injector marked with a red rectangle. This subfigure indicates that at a short distance with respect to the injector (~4 mm) all liquid ligaments break up into micron-size CNC-carrier droplets. Beyond 4 mm, the spray is characterized as a dense cloud of liquid droplets of variable sizes that spread along the spray spreading angle and undergo evaporation to release the CNC particles close to the printed ABS samples. These processing parameters are adjusted so that the droplets evaporate right before reaching the 3D printed surface leading to precise dispersion and uniform distribution of CNC without making the surface wet. It is noted that the viscosity of the aqueous mixture impacts the spray droplet size during atomization. However, considering the high shear rate at the nozzle (order of $10^4\ s^{-1}$) and the shear thinning effect of CNC, [178-180] the viscosity of the suspension does not significantly change and thus it does not affect the droplet size distribution. As air pressure is increased from 148.3 kPa to 244.8 kPa, the length of the liquid core and overall droplet sizes decrease from 31.6 μm to 29.9 μm. **Figure 11** shows this effect and the corresponding droplet size measurements.

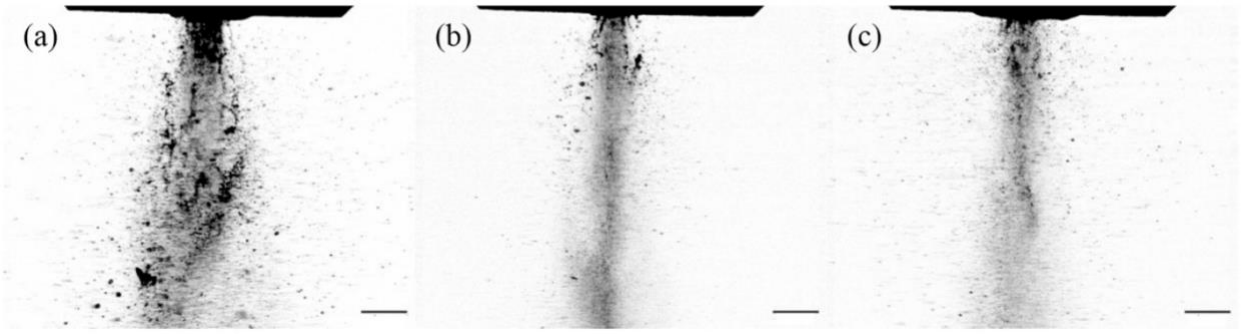

Figure 11. Effect of air pressure on droplet sizes, (a) P= 148.3 kPa, (b) P= 196.5 kPa, (c) P= 244.8 kPa. Scale bar is 1 mm.

Higher pressures deliver more gas to the mixture and burst of these gas bubbles results in smaller droplets. [181] 244.8 kPa pressure has been used here to enable faster droplet evaporation and smaller droplet size. The spatiotemporal evolution of the jet is depicted in **Figure 12**.

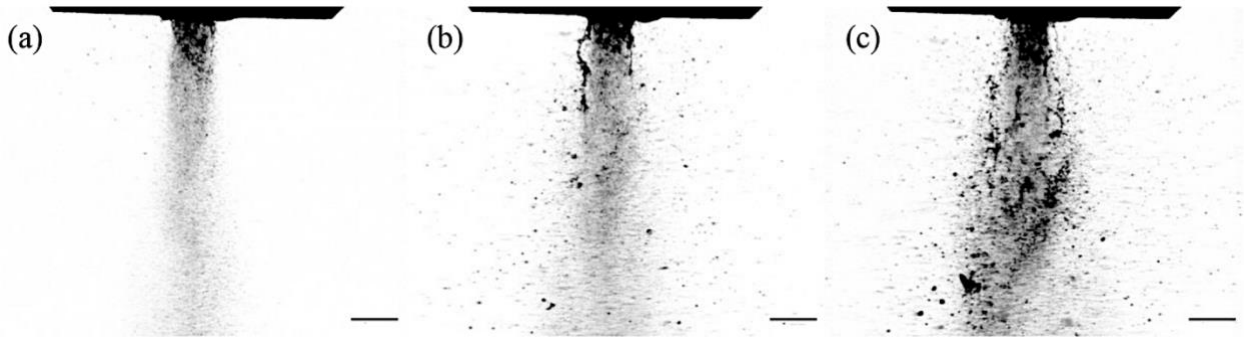

Figure 12. Spatio-temporal evolution of jet at P= 148.3 kPa, (a) t= 0.167 ms, (b) t= 1.83 ms, (c) t= 3.5 ms. Scale bar is 1 mm.

3.1.2 CNC morphology

Figure 13 compares the CNC particles before atomization, when they are in the container, and after being deposited. It can be seen that the structure of CNC remains intact after injection. This confirms that the sprayed CNCs will maintain their intrinsic properties and thus can be used to enhance interlayer adhesion of polymer.

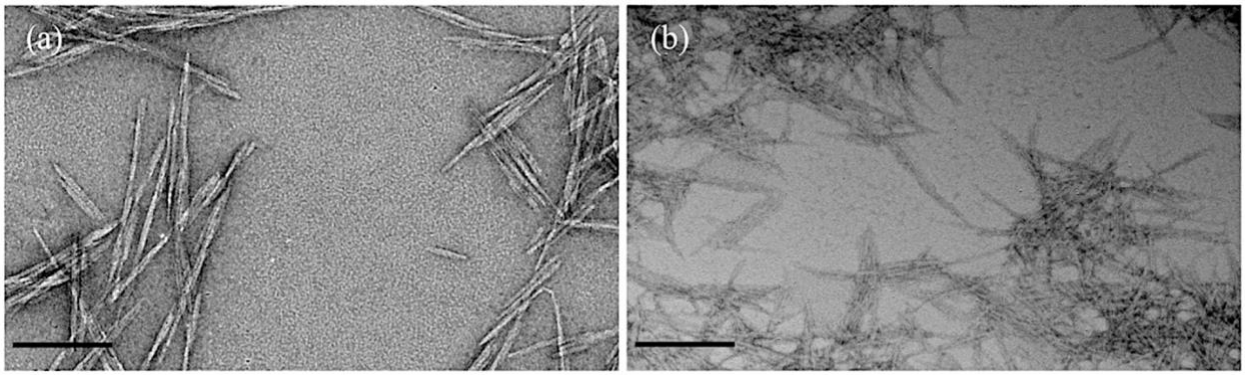

Figure 13. TEM micrograph of CNC particles (a) before and (b) after, atomization. Scale bar is 100 nm.

3.1.3 Specific density, CNC content, and thermal stability

The density for all CNC-ABS samples is found to be 1.07 ±0.04 g/cm^3, delineating that the addition of CNC does not increase the weight of printed parts, as expected considering the small amount of sprayed CNC. The CNCs wt% within the printed samples are correlated with their concentration in the sprayed aqueous suspension as shown in **Figure 14**. The neat ABS samples are used as the baseline for determining the CNC content (wt%). **Figure 14** also shows the thermal decomposition behavior of neat and CNC-ABS samples. Weight loss for CNC-ABS samples starts at ~250°C which is corresponding to the degradation temperature of CNC [182], indicating that CNC has been deposited on the ABS. The average CNC content is 2.5 wt%, 3.7 wt% and 4.6 wt% for 0.5CNC-ABS, 1CNC-ABS, and 1.5 CNC-ABS samples, respectively. It should be noted that the CNC wt% on the CNC-ABS does not increase linearly with increasing the CNC concentration of the sprayed suspension. All the samples show a steep fall between 370 °C and 470 °C, corresponding to the decomposition temperature of ABS [183].

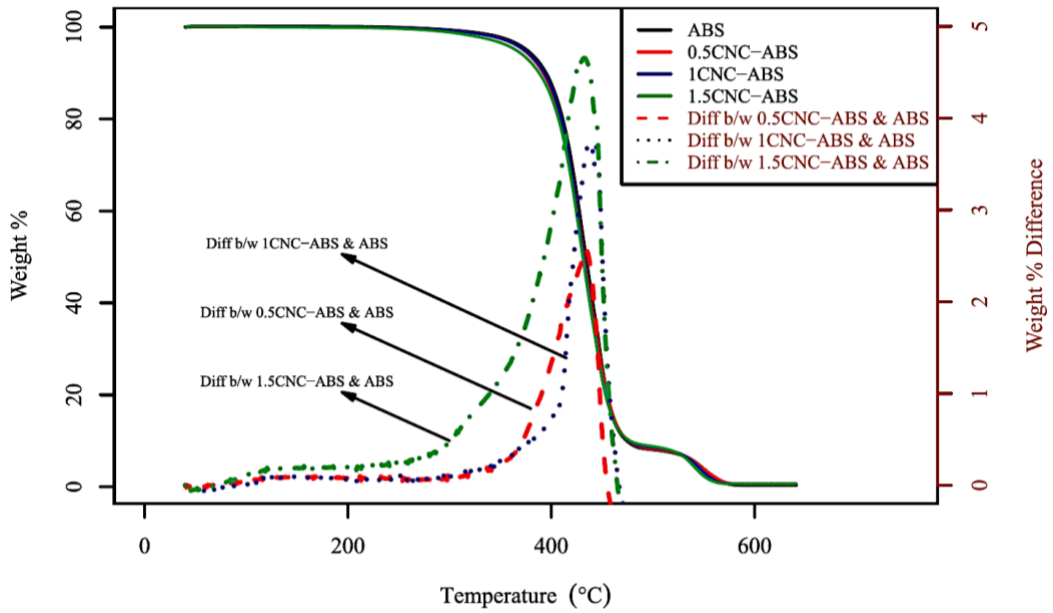

Figure 14. Deposited CNC on the CNC-ABS samples with respect to the concentration of the sprayed CNC suspension.

3.1.4 Fracture surface morphology

We studied the effect of CNC on the morphology of the fracture surfaces of the samples failed in the tensile testing using an SEM. In the absence of CNC, the main failure mechanism for samples with transverse printing direction (TD) is necking followed by separation of layers, as seen in **Figure 15(a**). Addition of 0.5 wt% and 1 wt% CNC has altered the fracture morphology of the samples as shown in **Figure 15(b) - (c).** It appears that more filaments in adjacent layers remained attached to one another during the failure. In addition, the fractured filaments in 0.5 and 1CNC-ABS samples imply that the contribution of brittle fracture has increased in contrast to the ductile failure mode (necking) in the samples without CNC. Increasing the CNC content increases the chance of formation of agglomerates and CNC multilayers as shown in **Figure 15(d)** for 1.5CNC-ABS. **Figure 15(e)** demonstrates freeze dried CNC and confirms the structure of CNC

agglomerates. These agglomerates can prevent effective adhesion between adjacent layers and reduce the ultimate strength. These observations suggest that the presence of CNCs alter the modes of fracture and provide stronger interlayer adhesion. These mechanisms can potentially lead to an increase in the absorbed energy in the fracture, and thus an improvement in strength.

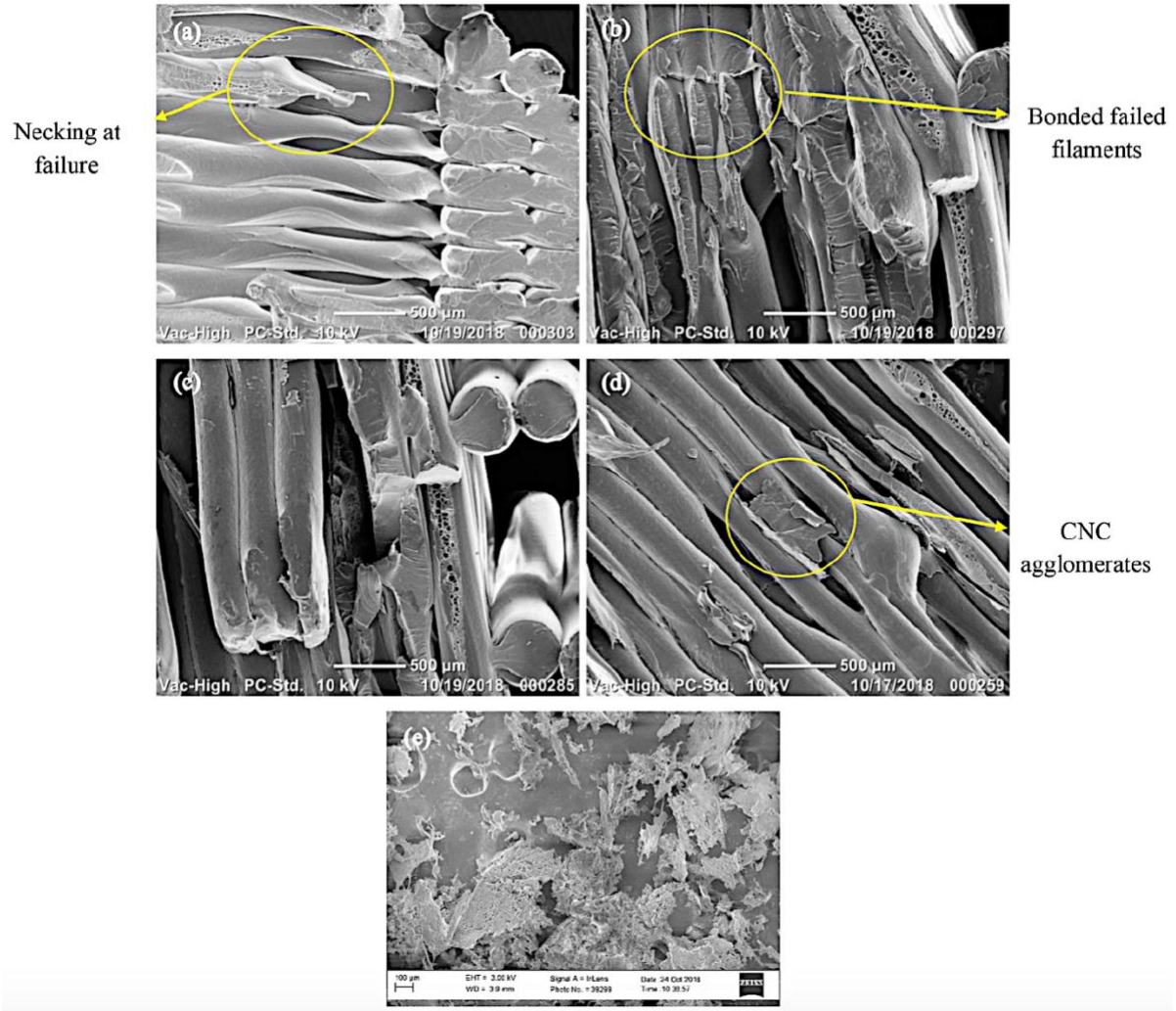

Figure 15. SEM images of fracture surface for TD samples failed in tensile (a) ABS (b) 0.5CNC-ABS (c) 1CNC-ABS (d) 1.5CNC-ABS (e) freeze dried CNC.

Figure 16 displays the fracture surface of the samples with longitudinal printing direction (LD) failed in tensile tests. As seen in **Figure 16(a),** for the case of ABS samples with no CNC content, adjacent layers are placed smoothly next to each other with almost a uniform distribution of voids between them. It can be seen in **Figure 16(b) - (c)** that the presence of CNC (0.5CNC-ABS and 1CNC-ABS) have altered the uniformity of voids along the thickness. This suggests that CNCs have modified the fracture surface morphology by better adhesion between adjacent layers that causes uneven surface fractures that affect the uniformity and distribution of voids. Increasing the CNC content to 1.5 wt% has facilitated the separation of layers as shown in **Figure 16(d).**

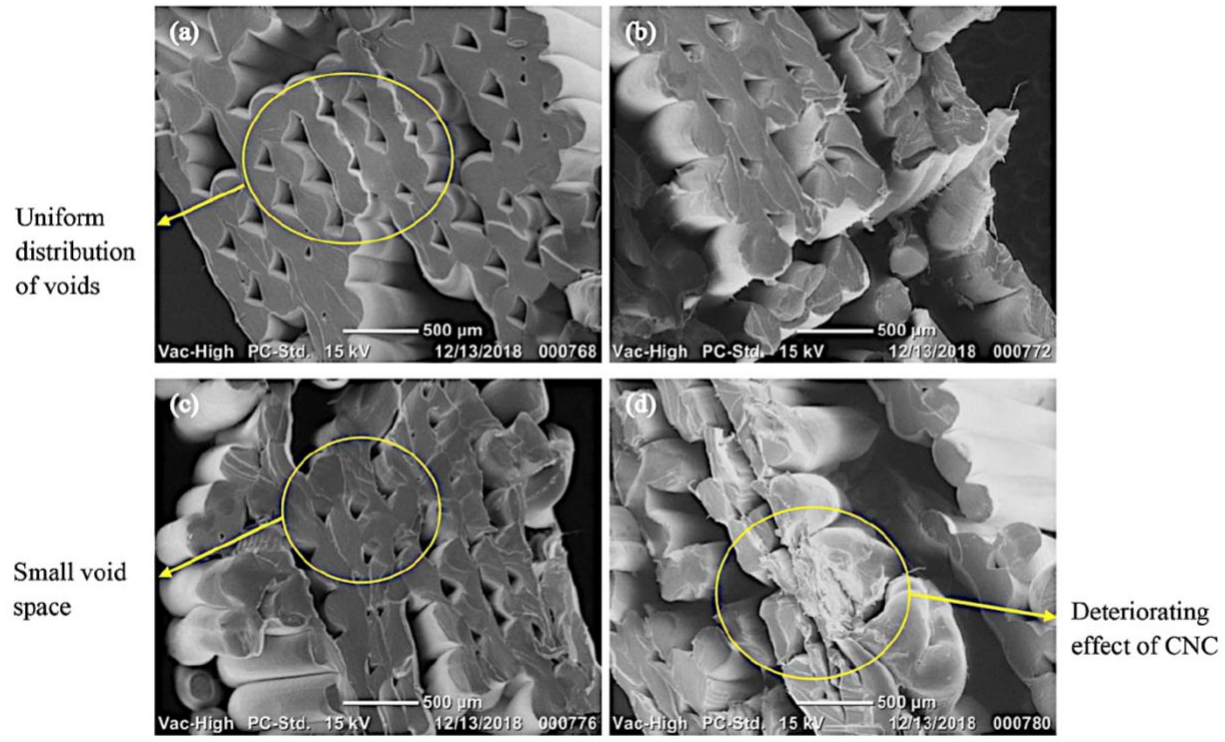

Figure 16. SEM images of fracture surface for LD samples failed in tensile (a) ABS (b) 0.5CNC-ABS (c) 1CNC-ABS (d) 1.5CNC-ABS.

Figure 17 shows the fracture surface of LD samples failed under short beam shear tests. As shown in **Figure 17(a),** a wide crack is seen in the neat ABS samples indicating an easy separation of layers in the absence of CNC. The nano-stitching effect of CNC represented in **Figure 17(b) - (c)** for 0.5CNC-ABS and 1CNC-ABS samples, has resulted in very narrow cracks in these cases inferring crack bridging capability of CNC. **Figure 17(d)** further elucidates that agglomeration of CNCs in 1.5CNC-ABS samples deteriorates the adhesion of contiguous layers.

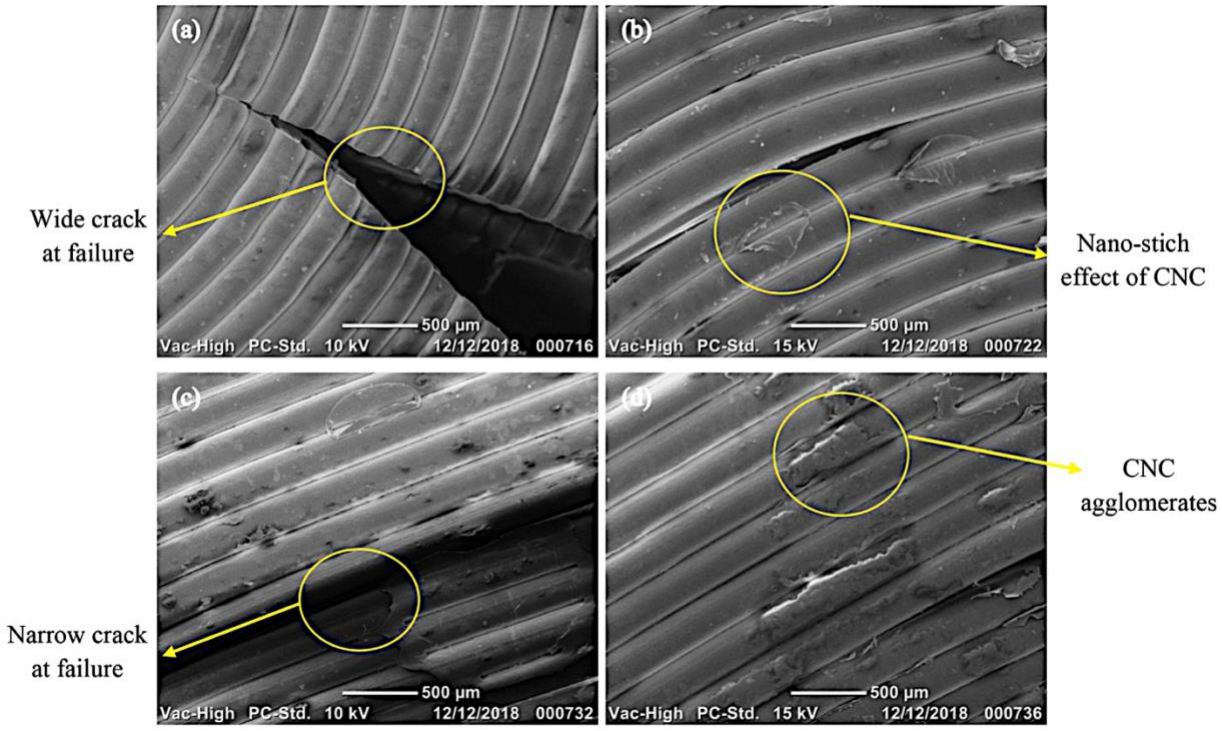

Figure 17. SEM images of fracture surface for LD samples failed in short beam test (a) ABS (b) 0.5CNC-ABS (c) 1CNC-ABS (d) 1.5CNC-ABS.

3.1.5 Thermomechanical properties

Table 5 presents the dynamic thermo-mechanical properties of the samples below and above T_g. At 25 °C (below T_g), increasing the CNC content slightly reduces the storage modulus (E'). A plausible reason is inhomogeneous dispersion of CNC that can lead to forming agglomerates (see **Figure 15(d)**), and thus reduce the stiffness by not allowing effective binding between CNCs and ABS. Initially, the presence of moisture because of incomplete water evaporation before depositing CNC on the ABS substrate was deemed as a potential culprit. Spaying pure water (without CNC) on the LD samples and comparing the properties with those of the neat ABS samples (see **Figure 20**) showed no difference in the tensile properties, and thus disproved the assumption that incomplete evaporation is the main cause for stiffness reduction. In contrast, at 125°C, the addition of CNC at concentrations larger than 0.5 wt% increases the rubbery modulus (E_r: the storage modulus above T_g) with a maximum 10% enhancement in 1CNC-ABS. Such an increase implies that CNC can reinforce the ABS and inhibit the chain segmental motion in the CNC-ABS samples above T_g, which is directly related to the rubbery modulus. Furthermore, the average value of tan δ (the ratio of the loss to the storage modulus) increases with CNC content indicating that the ability for energy damping is enhanced. Addition of CNC did not affect the T_g, according to **Table 5**.

Table 5. Dynamic mechanical analysis

Sample	E' at 25°C [MPa]	E_r at 125°C [MPa]	T_g [°C]	tanδ at T_g
ABS	1046.7±130	3.121±0.4	100.53±0.4	0.1338±0.009
0.5CNC-ABS	951.6±78	3.16±0.4	99.41±0.9	0.1419±0.01
1CNC-ABS	885±5	3.44±0.6	100.36±0.8	0.151±0.01
1.5CNC-ABS	860.4±45	3.32±0.6	101.39±1	0.173±0.04

3.1.6 Mechanical properties

The effect of CNC content on the tensile (LD and TD) properties of CNC-ABS samples are plotted in **Figure 18**. A single factor (CNC effect) ANOVA test was carried out to analyze the results between each test group of samples with and without CNC, as presented in **Table 6**. The difference between the mean values of each group is considered to be significant for a P value smaller than 0.001, and an F ratio ($F/F_{Critical}$) larger than 1.

The elastic modulus of the CNC-ABS samples containing CNC is enhanced; however, the trend is different in the longitudinal (LD) and transverse printing directions (TD). In the LD samples, spraying CNC with 0.5, 1 and 1.5 wt% concentrations increase the average elastic modulus by 8%, 20%, and 15%, respectively compared to that of neat ABS, as shown in **Figure 18**. This enhancement is statistically significant for 1CNC-ABS and 1.5CNC-ABS as indicated by the ANOVA results ($P < 0.001$ and F ratio > 1) shown in **Table 6**. For TD samples, spraying CNC up to 0.5 wt% concentrations increases the modulus by 15% verified by ANOVA results. Increasing the CNC concentrations to 1 and 1.5 wt% do not statistically affect the modulus according to **Figure 18** and **Table 6**. The enhancement of modulus in both tensile directions

suggests that the presence of CNC between the printed ABS layers can stiffen the samples. The enhancement of the modulus is the result of an increase in the apparent modulus of the CNC-ABS due to the contribution of the higher elastic modulus of CNC (150 GPa) that can increase the apparent modulus of CNC-ABS system in comparison with that of neat ABS (2.2 GPa).

The tensile strength of LD and TD CNC-ABS follows a similar trend to that of the modulus. Spraying CNC with 0.5 wt%, 1 wt%, and 1.5 wt% concentrations increase the strength of LD samples by 17%, 25%, and 8%, respectively that are statistically significant according to the ANOVA results. For TD samples, only 0.5CNC-ABS show an increase of 27% in the strength compared to that of neat ABS. Increasing the CNC concentration higher than 0.5 wt% reduces or does not statistically affect the tensile strength of TD samples. The increase in strength can be attributed to a better interlayer strength as CNC can increase adhesion between neighboring layers by mechanical interlocking between the adjacent layers via increasing the surface roughness and surface area of contact. Numerous hydroxyl groups available on the surface of CNCs can form physical and possibly covalent bond with polymer chains [184] and act as nano-stitches between the layers to improve the interlayer adhesion. In addition, the change of fracture modes in CNC-ABS samples can be another potential reason to increase the strength.

Table 6. ANOVA test results for tensile (longitudinal and transverse print) properties of *n*CNC-ABS samples

Sample	Sum of squares	*P* value	*F* ratio	Sum of squares	*P* value	*F* ratio	Sum of squares	*P* value	*F* ratio	Sum of squares	*P* value	*F* ratio
	LD Modulus			LD Strength			LD Strain at break			LD Toughness		
0.5CNC-ABS	0.079	0.101	0.019	43.33	1×10^{-5}	22.17	9×10^{-10}	0.004	8×10^{-4}	0.182	0.012	1.97
1CNC-ABS	0.429	0.001	2.145	90.73	2×10^{-6}	33.10	1×10^{-7}	0.403	0.15	0.105	0.033	1.24
1.5CNC-ABS	0.238	0.001	4.73	11.91	0.001	4.06	2×10^{-6}	0.626	0.05	0.088	0.122	0.56
	TD Modulus			TD Strength			TD Strain at break			TD Toughness		
0.5CNC-ABS	0.545	0.001	3.41	23.51	7.6×10^{-4}	5.74	1.1×10^{-4}	0.225	0.34	0.026	0.059	0.91
1CNC-ABS	0.009	0.717	0.03	4.79	0.022	1.51	3.8×10^{-5}	0.406	0.15	0.021	0.016	1.67
1.5CNC-ABS	4.2×10^{-5}	0.991	2.7×10^{-5}	56.85	5×10^{-6}	18.02	2.1×10^{-4}	0.108	0.63	0.064	4×10^{-4}	5.34

F ratio: the ratio of $F/F_{Critical}$
LD: Longitudinal printing direction
TD: Transverse printing direction

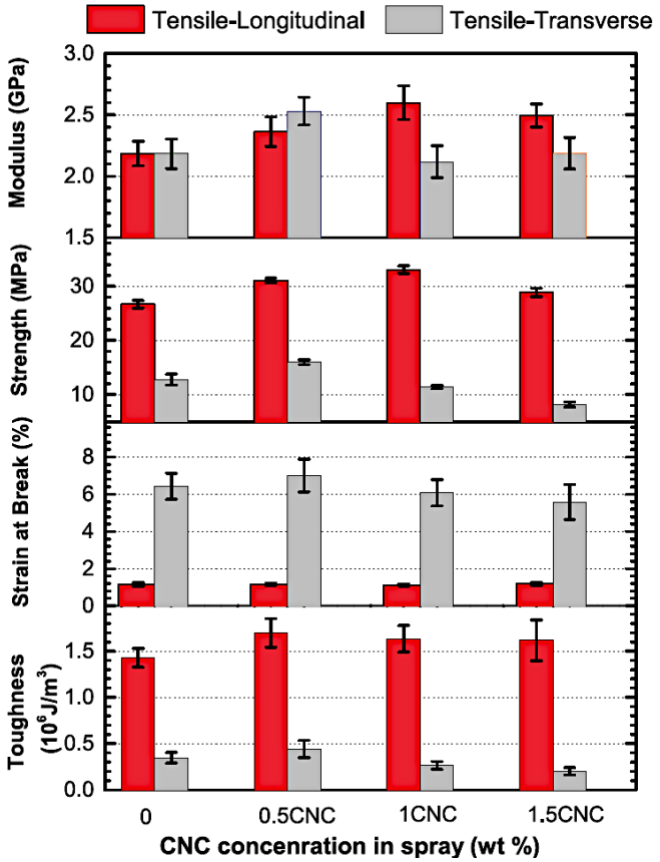

Figure 18. Effect of CNC content on tensile properties of the CNC-ABS samples. Error bars show one standard deviation.

The increase in tensile strength using spraying CNC is higher compared to methods in which CNC is mixed with ABS. It has been reported [185] that addition of 2.1 wt% CNC to ABS using a master batch method, increases tensile strength by 6.25% and modulus by 30%. In comparison, we show that the tensile strength of LD-1CNC-ABS and TD-0.5CNC-ABS samples increases by 25% and 27%, respectively. 0.5CNC-ABS samples contain 2.5 wt% CNC and 1CNC-ABS samples contain 3.7 wt% CNC as shown by TGA results demonstrating the effectiveness yet simplicity of the introduced method.

There is an optimum condition, i.e., 1CNC-ABS for LD and 0.5CNC-ABS, for which the tensile strength reaches a maximum. As the CNC concentrations increases to 1.5 wt% for LD and

1 and 1.5 wt% for TD, strength reduces. The strength of TD 1.5CNC-ABS samples is significantly lower (by 35%) than that of neat ABS. The lower strength indicates that interlayer adhesion and hence reduce the load transfer across the layers have reduced. Increasing CNC concentration increases the chance of both agglomerates and CNC multilayer formation (**Figure 15(d)**) that can potentially result in poor adhesion between layers and slippage of CNC with respect to each other, followed by reduction of interlayer strength and load transfer capability.

Although the trends in the tensile elongation at break and fracture toughness are not statistically significant according to the ANOVA results, they are following a trend like that of the tensile strength. For TD 0.5CNC-ABS samples, the elongation at break increases by ~10% and decreases for higher CNC concentrations. Furthermore, the toughness (the area under the stress-strain curve), shows an increase by ~20% and 30% for 0.5CNC-ABS samples in LD and TD directions respectively, suggesting higher energy absorption before the catastrophic failure. However, the toughness of TD 1CNC-ABS and 1.5CNC-ABS samples are lower even than that of neat ABS samples implying the pronounced effect of agglomeration and multilayer formation in the final fracture. The high standard deviation for the toughness data might be since toughness considers both stress and strain, and consequently, any experimental fluctuations due to CNC agglomeration or void formation becomes amplified.

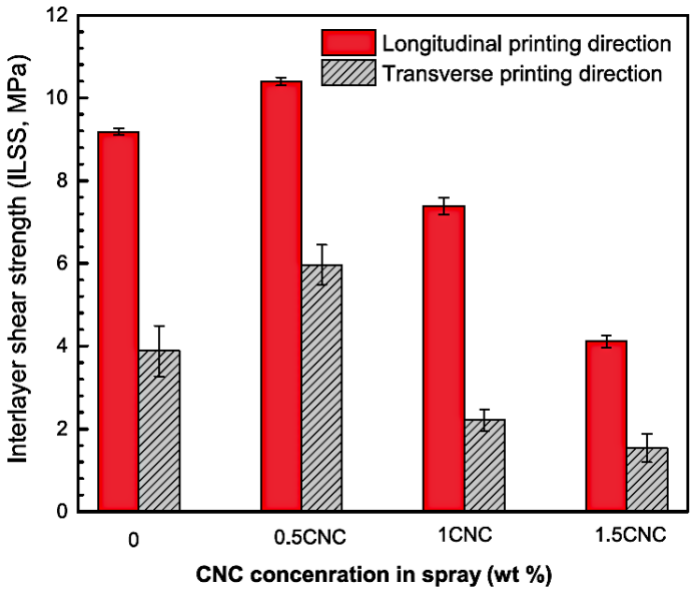

Figure 19. Effect of CNC content on interlayer shear strength of the CNC-ABS samples. Error bars show one standard deviation.

Figure 19 demonstrates the effect of CNC content on the interlayer shear strength (ILSS) of samples for both longitudinal and transverse printing directions. ILSS of LD sample is higher than that of TD sample at each CNC concentration. The addition of 0.5 wt% CNC to neat ABS increases the ILSS of LD and TD samples by 13% and 44%, respectively. These are significant improvements in the ILSS based on ANOVA test results presented in **Table 6**. This is particularly important as the separation of the layers is the main reason for the low strength values of 3D printed polymer parts. Enhancement of ILSS, in this case, can be due to the adhesive effect of CNC on adjacent layers, as it was seen in **Figure 17(b) and (c).** The adhesion effect of CNC is more pronounced for TD samples (44% improvement) suggesting that CNC nano-stitching effect leads to a larger relative improvement of interlayer adhesion in weak samples (TD samples) compared to strong samples (LD samples). The 1.5CNC-ABS sample exhibited the lowest ILSS due to the weak interlayer adhesion between layers corroborating the effect CNC agglomeration similar to

the trend observed in tensile tests. The improvement in ILSS can be related to the enhancement of tensile strength in LD and TD samples. There is a chance that depositing CNC suspension in large droplets that place on top of each other results in formation of these agglomeration sites. Our hypothesis is that if carrier droplets are small enough, they can distribute the particles more evenly across the substrate and better prevent aggregation for higher concentrations. One of the future works can be using the deposition system that is introduced in the next section to uniformly deposit micron size CNC carrier droplets while they are being 3D printed.

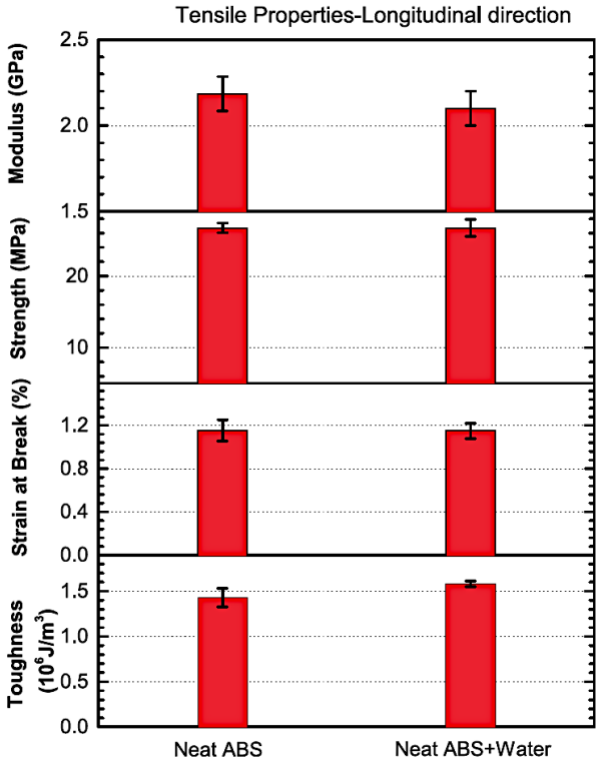

Figure 20. Effect of spraying water on tensile properties of ABS samples. Error bars show one standard deviation.

Assessing the thermo-mechanical properties and interlayer adhesion of CNC-ABS samples indicates that spraying the aqueous suspension of CNC with 0.5-1 wt% concentrations

significantly improves the tensile strength and modulus by 33% and 20% in longitudinal and transverse printing direction, respectively and the interlayer shear strength by 44%. This improvement indicates that spraying the aqueous CNC suspensions during 3D printing is an efficient yet simple technique to effectively disperse and distribute CNC to improve the properties of 3D-printed polymers, and thus is a departure from status quo where nanomaterials are added to the filaments through costly processing methods. This method does not only improve thermo-mechanical properties of the final part, but it is adjustable to any FDM printer enabling fabrication of functionally graded parts without interrupting the 3D printing process or altering the filaments prior to print.

3.2 Nanoparticle Spray Deposition in Composite Manufacturing [186][2]

Successful spray deposition of CNC particles that lead to enhanced properties of the 3D printed parts motivated us to test the feasibility of this method in another manufacturing area before moving forward with designing and investigating the SAA nanoparticle delivery system. This project employs two scalable coating techniques, slot die and spray coating (see **Figure 7**), to apply cellulose nanocrystals (CNCs) on the surface of glass fibers with the goal of enhancing interfacial interactions between glass fibers and epoxy and, consequently, the strength of fiber-reinforced composites. The quality of the cellulose coatings and the interfacial shear stress (IFSS), assessed via the single fiber fragmentation test (SFFT), are determined as a function of the method and conditions used to coat the fibers and compared for two methods. In addition, a comparison with

[2] Reprinted with permission from "Scalable coating methods for enhancing glass fiber-epoxy interactions with cellulose nanocrystals", by Ejaz Haque, et al., 2021. *Cellulose*, 28, 4685-4700, Copyright 2021 by Springer.

glass fibers coated with identical CNC formulations using a conventional laboratory-scale dip coating technique is provided. Results from scalable spray coating method were found to be comparable or superior to the dip coating technique, with spray coating outperforming dip coating by up to 18% on average depending on the coating applied. Further analysis was conducted on coating morphology, fracture behavior, elemental composition, and surface loading. The observed differences can be used to determine which technique is most appropriate for a given application.

Similar characterization techniques were utilized in this project as well. The liquid jet was visualized with the high-speed diffuse back illumination system. TGA assessed the CNC content coated on glass fiber in all three coating techniques. The mass of coating adhered to the surface of rovings was determined using TGA, and the results are reported in **Table 7**. All samples were brought from room temperature to 600°C. Changes in mass were monitored with respect to temperature, and it was observed that for all samples, mass loss plateaued at approximately 580°C at the latest. Though 600°C is insufficient to completely remove all organic material from the fiber surface, this plateau indicated that a stable char was achieved, and this temperature could be used as a suitable basis for comparison between coatings. DC samples yielded consistent results that generally tracked with the solids content of the coating solution (i.e., the mass lost for the 5EM 1CNC sample was approximately the sum of the mass lost from the 1CNC and 5EM samples individually). SC samples performed similarly except for a slightly lower result for the 5EM coating. SD samples did not follow such clear trends, likely a consequence of coating inhomogeneity. The 1CNC solution and, to a lesser extent, the 5EM solution failed to spread evenly across the GF surface. Instead, they pooled toward the edges of rovings which means an inhomogeneous coating.

Spray coating provided up to a 37% improvement in IFSS over uncoated fibers and up to an 18% improvement over fibers that were dip coated in equivalent coating formulations. Additionally, TGA revealed distinct decomposition peaks for SC coatings and broader, temperature-shifted peaks for SD coatings. This suggests that entrapment of CNCs within a network of emulsion polymers occurred less in SC samples, potentially allowing for more interactions between CNCs and the fiber and matrix. It can thus be concluded that spray coating can yield higher interfacial shear strengths.

Table 7. Mass (%) of coatings removed from chopped GF rovings by TGA. Averages are for 3 samples, and error is 1 standard deviation.

Sample	**Average mass loss (%)**
Uncoated	0.8 ± 0.1
Dip Coated (DP) 1CNC	2.3 ± 0.3
Slot Die (SD) 1CNC	4.2 ± 0.8
Spray Coated (SC) 1CNC	2.1 ± 0.3
DC 5EM	3.9 ± 0.1
SD 5EM	7.2 ± 0.6
SC 5EM	2.8 ± 0.2
DC 5EM 1CNC	6.7 ± 0.7
SD 5EM 1CNC	4.8 ± 0.03
SC 5EM 1CNC	6.1 ± 0.3

3.3 Supercritical Assisted Atomization [187][3]

Since spray nanoparticle deposition was proved as an efficient way in enhancing functionality and properties of the manufactured parts in the feasibility studies, this section is focused on fundamental understanding of jet breakup and spray formation mechanisms in SAA

[3] Reprinted with permission from "Experimental analysis of supercritical-assisted atomization", by Shadi Shariatnia, et al., 2021. *Physics of Fluids*, 33, Copyright 2021 AIP Publishing LLC.

system. This understanding paves the way for refining SAA as a precise method of Nanoparticle delivery in various systems. To accomplish these objectives, we designed and built an SAA system (illustrated in **Figure 8**) and resolved the jet breakup and spray characteristics via utilizing different optical diagnostics. For this purpose, the spray formation process using either CO_2 or Nitrogen (N_2) as the atomization fluid is portrayed via shadowgraphy and laser diffraction techniques. Furthermore, we leverage the linear instability analysis to delineate the dominating instability mechanisms at different flow conditions. Before diving deep into the analysis of SAA system and its characteristics, the thermophysical properties of the water-CO_2 and water-N_2 systems at equilibrium as a function of pressure and temperature is discussed. This is specifically important in explaining the behavior of the jet in SAA system.

3.3.1 Thermophysical Properties

Comparing the mole fraction of the dissolved N_2 in the N_2-water system with the CO_2 in CO_2-water system at room temperature versus pressure in **Figure 21** shows that the concentration of dissolved CO_2 in water is considerably higher than that of N_2. In addition, increasing the pressure does not significantly affect the solubility of N_2 in water, while the solubility of CO_2 increases with pressure until it reaches a plateau past the critical pressure of the CO_2-water binary system. [188, 189]

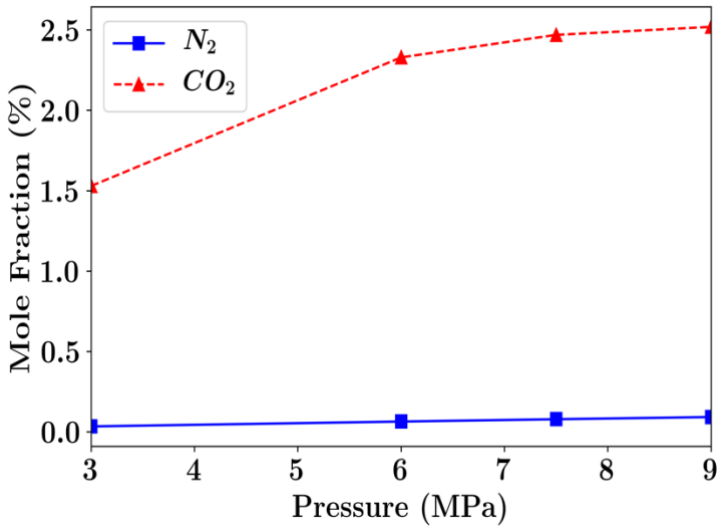

Figure 21. Mole fraction of the dissolved gas in water versus gas pressure at room temperature are adapted from the experiments conducted by Diamond et al. and Sun et al. [188, 189].

Due to the sensitivity of the thermophysical properties of the CO_2-water binary system to the temperature and pressure variations, we further discuss its phase diagram adopted from Diamond et al. [188] including the solubility of CO_2 in water as shown in **Figure 22**. The knowledge gained from the phase equilibria is key to define the limits of applicability of the proposed experimental conditions considered in this study with respect to the saturation lines and critical point of the CO_2-water system at equilibrium as shown in the shaded area. **Figure 22** shows the isopleths of CO_2 solubility in the water on a pressure-temperature phase diagram calculated by thermodynamic models. [188] Q_1 denotes the equilibrium state between H_2O-ice, CO_2-clathrate-hydrate, CO_2-bearing water and CO_2-vapor. The quadruple point Q_2 represents the equilibrium state between CO_2-clathrate-hydrate, CO_2-bearing water, CO_2-liquid and CO_2-vapor. LCEP (lower critical endpoint) which occurs at 31.5 ºC and 7.5 MPa is the critical point of the CO_2-water system at equilibrium that is slightly different than the critical condition of the pure CO_2 (31.7 ºC and 7.38 MPa). Our experimental condition (shaded area) expands over the vapor-CO_2 and liquid-CO_2

bearing water regions above and below the L_{aq}-L_{CO2}-V line, and thus spans from the two-phase region to single-phase supercritical fluid and a wide range of solubilities. We have designed test cases representing temperatures and pressures lower, higher, and very close to the critical point of the CO_2-water binary system at equilibrium to study the effect of a wide range of phase behaviors and the corresponding fluid properties on the breakup. In the remainder of the paper, we refer to subcritical (supercritical) conditions being lower (higher) than the critical pressure or temperature of the CO_2-water binary system at equilibrium.

The reduction in surface tension is one factor that can facilitate the atomization process and lead to a shorter liquid core and generation of finer droplets in gas-assisted atomization systems as shown in the classic studies of Lefebvre. [190] The surface tension forces that oppose distortion of the liquid surface have a critical role in dictating the size of the droplets, specifically at lower jet speeds where inertial forces are not strong enough to overcome the surface tension effects. Surface tension effects can also be important to breakup small-scale liquid structures in high-speed jets. [190] To investigate the role of gas dissolution in the water on the interfacial tension of the CO_2-water system, the diffusion coefficient of CO_2 versus pressure at a constant temperature (40 ºC) that are adopted from the experimental data of Tewes et al. [191] is illustrated in **Figure 23a**. The diffusion coefficient initially reduces with an increase in pressure from 3 to 4 MPa; however, it monotonically increases with pressure beyond 4 MPa and peaks close to the critical pressure of the CO_2-water system (dashed vertical line). [191]

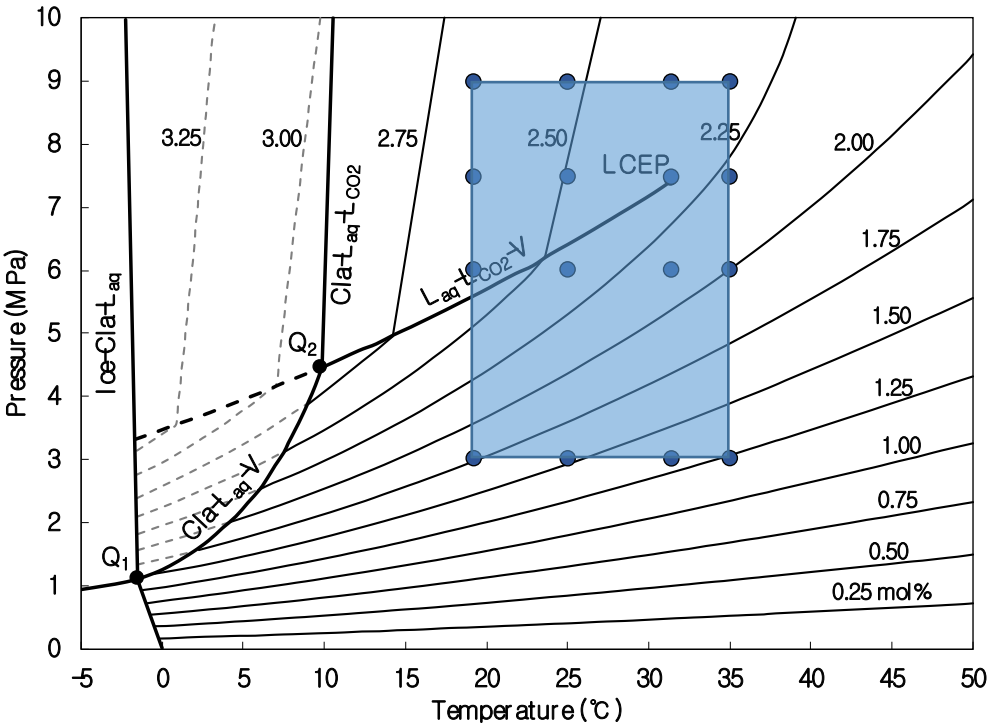

Figure 22. Phase diagram of the water-CO_2 binary system with selected isopleths of CO_2 solubility in the aqueous solution. LCEP denotes the lower critical endpoint of the system and Quadruple point Q_1 shows the equilibrium between H_2O-ice, CO_2-clathrate-hydrate, CO_2-bearing water and CO_2-vapor (Ice–Cla–Laq–V). The quadruple point Q_2 indicates the equilibrium between CO_2-clathrate-hydrate, CO_2-bearing water, CO_2-liquid and CO_2-vapor (Cla–L_{aq}–L_{CO2} –V). Reprinted with permission from [188]. The shaded area represents the experimental conditions considered in this study.

The mole fraction of the dissolved CO_2 in water plotted versus temperature and pressure in **Figure 23b** corroborate that CO_2 solubility in water also increases with pressure and decreases with an increase in temperature. Consistent with the diffusion coefficient data portrayed in **Figure 23a**, **Figure 23b** also shows that after reaching the critical pressure, the solubility does not increase drastically with an increase in pressure. **Figure 23c** illustrates the variation of interfacial tension of the CO_2-water system versus temperature and pressure extracted from the experimental data reported by Bachu et al. [192] This figure shows that the interfacial tension decreases by 38% from 3 MPa to 9 MPa. [193] It can be deduced that the increase in the solubility of CO_2 in water with

pressure is correlated with a decrease in the interfacial tension of the CO_2-water system. In addition, the interfacial tension increases with a decrease in the solubility (**Figure 23b**) as the temperature increases to the critical temperature. The interfacial tension drastically drops near the critical temperature of the CO_2-water system, (i.e., 31.5 ºC shown by the vertical dashed line in **Figure 23c**) for all pressures.

These results indicate that the proximity to the critical temperature and pressure of the binary system has a profound effect on reducing the interfacial tension due to the sharp increase in gas diffusion and solubility in water. **Figure 23d-e** represents the solubility and interfacial tension of the N_2-water system. The solubility of N_2 in water is much smaller than the solubility of CO_2 in water (also shown in **Figure 21**); however, it is more sensitive to the temperature variation compared to the solubility of CO_2 in water, particularly at higher pressures. **Figure 23e** shows that the interfacial tension of the N_2-water system is significantly higher than CO_2-water, especially at higher pressures and it drops sharply with an increase in temperature.

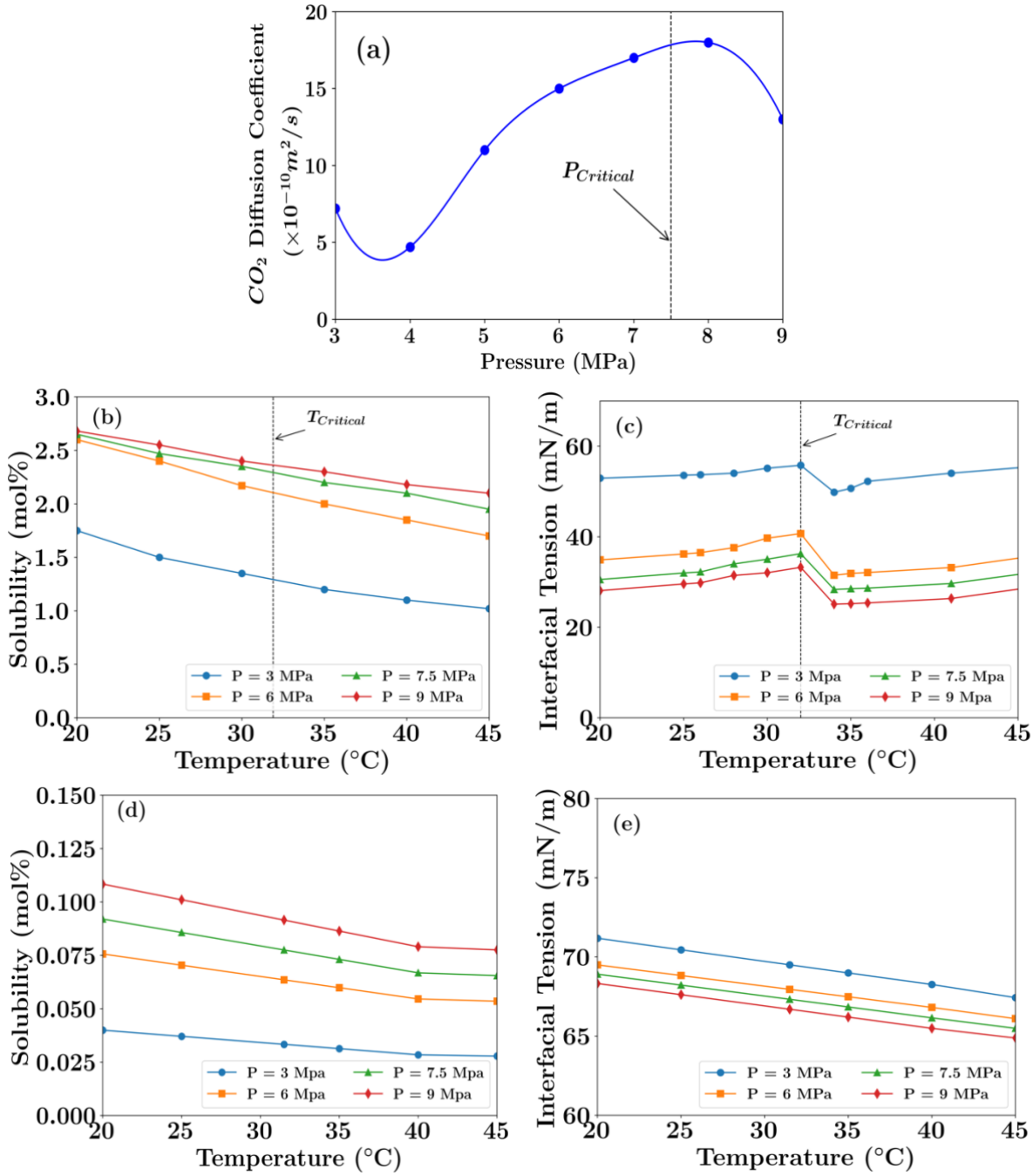

Figure 23. (a) Diffusion coefficient of CO_2 in water at 40℃ as a function of pressure adopted from Tewes et al. [191] Vertical dashed line indicates the critical pressure; (b) solubility of CO_2-water binary system

as a function of temperature at various pressures adopted from Diamond et al. [188]; (c) interfacial tension of CO_2-water system as a function of temperature at various pressures adapted from [192] Vertical dashed line indicates the critical temperature; (d) solubility of N_2-water system as a function of temperature at various pressures adapted from [189]; (e) interfacial tension of N_2-water system as a function of temperature at various pressures adapted from [194].

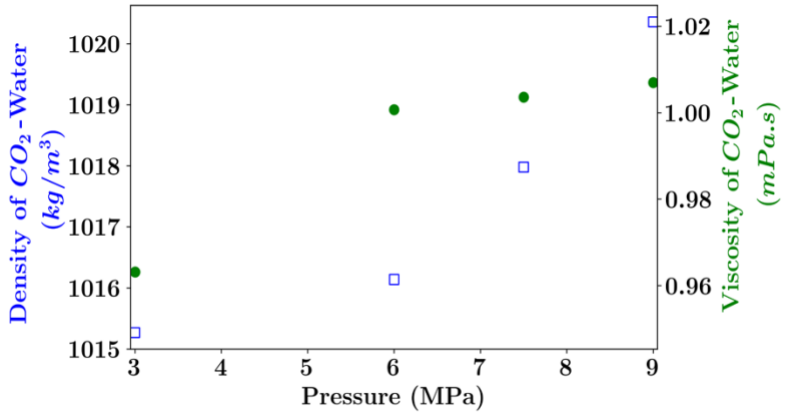

Figure 24. Density (open blue square and left axis) and viscosity (solid green circle and right axis) of the CO_2-water system versus pressure at 25℃ adapted from [193].

In contrast to surface tension, the density and viscosity of the CO_2-water system are not very sensitive to an increase in pressure as shown in **Figure 24.** In fact, by increasing the pressure from 3 to 9 MPa at room temperature, the viscosity and density only increase by 4.5% and 5%, respectively. [195] The viscosity data adopted from McBride-Wright et al. [195] indicate that increasing the temperature of the CO_2-water system at 7.5 MPa from room temperature to the critical temperature of 31.5 ºC results in about 15% drop in viscosity; indicating that temperature has a more profound effect on the viscosity at higher temperatures (i.e. above 45ºC). In summary, solubility and interfacial tension are the two important parameters that vary noticeably between N_2-A and CO_2-A cases.

3.3.2 Pressure Effects on Primary Breakup

Figures 25-28 visualize the CO_2-A and N_2-A cases in the near-nozzle region and at the early stages of spray development for different test conditions outlined in Table 1. It is noted that the nozzle has multiple injection orifices and the out-of-focus structures, as annotated in **Figure 25c**, belong to one of the neighboring plumes. The spacing between orifices is such that plumes do not interfere with each other, especially at the early stages of the spray development as evident in **Figure 25a** and **25d**.

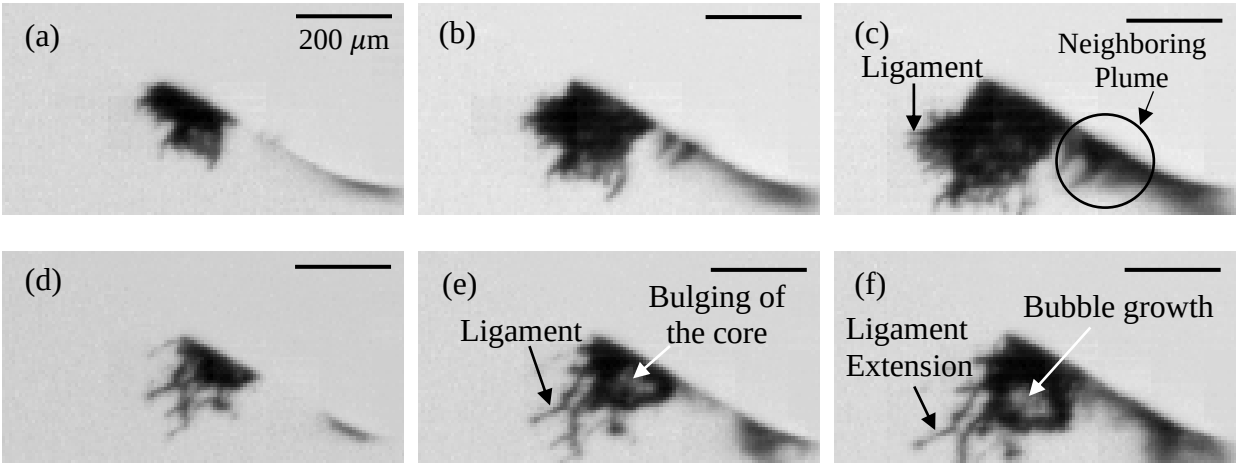

Figure 25. High-speed images (500,000 fps) comparing the primary breakup in (a-c) N_2-A, and (d-f) CO_2-A jet. All cases are conducted at GLR = 0.2, T_{inj} = 25 ºC, P_{inj} = 9 MPa developing with time from left to right with a 2 μs time interval between the frames. The scale bar is identical (200 μm) for all images.

The GLR is kept constant at 0.2 for all cases reported in this subsection. **Figure 25** compares the primary breakup of N_2-A (**Figure 25a-c)** with those of CO_2-A (**Figure 25d-f**) at 25 ºC and 9 MPa injection pressure. This figure shows the evolution of the liquid jet from left to right with a 2 μs time interval between the frames. A bulged liquid core in CO_2-A is evident in **Figure**

6e, that emerges as a gas bubble very close to the nozzle (~ one orifice diameter down the nozzle) that expands radially (**Figure 25f**) and squeezes the liquid axially due to the inertial forces imposed by the expanding gas bubble. As a result, the edges of the liquid core become thinner and deform into relatively long ligaments. These ligaments and liquid structures elongate axially before breaking up into small droplets very close to the nozzle. Similar deformations pertaining to a bulged core due to the emergence of gas bubbles and their expansion and ligament formation have been observed in the spray images of effervescent atomizers. [196, 197]

The liquid core in N_2-A does not exhibit any evident expanding gas bubbles, and the created ligaments are significantly shorter in contrast to the CO_2-A at comparable times (**Figure 25 a-c**). In fact, the ligaments formed in CO_2-A have an aspect ratio (length to diameter) of about 10-15 while the ligaments in N_2-A represent a 3-5 range aspect ratio. The droplets that eventually break from high-aspect-ratio ligaments are expected to be smaller as will be further discussed in the following subsections. The discrepancies observed in the breakup process of these two cases at the same injection conditions are mainly related to the smaller amounts of the dissolved N_2 in water since the other thermophysical properties of these two cases are not significantly different. The lower dissolved N_2 concentration suggests that the main underlying breakup mechanism, in this case, is not the emergence of gas from the liquid phase and the subsequent formation and the burst of the gas bubbles. The differences in the ligament sizes can also be attributed to the lower surface tension of the CO_2-water system at 9 MPa compared to the N_2-water system (29.65 vs. 66.09 mN/m for CO_2), [193] which makes the interface more prone to deformation at scales much smaller than the liquid jet.

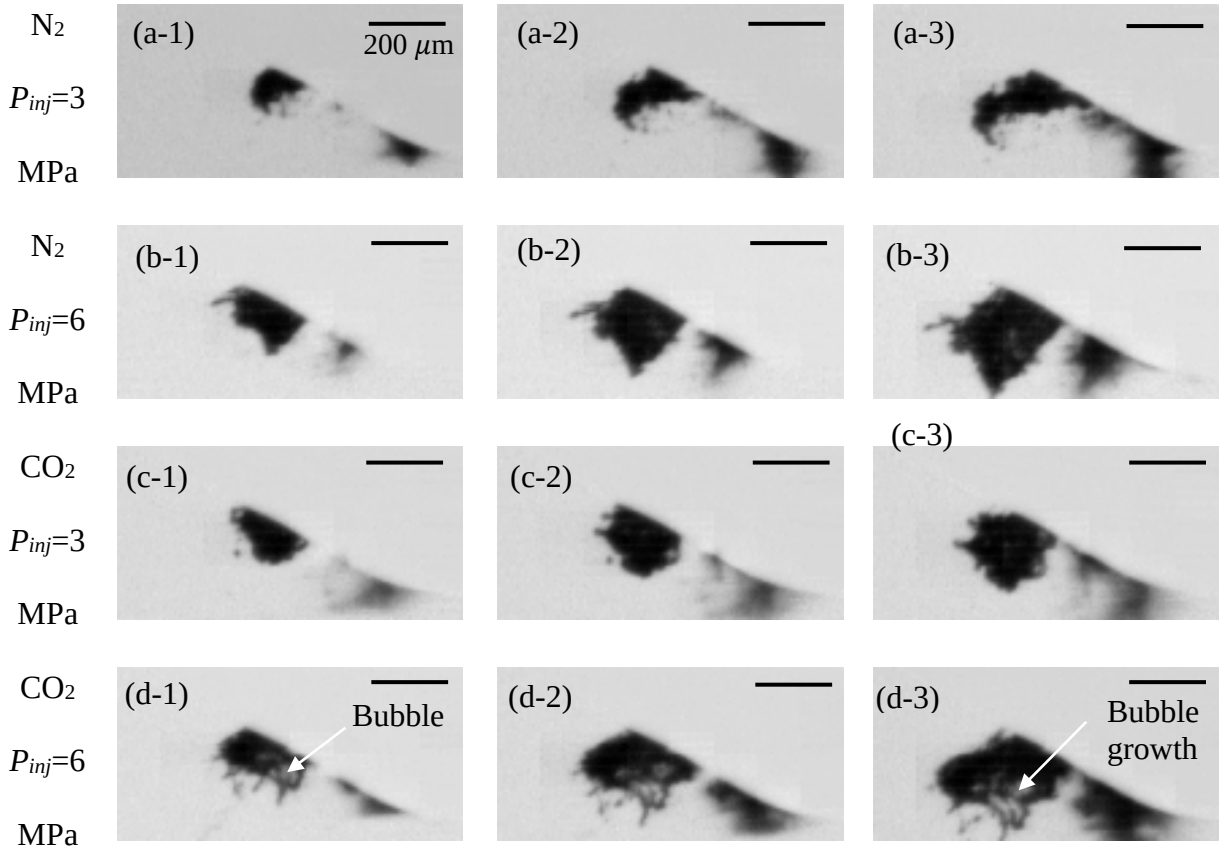

Figure 26. High-speed images (500,000 fps) comparing the primary breakup in (a-b) N_2-A, and (c-d) CO_2-A jet; both at GLR = 0.2, T_{inj} = 25ºC, and different injection pressures with 2μs time intervals between the frames. The scale bar is identical (200 μm) for all images.

Figure 26 illustrates the difference in spray behavior at lower pressures for both N_2-A and CO_2-A. The structure of the liquid core does not portray noticeable bubble formation at 3 MPa for both cases (**Figure 26a (1-3)** and **c (1-3)**). Even at 6 MPa, N_2-A does not exhibit major bubble formation in the liquid core. However, it is evident from **Figure 26b** and **d** that formation of the gas bubbles and ligaments and liquid core bulging initiates above 3 MPa for the CO_2-A and intensifies with an increase in pressure (**Figure 25f** and **26d**) as the solubility of CO_2 in water increases with pressure.

Figure 27 represents a higher resolution image of the primary breakup and at a later time compared to **Figure 26**. The injection pressure of 7.5 MPa is also included in this figure. **Figure 27 (a-d)** visualizes the CO_2-A liquid jet injected into ambient pressure and room temperature at the same snapshots (23.81 μs) and 3, 6, 7.5, and 9 MPa injection pressure, respectively. It is evident from **Figure 27 a-d** that increasing the injection pressure from 3 to 7.5 MPa has significantly reduced the intensity of the black pixels; lighter shades of gray are noticeable in the spray area. This suggests that the binary system exhibits a lower density, which can be attributed to the separation of the dissolved CO_2 and the formation of a two-phase bubbly flow due to depressurization. This observation is consistent with the microscopic images of the early breakup of effervescent atomization that depict a lighter expanded area filled with gas bubbles surrounded by the darker regions associated with the liquid. [197] Since the diffusion coefficient of CO_2 in water reaches a maximum very close to the critical pressure of the binary system (i.e., 7.5 MPa) as illustrated in **Figure 23a** and leads to increased solubility of CO_2 in water (**Figure 23b-c**), it is expected that a larger volume of the jet core contains dissolved gas. These effects tend to facilitate the emergence of the gas bubbles from the liquid phase due to depressurization, particularly at 7.5 MPa (**Figure 27c**). **Figure 27e-h** exhibits almost similar color intensity in the liquid jet core for N_2-A; suggesting that jet core density has not been drastically affected by the dissolved N_2. In addition, the liquid jet appears wider for the CO_2-A that is linked to the radial expansion of the gas bubbles in the jet core at this early stage of break up that is absent in the N_2-A case since the solubility of N_2 in water is insignificant.

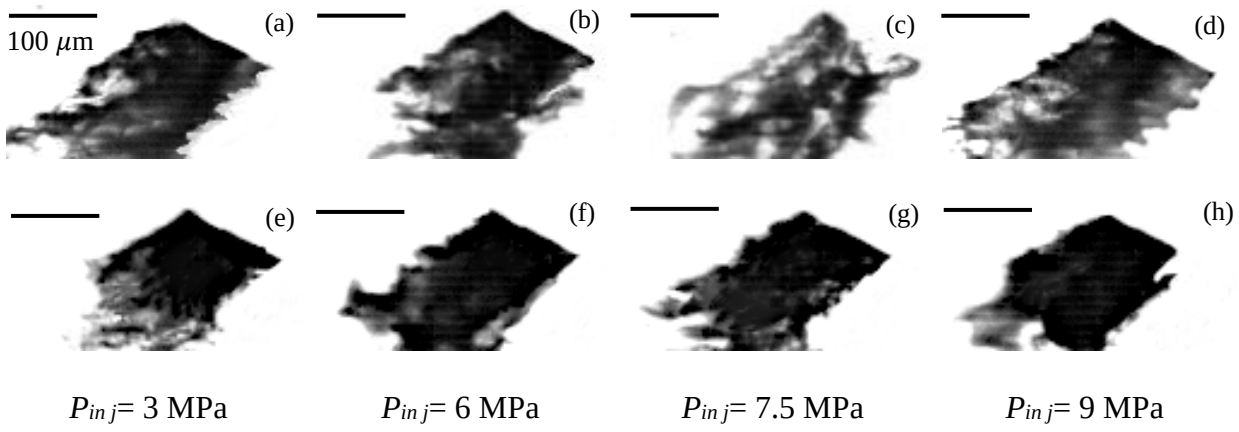

Figure 27. High-speed images (420,000 fps): visualizing the effect of injection pressure on the early development of spray: (a – d) CO_2-A, and (e – h) N_2-A. All images are captured at 23.81 μs after the start of injection into atmospheric pressure at T_{inj} = 25 ºC and GLR = 0.2. The scale bar (100 μm) is identical for all the images.

The length of the liquid core and the spray cone angle are depicted in **Figure 28a-b** to represent the overall spray behavior for CO_2-A and N_2-A. The measurements are made on a fully developed and stabilized plume one millisecond after the start of injection for 10 different shots for each case. The quasi-steady liquid length is consistently determined from the high-speed imaging using a 3% threshold of maximum intensity as recommended by Siebers. [198] Spray cone angle represents the angle between two lines drawn from the tip of nozzle tangent to the outer margin of the plume after injection. **Figure 28c** demonstrates an example of the liquid core length and spray cone angle measurement at 3 MPa for the CO_2-A. **Figure 28a-b** shows that by increasing the injection pressure from 3 to 9 MPa, the length of the liquid core decreases while the spray cone angle increases for both N_2-A and CO_2-A; however, the liquid core is substantially shorter, and the spray angle is wider for the CO_2-A.

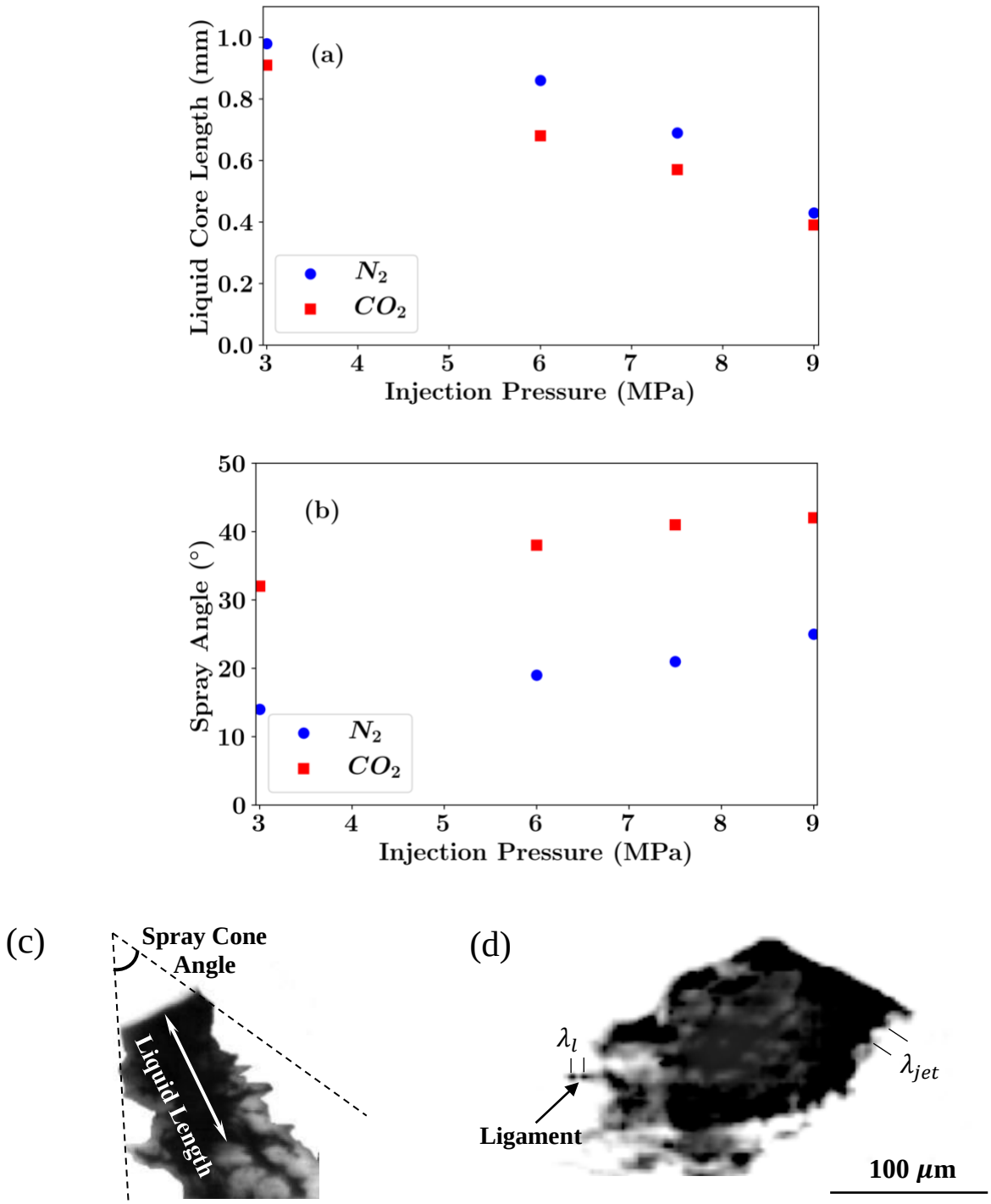

Figure 28. Effect of the injection pressure on the (a) liquid core length; (b) spray cone angle; (c) exemplified liquid core and spray cone angle measurement for CO_2-A at GLR = 0.2, P_{inj} = 3 MPa, T_{inj} = 25 ºC; and (d) exemplified wavelength measurement on liquid jet (λ_{jet}) and ligaments (λ_l) for CO_2-A jet for P_{inj} = 7.5 MPa, T_{inj} = 31.5 ºC and GLR= 0.2.

Interestingly, the contrast between the liquid core length in CO_2-A and N_2-A is more noticeable at the injection pressure of 6 and 7.5 MPa; closer to the critical point of the CO_2-water system than at 3 and 9 MPa. Since the main difference between CO_2-A and N_2-A spray at the same injection condition is the lower concentration of the dissolved gas in case of the N_2-A spray, this behavior suggests that the breakup mechanism is linked to the expansion and burst of the dissolved gas bubbles that disintegrate the liquid core more intensely for the CO_2-A at comparable pressure, liquid density, and viscosity. The higher concentration of CO_2 in water compared to N_2 at the same injection pressure, particularly near the critical point justifies this observation. The acceleration and inertia of the liquid ligaments increase with pressure and at a greater rate for CO_2-A. Thus, the higher momentum resulting from the ligament breakup scatters the smaller droplets further outward leading to a wider spray cone angle by increasing the injection pressure. **Figure 28d** exemplifies the instability wavelengths measurement (shown with short solid lines), which measure the distance between two visible consecutive peaks seen at the periphery of the jet liquid core and ligaments that will be used for the linear instability analysis.

3.3.3 Temperature Effects on Primary Breakup

The effects of the temperature of the injected mixture on the jet primary breakup are presented in **Figure 29a-d** for the CO_2-A and in **Figure 29e-h** for the N_2-A. The high-speed images were captured at the same time after the start of injection (i.e., 19.05 μs) for all cases. The injection pressure is kept constant at 7.5 MPa for all cases and the mixture temperature prior to injection varies between 19-35 °C. **Figure 29a-b** illustrate that the liquid core is shorter at lower temperatures (i.e., 19 and 25 °C); however, at 31.5 °C, the liquid core is longer, and the ligaments

are shorter than those of 19 and 25°C. This behavior is linked to the decrease in the CO_2 solubility in water with an increase in temperature that drops from 2.6 to 2.1 mol% by increasing the temperature from 19-31.5°C at 7.5 MPa. As discussed in **Figure 25-26**, bubble formation, growth, and burst are the main mechanisms responsible for the breakup of the liquid core containing dissolved gas. At the supercritical temperature of 35 °C shown in **Figure 29d**, the overall shape of the spray is significantly different: the liquid core is invisible, the small-scale structures are scattered more radially outwards compared to the lower temperatures (**Figure 29a-c**). In contrast, in **Figure 29a-b** ligaments are more visible and in the case of T_{inj}= 19 ºC (**Figure 29a**), ligaments break up into small droplets is also evident. In addition, the surface tension of the CO_2-water system drastically drops by increasing the temperature from 31.5 to 35 °C (**Figure 23c)** that makes the interface more prone to deformation and disintegration as comparing **Figure 29c** and **d** indicate. **Figure 29e-h** portraying the jet breakup for N_2-A reveals that increasing the temperature does not significantly modify the liquid jet behavior. At 35 ºC (**Figure 29h**) where surface tension decreases however, the instabilities are more pronounced, and a shorter liquid core is observed in N_2-A.

Therefore, the temperature of the injected mixture affects the liquid jet breakup from three different perspectives: (1) solubility decreases with an increase in temperature (**Figure 23a** and **c**); (2) the interfacial tension decreases with an increase in temperature and drastically drops near the critical temperature (**Figure 23b** and **e**). As a result, increasing the temperature pose two contradictory effects on the atomization process: while the capillary breakup is potentially enhanced due to the lower surface tension, the smaller amount of the dissolved gas in liquid implies that there are fewer gas bubbles in the mixture to expand, burst and eventually shatter the liquid

core. Since the surface tension plays a more dominant role after the primary breakup and on the small-scale liquid structures, [199] the change in solubility is the main factor driving the primary breakup with an increase in temperature that is more pronounced near the critical point of the CO_2-water system.

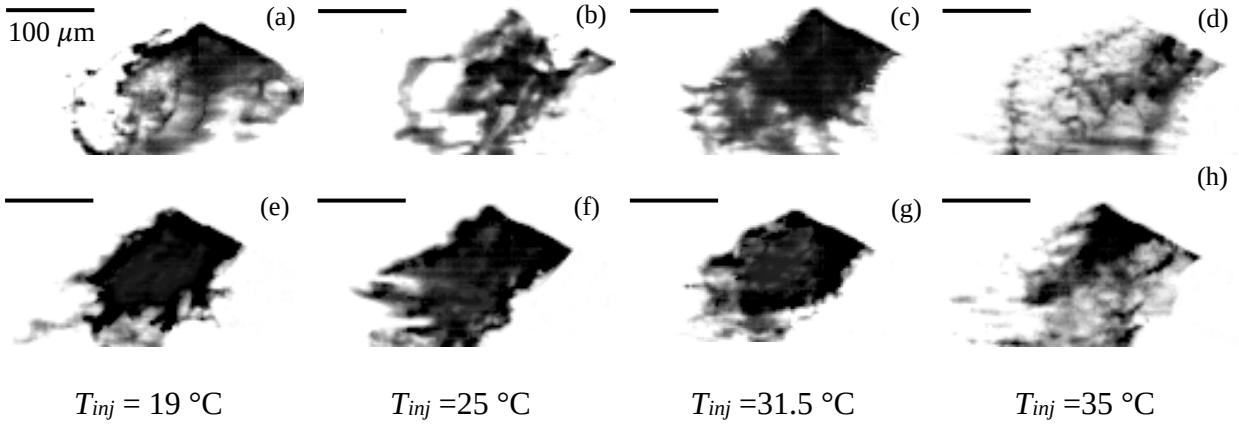

Figure 29. High-speed images (420,000 fps): visualizing the effect of mixture temperature on the early development of the spray: (a – d) CO_2-A and (e – h) N_2-A. P_{inj} = 7.5 MPa and GLR= 0.2. All snapshots are captured at 19.05 $\boldsymbol{\mu}$s. The scale bar (100 $\boldsymbol{\mu}$m) is identical for all images.

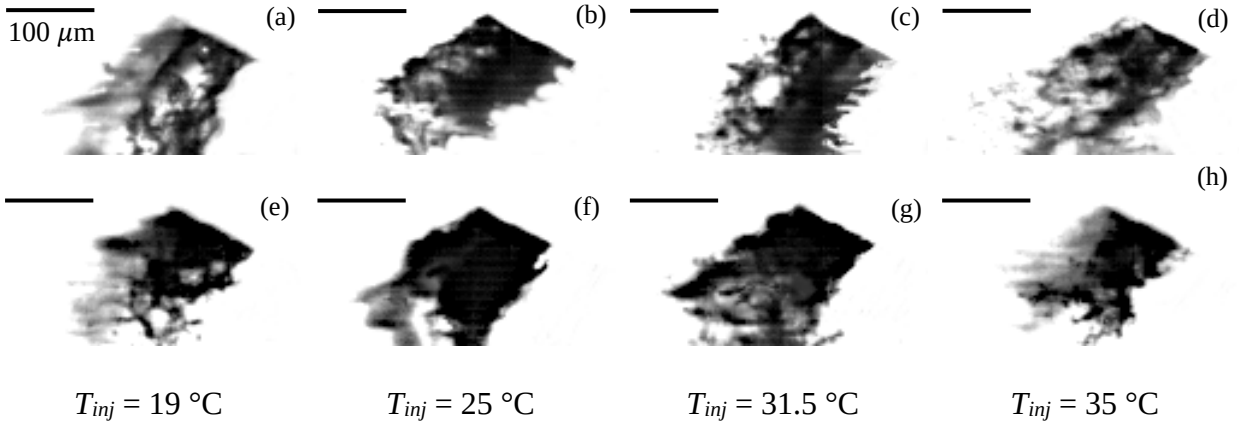

Figure 30. High-speed images (420,000 fps): visualizing the effect of mixture temperature on the early development of the spray: (a – d) CO_2-A and (e – h) N_2-A jet. P_{inj} = 9 MPa and GLR= 0.2. All snapshots are captured at 19.05 $\boldsymbol{\mu}$s. The scale bar (100 $\boldsymbol{\mu}$m) is identical for all images.

By increasing the injection pressure to 9 MPa (supercritical) (**Figure 30**) the spray shapes for both N_2-A and CO_2-A do not significantly change by varying the temperature. Comparing **Figure 29d** and **Figure 30d** reveals that at 7.5 MPa and 35 ºC the CO_2-A spray is developed wider compared to the 9 MPa and numerous small droplets are detected at the periphery of the shattered jet. The diffusion coefficient increases near the critical pressure (**Figure 23a**) and then decreases by increasing the pressure to 9 MPa. Thus, more CO_2 is dissolved in water at 7.5 MPa than 9 MPa and eventually, the separation of the dissolved gas in liquid amplifies the jet instabilities and promotes the jet break up. Therefore, 7.5 MPa and 35 ºC create a unique condition to facilitate the breakup as surface tension decreases, and gas solubility increases simultaneously.

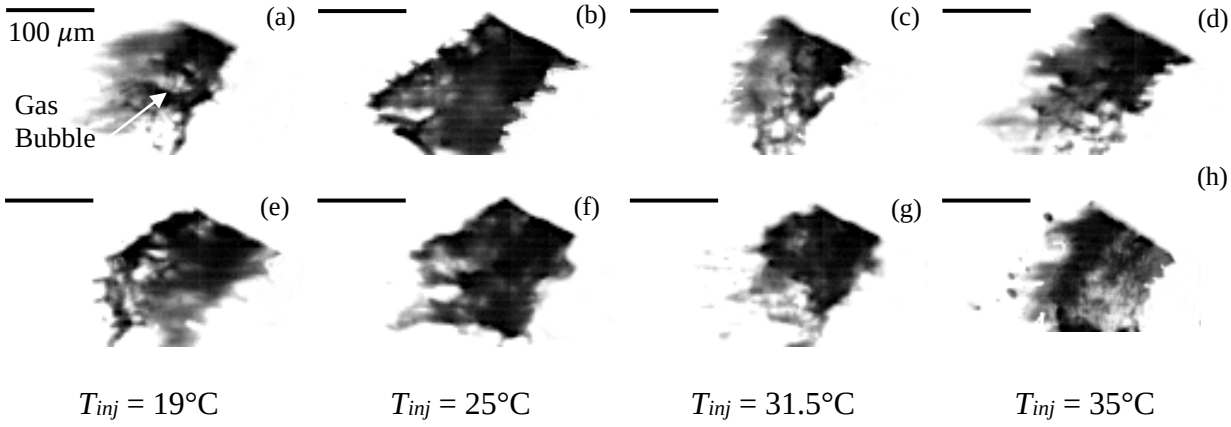

Figure 31. High-speed images (420,000 fps): visualizing the effect of mixture temperature on the early development of the spray: (a – d) CO_2-A: P_{inj} =3 MPa and GLR =0.2; (e – h) CO_2-A: P_{inj} =6 MPa and GLR =0.2. All snapshots are taken at 19.05 $\boldsymbol{\mu}$s. The scale bar (100 $\boldsymbol{\mu}$m) is identical for all images.

Finally, we focus on subcritical injection pressures (3 and 6 MPa) with injection temperature varying between 19 to 35 ºC for CO_2-A that according to the phase-diagram depicted in **Figure 21** represents a two-phase system at equilibrium. Since the solubility is quite lower at

subcritical pressures, we expect that the major mechanism driving the instability in these cases is the ejection of a two-phase bubbly flow more like the effervescent atomization rather than separation of the dissolved CO_2 as discussed for 7.5 and 9 MPa. **Figure 31a** shows that a relatively large gas bubble appears within the liquid core at 19 ºC that grows with time. By increasing the temperature from 19 to 25 ºC, the solubility decreases. As a result, the liquid core length increases more noticeably at 3 MPa (**Figure 31a** and **b**). By approaching the critical temperature (**Figure 31c** and **g**), the liquid core decreases for both 3 and 6 MPa, again more evidently for 3 MPa. Both cases exhibit much smaller liquid structures and visible droplets at 35 ºC (**Figure 31d** and **h**) compared to 31.5 °C as the surface tension reaches a minimum at 35 ºC (**Figure 23c**). At P_{inj} = 6 MPa, increasing the injection temperature does not affect the spray morphology significantly (**Figure 31e** and **f**). This behavior is related to the solubility of CO_2 in water that decreases more drastically at lower subcritical pressures (e.g., 3 versus 6 MPa) with an increase in temperature as **Figure 23b** depicts.

In summary, at subcritical pressures, the breakup is enhanced at subcritical temperatures where the CO_2 solubility in water is higher. Near the critical pressure, the solubility is enhanced noticeably and increasing the temperature further lowers the surface tension where both effects promote atomization. At supercritical pressures, the solubility does not significantly increase compared to the solubility at the critical pressure; therefore, increasing the temperature mainly affect the surface tension. Thus, the early stages of spray morphology do not vary visibly with the temperature at supercritical pressures.

3.3.4 Pressure Effects on Secondary Breakup

Gas-to-liquid mass flow rate ratio (GLR) is a critical parameter in promoting the dissolved-gas atomization as it significantly influences the SMD. [200] SMD is defined as the diameter of a sphere with the same volume-to-surface area ratio as the droplet of interest. [201] To investigate the effects of GLR on SMD, GLR is varied from 0.025 to 4 by controlling the CO_2 (N_2) mass flow rate through the pump, keeping the water mass flow rate constant for CO_2 (N_2)-A systems. The measured SMD versus GLR at 25 ºC with different injection pressures at three locations downstream of the nozzle, i.e., 10, 15, and 20 cm is plotted in **Figure 32**. To portray the sensitivity of SMD to GLR, we magnified a portion of the graph on the same plot to focus on the lower GLRs. It is observed from **Figure 32 (a-c**) that the mean droplet size decreases with an increase in the injection pressure as GLR increases. As the magnified plots depict, the rate of SMD reduction decreases with an increase in GLR. After a certain GLR, the SMD does not change noticeably and the rate of SMD reduction reaches a plateau; further increasing GLR does not notably change the mean droplet size. However, for lower injection pressures (e.g., 3 and 6 MPa), the droplet size becomes invariant at higher GLRs compared to that of 7.5 and 9 MPa. Comparing the SMD versus distance from the nozzle at the same injection pressure in **Fig. 13 (a-c)** depicts that SMD at a further distance with respect to the nozzle is less affected by an increase in the GLR for all injection pressures.

It is shown in **Figure 32 (a-c)** that the difference between SMD of 7.5 and 9 MPa injection pressure increases with distance from the nozzle that can be linked to the secondary atomization. To illustrate this effect on the relationship between the SMD and GLR, **Figure 33** compares SMD at three different vertical locations with respect to the nozzle for each injection pressure, i.e., 3, 6,

7.5, and 9 MPa. The focus is on lower GLRs in this figure where the rate of change of SMD is much higher. **Figure 33** illustrates an interesting behavior at 7.5 MPa: closer to the nozzle at 10 cm, the droplet size drops and reaches that of 9 MPa by a small increase in GLR from 0.025 to 0.05 and it remains unchanged with an increase in GLR and further from the nozzle (i.e., 15 and 20 cm). Therefore, a more uniform distribution along the axis of the spray is achievable at 7.5 MPa. However, SMD continuously decreases with distance from the nozzle at lower (3 and 6 MPa) and higher injection pressures (9 MPa) compared to 7.5 MPa. This trend corroborates that at 7.5 MPa, smaller droplets (SMD ~ 3 μm) are formed mainly due to the primary atomization closer to the nozzle. It can be deduced that the secondary atomization is responsible for SMD decrease at injection pressures away from the critical point (i.e., 3, 6, and 9 MPa) and further away from the nozzle. The overall trend reveals that an increase in the dissolution of CO_2 in water near the critical pressure of the water-CO_2 system at 7.5 MPa enhances the primary atomization irrespective of the GLR. In general, the smallest droplet size can be created with an injection pressure of 7.5 MPa and $0.05 < GLR < 0.2$ at 10 cm downstream of the nozzle. In addition, since SMD does not vary significantly with the distance from the nozzle at 7.5 MPa (**Figure 32c**) it corroborates a more uniform droplet distribution is achievable at the critical pressure which significantly improves the system's efficiency. This behavior has significant implications for designing supercritical-assisted atomization systems as small droplet sizes are generated at low GLRs by operating near the critical pressure of the mixture, and thus there is no need for excessive use of the assisting fluid or increasing the injection pressure to achieve the same mean droplet size is more homogenous.

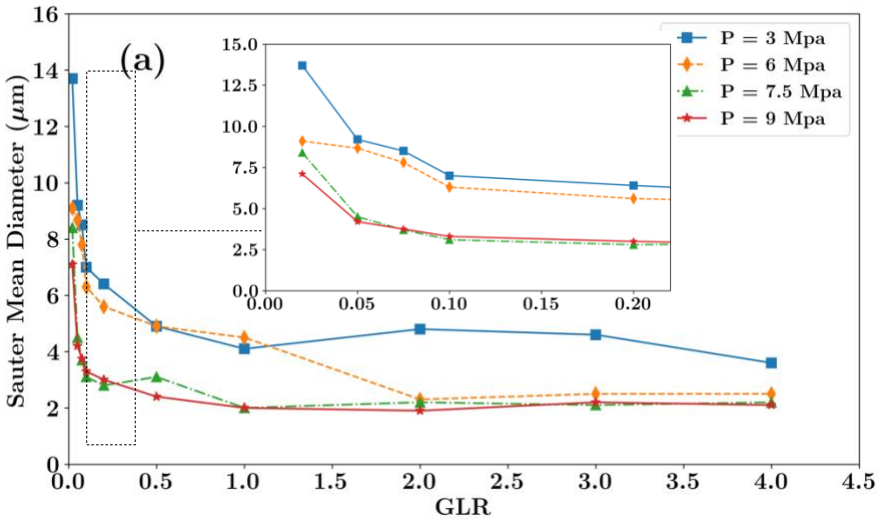
(a)
P = 3 Mpa
P = 6 Mpa
P = 7.5 Mpa
P = 9 Mpa
Sauter Mean Diameter (μm)
GLR

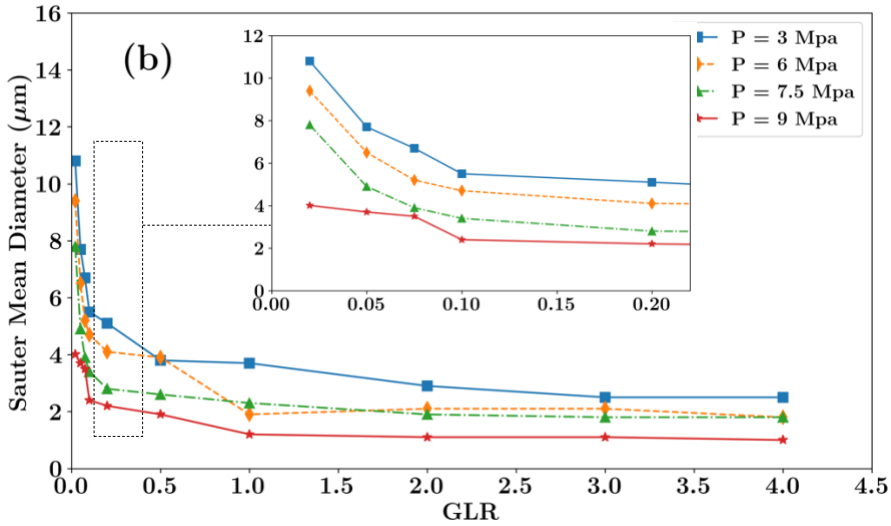
(b)
P = 3 Mpa
P = 6 Mpa
P = 7.5 Mpa
P = 9 Mpa
Sauter Mean Diameter (μm)
GLR

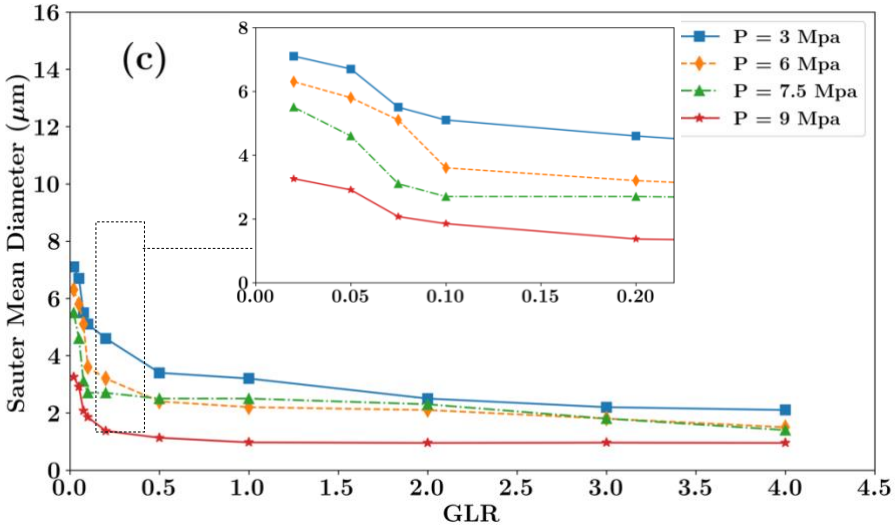

Figure 32. SMD as a function of GLR at different injection pressures measured axially w.r.t the nozzle at (a) 10 cm, (b) 15 cm and (c) 20 cm for CO_2-A at 25 ºC.

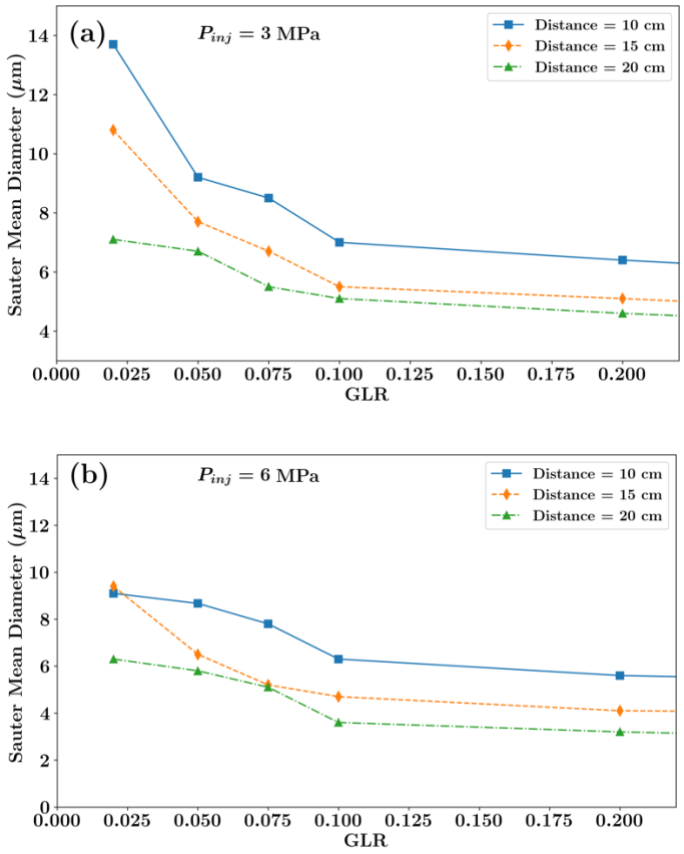

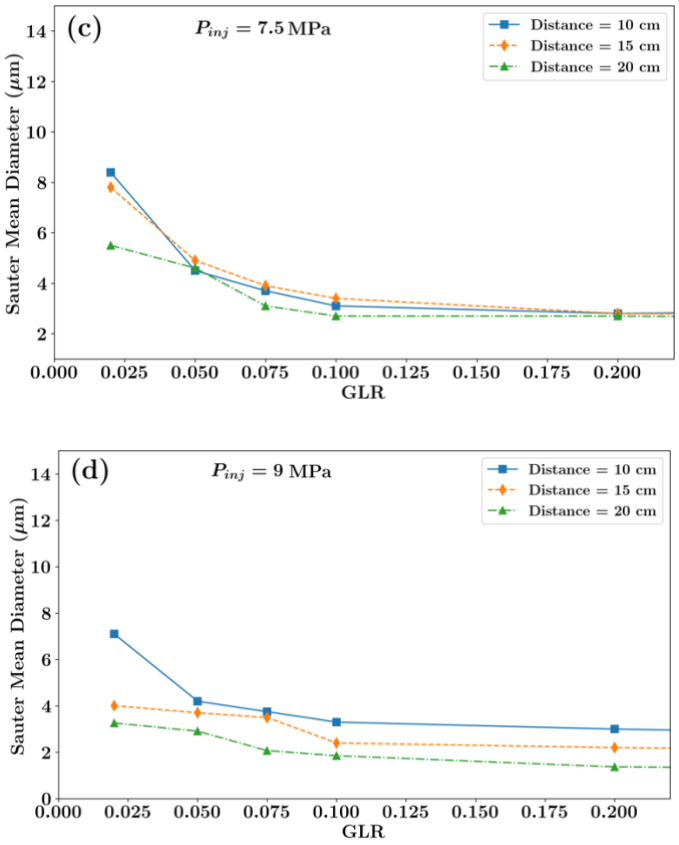

Figure 33. SMD as a function of GLR measured at (a) 3 MPa, (b) 6 MPa, (c) 7.5 MPa, and (d) 9 MPa injection pressures for CO_2-A at 25 ºC.

Figure 34 shows the variation of SMD with respect to GLR where N_2 is utilized as the atomization gas. Like CO_2-A, increasing the GLR and injection pressure decreases the SMD. However, the rate of SMD reduction is lower compared with CO_2-A and a plateau is not reached within the tested GLRs even up to a GLR equal to 4. Using either CO_2 or N_2, the droplet sizes become smaller further away from the injection nozzle due to the secondary atomization. The SMD is approximately a factor of two larger in N_2-A spray for all tested injection pressures and GLRs. This is consistent with the behavior of the primary break up illustrated in **Figure 27** that showed the lower mole fraction of dissolved N_2 in water and higher surface tension of the N_2-

water mixture retard the atomization process compared to CO_2-A that eventually leads to larger droplet sizes.

Figure 35 compares the relative span factor (RSF) for CO_2 (N_2)-A at different GLRs to better demonstrate the effect of GLR on the SMD size distribution. Lower RSF values imply a more uniform droplet size distribution. The relative span factor (RSF) is a non-dimensional parameter defined as $\frac{Dv90-Dv10}{Dv50}$ where *Dv90 (Dv10)* are arithmetic mean diameters representing 90% (10%) of the total volume of liquid droplets with diameters larger than median value; the median diameter implies 50% of the droplets are larger than the median and 50% are smaller. [202] **Figure 35** shows that CO_2 has generated a more uniform distribution of droplet sizes (lower RSF) compared to N_2 at all tested GLRs and injection pressures while RSF decreases with an increase in pressure for both N_2-A and CO_2-A sprays. In general, the increase in GLR has a more pronounced effect on lowering the RSF for N_2-A spray compared with CO_2-A. For example, by increasing GLR from 0.05 to 2 at 3 MPa injection pressure and 25 ºC temperature, the RSF of CO_2-A spray stays almost the same, while the RSF of N_2-A experience a 12.5% reduction. The changes in RSF versus pressure is more noticeable for the CO_2-A. At 7.5 and 9 MPa, CO_2-A exhibits a lower RSF, i.e., a very narrow droplet size distribution compared to N_2-A at the same pressure. Particularly, the lowest RSF occurs near the critical point, i.e., at 7.5 MPa for all tested GLRs. This behavior corroborates our observation from **Figure 33** that showed SMD did not change notably at different spray cross-sections at 7.5 MPa. **Figure 35** depicts that further increasing the pressure to 9 MPa has an adverse effect on RSF. This behavior confirms our earlier observation that degassing of the dissolved CO_2 in water that increases near the critical point is the main mechanism driving the liquid instability.

3.3.5 Temperature Effects on Secondary Breakup

According to the SMD vs. GLR plots at T_{inj}= 25 ºC shown in **Figure 33**, the SMD curve reaches a plateau at GLRs above 0.2 for CO_2-A; indicating that there is no need for supplying excessive amounts of CO_2 in the system to achieve small droplets for CO_2-A. Therefore, to investigate the effect of injection temperature on droplet sizes, the injection temperature is increased from 25 to 31.5 and 35 ºC and SMD is measured at a constant GLR = 0.2.

Figure 36 demonstrate a slight increase in SMD by increasing the temperature and decrease in SMD with an increase in injection pressure for both N_2-A and CO_2-A. For the CO_2-A spray at subcritical pressures (i.e., 3 and 6 MPa), the increase of SMD with temperature is more evident than at near-critical and supercritical pressures (i.e., 7.5 and 9 MPa) where SMD remains almost identical at 25 ºC, 31.5 ºC, and 35 ºC. Particularly at 9 MPa, the variation of SMD with temperature is negligible (less than one micron). This observation suggests that although the solubility of CO_2 reduces and the amount of dissolved gas in the mixture decreases with an increase in temperature, the surface tension reduction promotes the breakup process for supercritical pressures at higher temperatures. In other words, the effect of lower solubility is compensated by the lower interfacial tension of the mixture above the critical point that reaches a minimum at 35 ºC (**Figure 23c**). However, at subcritical pressures where a two-phase mixture prevails, the solubility of gas and bubble growth mechanism plays a more important role in facilitating the breakup process than the reduction in interfacial tension with a temperature increase; thus, at subcritical pressures, SMD is more sensitive to the changes in solubility with temperature. These results are consistent with the high-speed images of spray (**Figures 29-31**).

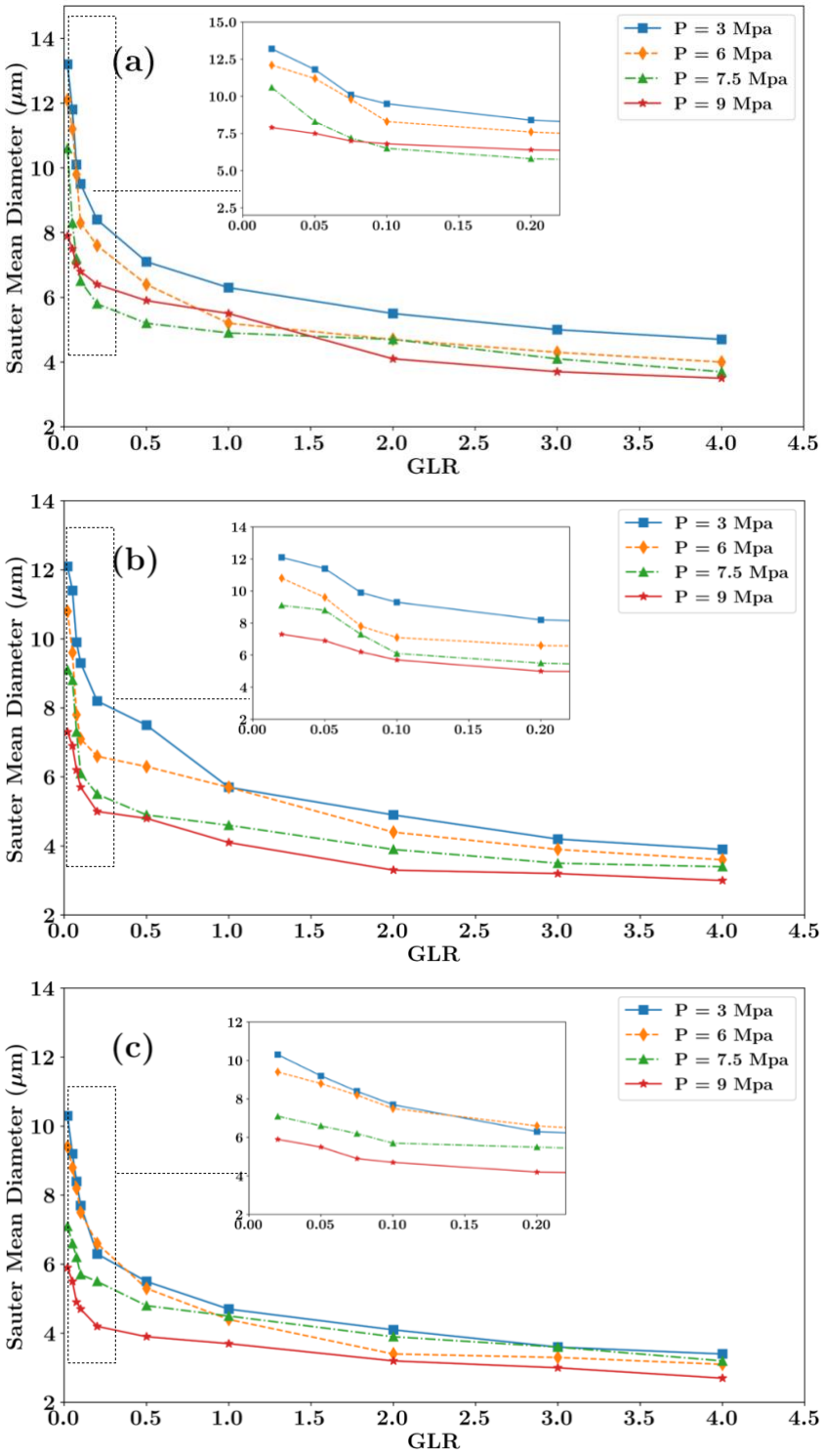

Figure 34. SMD as a function of GLR at different injection pressures measured axially w.r.t the nozzle at (a) 10 cm, (b) 15 cm and (c) 20 cm for N_2-A at 25 ºC.

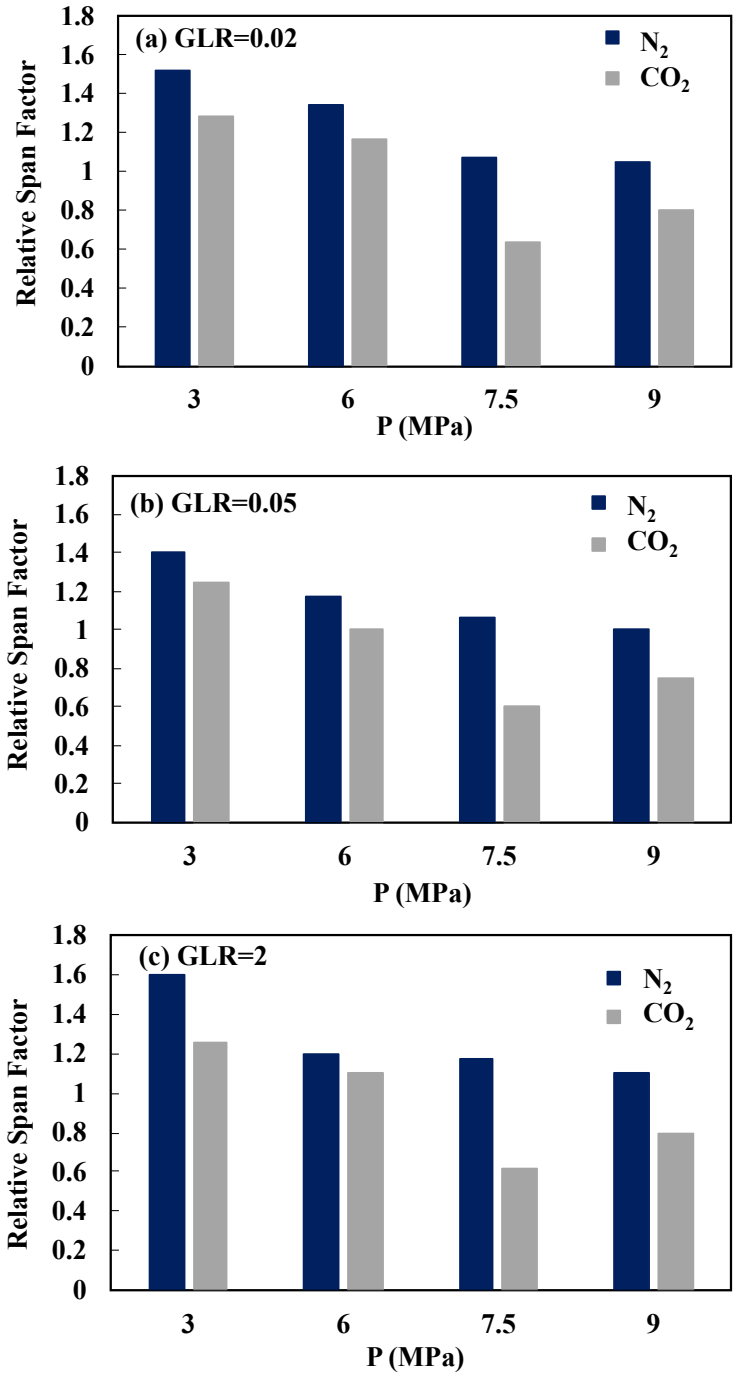

Figure 35. RSF of droplet sizes as a function of injection pressure for CO_2-A and N_2-A sprays measured at 10 cm axial location at T_{inj}= 25 ºC for (a) GLR = 0.02, (b) GLR = 0.05, (c) GLR = 2.

SMD measured for N_2-A varies more noticeably with temperature compared to CO_2 at all pressures. As was shown in **Figure 23d**, although the solubility of N_2 in water is much lower than CO_2, it reduces more steeply with temperature. Increasing temperature from 25 ºC to 35 ºC results in a ~15% reduction in solubility of N_2 in water versus ~ 9% for CO_2. [189] Consequently, less dissolved N_2 implies fewer bubbles formation that negatively affects the atomization process and leads to an increase in the droplet sizes with an increase in temperature. It is noted that in contrast to the CO_2-A, such gas bubbles were not visible in high-speed images of N_2-A.

The RSF of droplet sizes at GLR equal to 0.2 at 25, 31.5, and 35 ºC for both N_2-A and CO_2-A at 10 cm from the nozzle is shown in **Figure 37**. For CO_2-A spray, the lowest RSF occurs at 35 ºC for all pressures except for 7.5 MPa where the lowest RSF occurs at 25 ºC. This behavior corroborates that increasing the temperature at the critical pressure does not have a profound effect on the homogeneity of the droplet distribution close to the nozzle. Away from the critical pressure however, the surface tension reduction at 35ºC enhances the droplet size homogeneity across the spray cross-section. By increasing the temperature in N_2-A, RSF varies more evidently compared to the CO_2-A consistent with the wider SMD range observed in **Figure 36.** In summary, by operating near the critical pressure of the CO_2-water mixture, smaller droplets and homogenous size distribution can be achieved even at subcritical temperatures. At supercritical pressures where the solubility does not significantly increase compared to the solubility at the critical pressure, smaller droplets with a narrow size distribution are obtained at supercritical temperatures due to lower surface tension. Operation at subcritical pressures where less amount of gas is dissolved in water the mix creates much larger and less uniform droplet size distribution, especially at supercritical temperatures. Thus, by operating near critical pressure and subcritical or near-critical

temperatures, the need for ultrahigh pressures, high temperatures, and high GLR to generate a more uniform droplet size can be eliminated in CO_2-A systems.

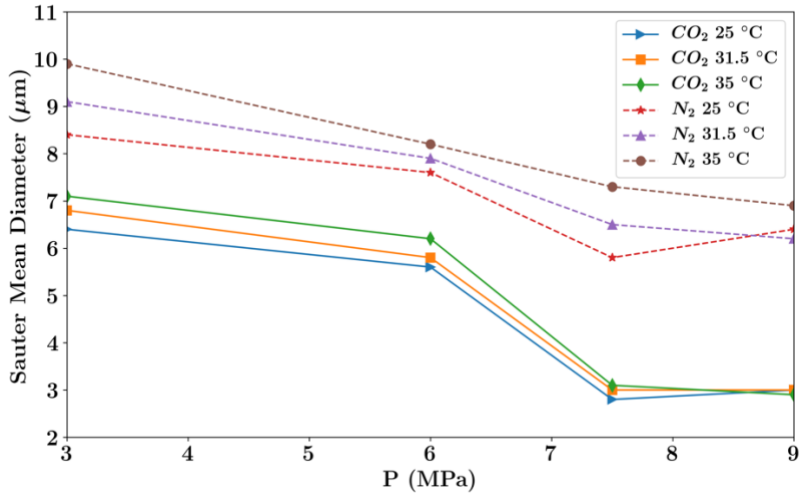

Figure 36. SMD as a function of injection pressure for N_2-A and CO_2-A measured at 10 cm from the nozzle at different injection temperatures and pressures.

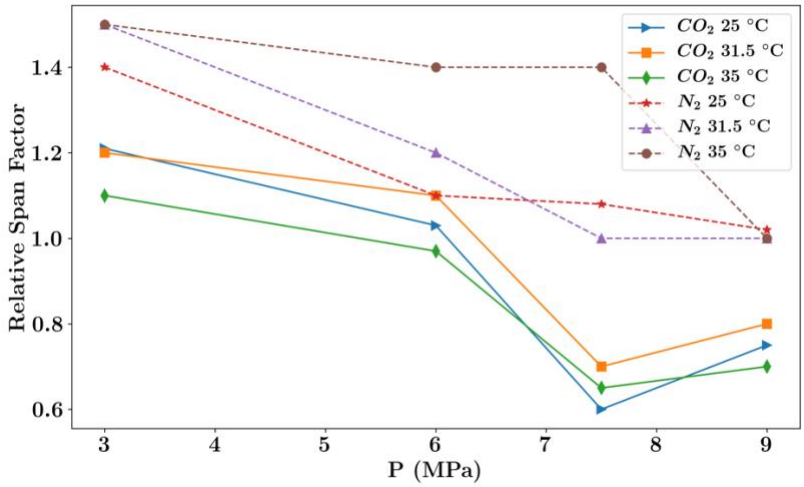

Figure 37. RSF of droplet sizes as a function of injection pressure for CO_2-A and N_2-A sprays measured axially from the nozzle at 10 cm for GLR = 0.2 for T_{inj}= 25 ºC, 31.5 ºC, and 35 ºC.

3.3.6 Linear Instability Analysis

Although the behavior of the liquid jet containing dissolved gas has a non-linear nature and involves an amalgamation of different instability mechanisms, it is still useful to study the predictions of linear instability theory; especially, to identify the wavelengths with the fastest growth rates. Disintegration and breakup of a liquid jet and droplet formation is widely accepted to be a result of the growth of different hydrodynamic instabilities, mainly Kelvin-Helmholtz (KH) or shear instability and Rayleigh-Taylor (RT). RT instability can result from the fluid acceleration acting at the liquid-gas interface that has primarily been exposed to the KH instabilities risen because of the interfacial shear between the liquid and gas. While the liquid jet becomes unstable after injection and breaks up into ligaments due to KH instabilities, the breakup and droplet formation is mainly attributed to the growth of RT instabilities arising from density difference and acceleration imposed on the liquid-gas interface. [203-205] For a heavy fluid over a light fluid, the classical RT instability theory neglects the effects of viscosity and surface tension and suggests the instabilities of a flat free surface in such system grow exponentially with a growth rate of $\omega = [k\frac{\rho_2-\rho_1}{\rho_2+\rho_1}g]^{1/2}$, where ω denotes the temporal growth rate, k is the wavenumber, g is the gravitational acceleration and ρ_1 and ρ_2 indicate the density of the light and heavy fluids, respectively. [206] By neglecting the effects of surface tension and viscosity shorter wavelength can grow indefinitely since both surface tension and viscosity potentially damp short wavelengths. However, Chandrasekhar instability theory suggests [207] that there is a finite RT wavelength (λ_{RT}) with a maximum growth rate that depends on both acceleration (a) and surface tension (σ) as follows,

$$\lambda_{RT} = 2\pi\sqrt{\frac{3\sigma}{(\rho_l-\rho_g)a}}, \quad (1)$$

where ρ_l and ρ_g refer to the liquid and gas density, respectively. In general, four physical phenomena control the hydrodynamic instability: (1) inertial differences across the shear layer that contribute to the KH (shear) instability, (2) acceleration imposed on the interface that contributes to the RT instability, (3) viscous effects, and finally (4) surface tension that activates the capillary instability. Equation 3 shows the dispersion equation developed by Joseph et al., [208] indicating the temporal growth rate of instabilities as a function of wavelength where the four dominating effects are taken into account. It is worth noting that although this relation was obtained for the instability analysis of viscous potential flows with an initially planar interface, it has been shown to provide useful insights into the instability of round liquid jets at high injection pressure. [209]

$$\omega = -k^2\frac{\mu_l+\mu_g}{\rho_l+\rho_g} \pm \left[\rho_l\rho_g k^2\left(\frac{u_l-u_g}{\rho_l+\rho_g}\right)^2 - k\frac{\rho_l-\rho_g}{\rho_l+\rho_g}g - \frac{k^3\sigma}{\rho_l+\rho_g} + k^4\left(\frac{\mu_l+\mu_g}{\rho_l+\rho_g}\right)^2\right]^{\frac{1}{2}}, \quad (3)$$

where ω denotes the temporal growth rate of instabilities, k is the wavenumber, g is the gravitational acceleration that can be replaced with the acceleration at the liquid-gas interface, and ρ_l, ρ_g, μ_l, and μ_g indicate the density and viscosity of the liquid and gas, respectively.

Since different instability mechanisms dominate at different length scales, we investigate the growth rate of instabilities for both liquid jet and ligaments. The liquid jet has a circular cross-section and ligaments are detected on the periphery of the core jet in the high-speed images of the spray (**Figure 28d**). For this analysis, density, viscosity, and surface tension of the liquid have been obtained from the experimental data portrayed in **Figures 23-24.** The initial velocity of the jet right at the nozzle exit before the growth of non-linear instabilities is estimated given the

pressure difference between the liquid mixture and the ambient air, the nozzle diameter (125 μm), and the density of the CO_2-water or N_2-water mixture for injection pressures of 7.5 and 9 MPa. We selected these two injection pressures for this analysis as we showed earlier that the instability mechanisms became more complex at critical and supercritical pressures where the competing effects of surface tension and solubility are simultaneously involved. To calculate the velocity and acceleration of the liquid jet (ligaments), we manually tracked the head of the liquid core (ligaments) identified on the selected high-speed images in consecutive frames and measured the distance traveled by the tip of the liquid core (ligaments) over each time interval. Since the gravitational acceleration is insignificant compared to the calculated acceleration, we replaced it with the acceleration of the jet (ligaments) in Eqn. 2, measured by manual post-processing of the high-speed images. **Table 8** outlines the fluid properties, velocity, acceleration of the jet and ligaments, and experimental and theoretical RT wavelengths, and capillary time scales.

Table 8. Properties of the liquid jet/ligaments and unstable wavelengths and capillary breakup time.

Case	P_{inj} (MPa)	σ (N/m)	u_l (m/s)	$a\times10^6$ (m/s^2)	D (μm)	λ (μm) Experiment	λ_{RT} (μm)	t (μs) Experiment	t_σ (μs)
CO_2-A jet	7.5	0.0296	122.1	8.0	117.0	19.1	20.8	95.2	234.8
	9	0.0296	134.4	8.8	109.0	17.2	19.9	128.5	211.1
CO_2-A ligament	7.5	0.0296	128.0	9.9	18.5	11.7	18.7	4.8	14.8
	9	0.0296	138.3	9.9	15.3	10.6	18.6	9.5	11.1
N_2-A jet	7.5	0.0669	121.0	7.8	119.0	27.6	31.5	119.0	158.8
	9	0.0661	133.1	8.7	117.0	25.4	29.9	114.3	155.7
N_2-A ligament	7.5	0.0669	124.2	9.2	19.1	14.9	29.2	9.5	10.2
	9	0.0661	136.1	9.7	17.5	13.8	28.2	9.5	9.0

Figure 38 shows the real part of the growth rate of instabilities obtained from Eqn. 2 as a function of wavelength for the liquid jet for CO_2-A (**Figure 38a-b**) and N_2-A (**Figure 38c-d**) at

two different injection pressures (P_{inj}= 7.5 and 9 MPa, both at T_{inj}=25 ºC) using the parameters discussed above and detailed in **Table 8**. The positive values of the growth rate indicate unstable regions. To identify the dominating factor driving the instabilities, the contribution of surface tension, viscosity, combined inertia and acceleration, and inertia has been plotted individually in **Figure 38**. Considering all contributing effects, the growth rate of instabilities is higher for the CO_2-A than N_2, increasing with the injection pressure, which can be attributed to higher velocity and acceleration and lower surface tension for CO_2-A. This is consistent with the snapshots of the spray development (**Figures 29-30**) and SMD measurements (**Figure 33**) that showed longer breakup length and larger SMD for N_2-A at the same injection pressures and temperature. The range of the unstable wavelengths predicted by the growth rate analysis, i.e., O (10^{-5} m) is consistent with the wavelengths measured from the high-speed images during the first 23 µs after the start of injection. Unstable wavelengths at the periphery of the liquid jet (λ_{jet}) and the wavelength detected on the ligaments (λ_l) are exemplified in **Figure 28d**.

It is observed from **Figure 38** that the surface tension has a stabilizing effect at sub-millimeter wavelengths as neglecting surface tension drastically increases the growth rate in the presence of the inertial forces and acceleration. The stabilizing effect of surface tension is more pronounced for N_2-A mainly due to the higher surface tension of N_2-water compared to the CO_2-water mixture (**Table 8**) as the higher values of the growth rate indicate (**Figure 38c-d**). Viscous forces do not affect the instability of small wavelengths (i.e., sub-micron) and exhibit a stabilizing effect at wavelengths larger than ~10 μm. As the viscosity of the CO_2-water mixture is slightly higher than the N_2-water mixture at the same injection pressures and temperature, neglecting the viscosity marginally increases the growth rate of the CO_2-water jet. Finally, neglecting the inertia

and acceleration terms in the dispersion equation results in a lower growth rate of the liquid jet for both CO_2 and N_2-A; more in CO_2-A. When the combined effect of inertia and acceleration term is considered, and other terms are neglected (i.e., the square symbol purple line) the jet is highly unstable in both cases. **Figure 38** shows that by neglecting either acceleration (dashed orange) or inertia (dotted blue), the jet remains unstable; indicating that both effects are important in the promotion of instability.

The most unstable wavelength in both cases is consistent with the experiments (i.e., $O(10^{-5}$ m). The same analysis was performed for instabilities of ligaments. Since the rheological properties of the ligaments and the liquid jet are the same and their velocities and accelerations are close (slightly higher in case of ligaments in **Table 8**), similar behavior as the liquid jet is observed. The only difference in the case of ligament instabilities is that the most unstable wavelength shifts toward smaller wavelengths (not shown here for the sake of brevity). This is consistent with our experimental observations where the wavelengths formed on the ligaments are shorter than the wavelengths observed at the edge of the jet (**Figure 28d**).

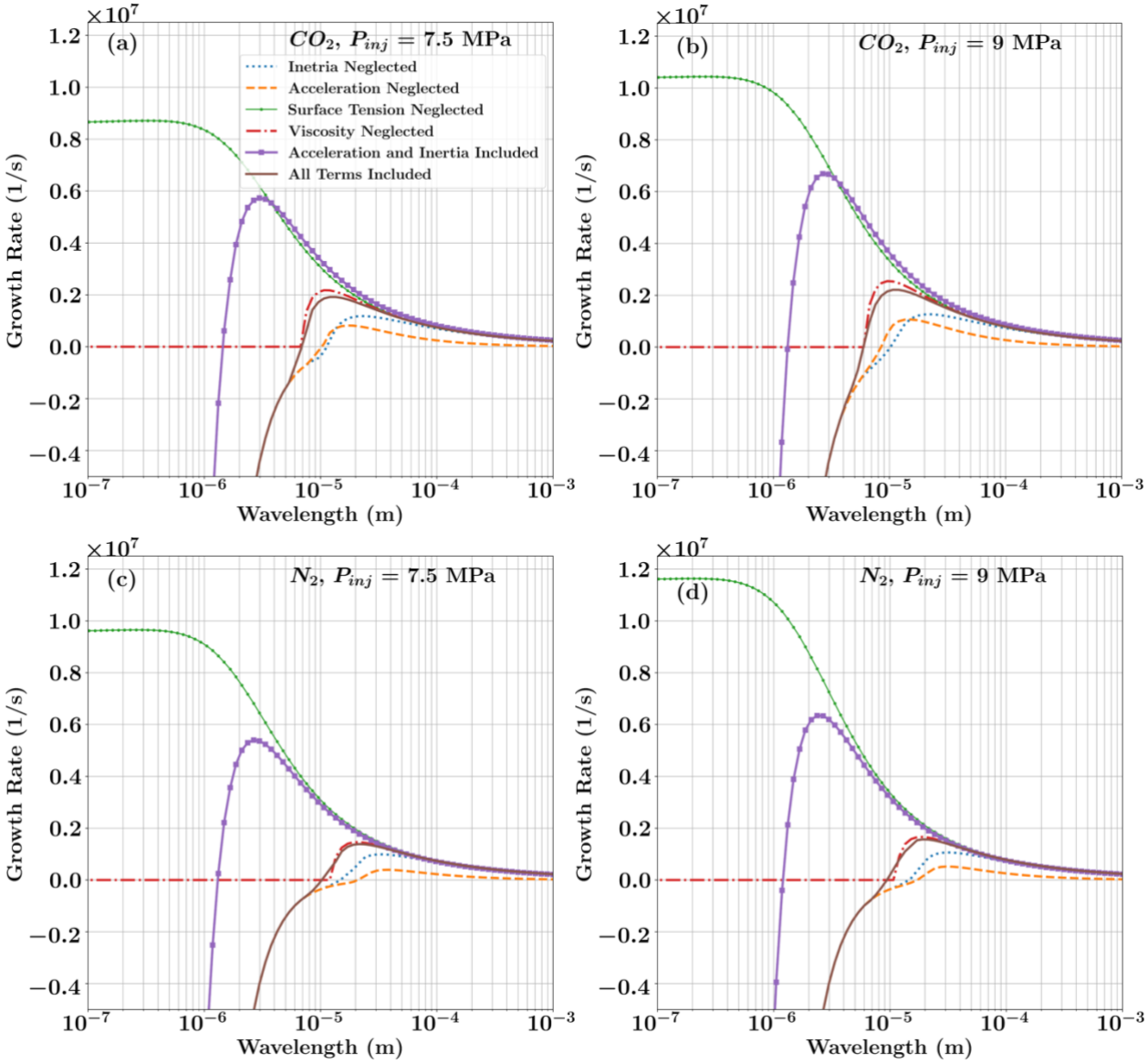

Figure 38. The real part of the linear growth rate of instabilities calculated for the liquid jet as a function of wavelength for (a) CO_2-A at P_{inj} = 7.5 MPa, (b) CO_2-A at P_{inj} = 9 MPa (c) N_2-A at P_{inj} = 7.5 MPa, and (d) N_2-A at P_{inj} = 9 MPa cases. T_{inj}= 25 ºC for all cases.

To decouple the effects of the inertia and acceleration terms on driving the liquid jet and ligament instabilities, the most unstable RT wavelength is calculated using the linear instability analysis of Chandrasekhar shown in Eqn. 1[207]. The theoretical RT wavelengths are compared with the measured wavelengths detected from the high-speed images in **Table 8**. The predicted

wavelengths for the jet are consistent with the experimental results; however, the theoretical wavelengths on the ligaments are longer than the experiments. This behavior suggests that the ligaments are more susceptible to capillary breakup. To explore the effect of the capillary breakup, we invoked the following equation proposed by Marmottant and Villermaux [210] that predicts the capillary breakup timescales of a cylindrical liquid jet as follows:

$$t_\sigma = \sqrt{\frac{\rho_l D^3}{\sigma}} f(Re). \quad (4)$$

where D, ρ_l, and σ represent the jet (ligament) diameter, liquid density, and surface tension coefficient, respectively. Re is defined as $Re = \sqrt{\frac{D\sigma\rho_l}{2\mu_l^2}}$ and $f(Re)$ is reported based on the experiments conducted in that same study. The capillary break-up time according to Eqn. 3 for N_2-A and CO_2-A jets and ligaments are presented in **Table 8**. The breakup times are captured in high-speed images where the first visible droplet is separated from the ligament. It is noted that a few droplets smaller than the resolving power of our system might have been broken from the ligaments earlier than reported in **Table 8**. The capillary timescale calculated for the jet and ligaments attributed to the CO_2-A is greater than the experimental breakup time. Especially, for CO_2-A at 7.5 MPa injection pressure, the measured timescales and wavelengths are much smaller than at 9 MPa case. The difference between the predicted and measured capillary timescales reduces for N_2-A. Particularly, a good agreement is observed for the ligaments generated through N_2-A while a comparison of the theoretical RT and experimental wavelengths shows a shorter wavelength than theoretical RT for the ligaments of N_2-A. This observation suggests that the acceleration effects caused by the separation of the dissolved gas and bubble burst are the main

mechanism driving the instabilities for CO_2-A. Therefore, for lower amounts of dissolved gas as in N_2-A, capillary breakup plays a major role in promoting the ligament breakup.

It is worth noting that the effect of the dissolved gas and the separation of the gas bubbles that lead to jet breakup and the non-linear effects inherited in the breakup process is not directly accounted for in the linear instability analysis presented in this section. In experiments, a two-phase mixture (CO_2/N_2-saturated water including CO_2/N_2 bubbles) is injected into ambient air which undergoes a phase change due to depressurization upon injection. According to the phase diagram (**Figure 22**), the solubility of CO_2 and N_2 in water reduces by decreasing the pressure (i.e., degassing). The degassing process exerts higher interfacial shear force and higher acceleration due to the spontaneous burst of the bubbles and both effects enhance the growth of instabilities during the early stages of the jet development (O(10) μs) considered in this study. The higher concentration of dissolved gas in CO_2-A, is attributed to a larger volume of bubbles that expand and burst, which justifies higher velocity and acceleration experimentally measured for the liquid jet, and especially higher acceleration for the ligaments. Consequently, the role of the dissolved gas in enhancing the growth of instabilities is indirectly reflected in the inertia and acceleration terms of the linear instability analysis and their combined effect exhibits a higher growth rate for CO_2-A at comparable pressures. However, the spontaneous effect of the bubble burst in shattering the liquid jet that occurs at a fraction of microsecond has not been included in this theoretical analysis.

3.3.7 SMD Prediction Models

In this section, we first introduce the model of Lund, which is commonly used as a benchmark for predicting the SMD in effervescent atomization. We then introduce the

methodologies used for developing an empirical SMD model in this work and compare the experimentally measured SMD with model predictions. Equation 5 represents the model of Lund:

$$SMD = 3\sqrt[3]{\frac{3}{2}\sqrt{2}\pi D^3\sqrt{1+\frac{3\mu_l}{\sqrt{\rho_l\sigma D}}}}, \quad (5)$$

where D, ρ_l, σ and μ_l represent the ligament diameter, density, surface tension, and viscosity, respectively. To better represent the comparison between the experimental measurements of SMD data obtained for N_2-A and CO_2-A with the model of Lund, we deployed two different machine learning (ML) analyses, i.e., multiple-regression and gradient boosting to train a predictive model of SMD. Droplet sizes obtained from laser measurements for different injection pressures, GLR, axial distance from the nozzle, solubility of the dissolved gas in water, and injection temperature have been incorporated to train the abovementioned ML models. As part of an exploratory data analysis prior to model training, we created a correlation matrix based on Pearson's Product-Moment correlation, [211, 212] to find the pairwise correlation of the independent input variables. The correlation matrix is commonly used to summarize the data and find the existing patterns between variables for large datasets as a diagnostic input for ML analyses. Stronger correlations are represented by a higher correlation coefficient (*C*). With SMD representing the response variable, GLR shows the highest correlation (*C*= 0.55) among the independent variables, followed by the solubility of the atomization gas (*C*= 0.50), injection pressure (C= 0.38), axial distance from the nozzle (*C*= 0.24), and injection temperature (*C*= 0.12). These correlations were expected as we showed the significance of GLR and gas solubility on the SMD predictions in **Figures 31-33**. The injection temperature exhibits the weakest correlation with the SMD. This is expected as **Figure 36** depicts less than a one-micron difference in SMD by increasing the temperature from 25 to 35

ºC keeping the same injection pressure for CO_2-A. Therefore, the effect of temperature variation has not been included in this model and the SMD measured at 25 °C is considered in the ML analysis.

Figure 39 portrays the distribution of SMD as a function of the solubility of the atomizing gas in water using a box plot. This figure portrays the integrated SMD measurements obtained at 25 ºC for all variables including different injection pressures, GLR, axial distance from the nozzle, and the solubility of the dissolved gas in water. Box plots graphically represent the minimum and maximum data points excluding the outliers (diamond symbols in **Figure 39**) by lower and upper whiskers, and the interquartile range using a box. The lower bound of the box, the line in the middle, and the upper bound of the box shows the first quartile, median and thirds quartile, respectively. Each value of the solubility in the plot corresponds to a certain pressure and atomizing gas as annotated in **Figure 39**. This plot shows that CO_2-A generates smaller and a more uniform SMD distribution as the solubility increases with pressure. Overall, it also predicts smaller droplets compared with N_2-A. Particularly, it is evident from this figure that the lowest and the narrowest SMD size distribution occurs at 7.5 MPa for CO_2-A. This behavior is consistent with SMD vs. GLR shown in **Figures 31-33**.

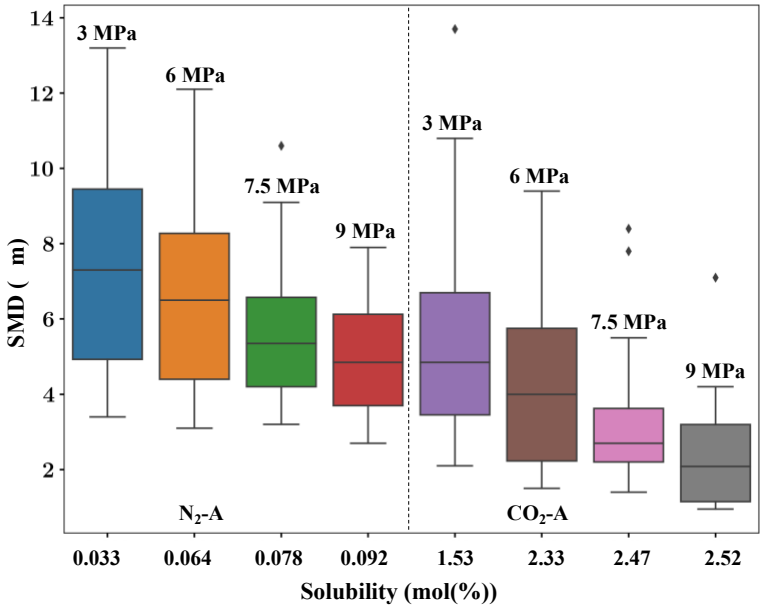

Figure 39. SMD distribution as a function of solubility of the dissolved gas for all experimental data set for both N_2-A and CO_2-A including different injection pressures, GLR, axial distance from the nozzle, and solubility of the dissolved gas in water at T_{inj}= 25 ºC.

For training the multiple-regression and gradient-boosting ML algorithms utilized in this study, 75% of the total empirical data points are used and 25% is employed as test cases. This model is developed based on the measured SMD for 3-9 MPa pressure, 0.02-4 GLR, 0.03-2.5 mol% gas solubility, and axial distance from the nozzle, i.e., 10, 15, and 20 cm. Investigating the data also indicates that SMD has a log-normal distribution; thus, the prediction model has been developed for $\ln(SMD)$ as displayed in **Figure 40** compared to the experimentally measured values. The accuracy of each model is evaluated based on the R^2 coefficient of determination that is 0.79 and 0.99 for the multiple-regression and gradient boosting methodologies, respectively. The multiple-regression model presents the following empirical relationship between SMD and the playing parameters:

$$\ln(SMD) = -7.37 \times 10^{-2} P - 0.27\, S - 0.25\, GLR - 0.03 L + 2.96. \quad (5)$$

where *P*, *GLR*, *S*, and *L* represent the injection pressure, gas-to-liquid ratio, the solubility of the dissolved gas in water, and axial distance from the nozzle, respectively. As was shown earlier, the effects of temperature on SMD prediction are much less pronounced compared to the injection pressure and GLR, and thus was removed from this analysis. Unlike the multiple-regression model, the gradient boosted tree does not offer a straight-forward relationship between the independent and response variables. However, the gradient boosted tree model more accurately predicts the non-linear relationship between SMD and independent variables as it is not constrained by the linearity assumption. [213, 214] Moreover, the gradient boosted model is a powerful ensemble-based model that allows achieving higher accuracies by combining multiple algorithms to improve otherwise weak models. [215, 216] Gradient boosting starts by fitting a model to the response variable. Then it fits a second model to the residuals of the first model (i.e. the difference between the outcome of the first model and the tested dataset); thus, models are improved sequentially until the desired accuracy is achieved. [217, 218]

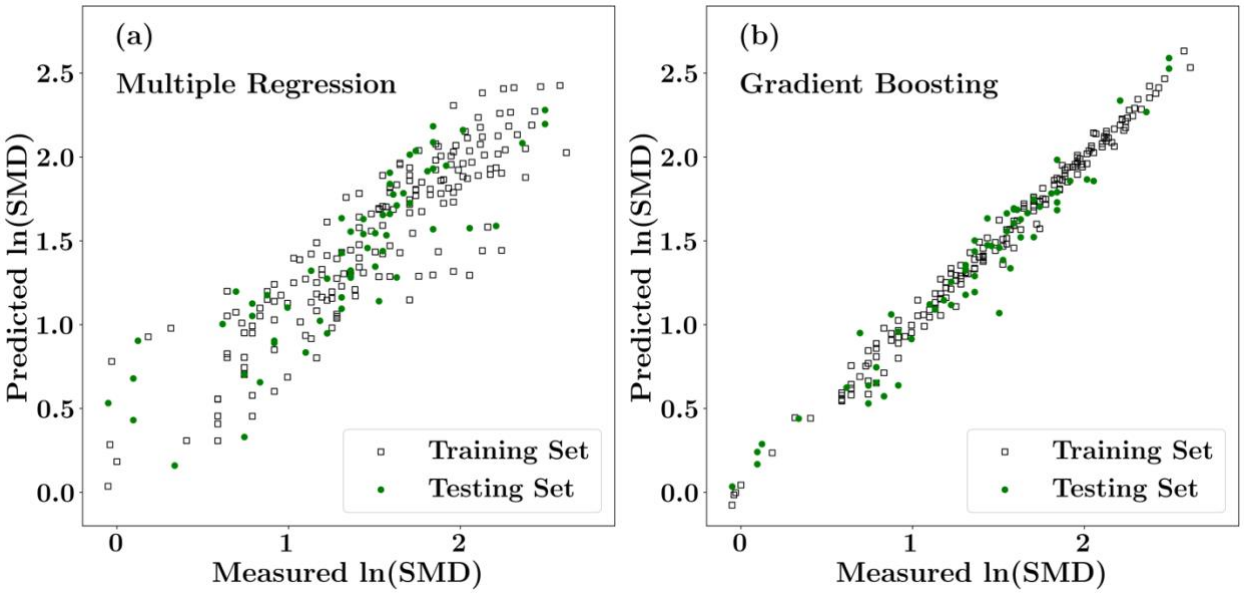

Figure 40. Predicted $\ln(SMD)$ versus measurements using (a) multiple-regression and (b) gradient boosted tree ML methodologies. The same training set has been used for both methods.

Figure 41 compares the experimental measurements of SMD for CO_2-A and N_2-A as a function of the injection pressure with the predictions of Lund, multiple-regression, and gradient boosting models. The measured SMD shown in this figure is attributed to GLR of 0.02 and 10 cm from the nozzle at 25 ºC. The ligament diameters implemented in the Lund model are captured from the high-speed images and the corresponding rheological properties (i.e., density, surface tension, and viscosity) of the gas-liquid mixtures are obtained from **Figures 23-24**. The model of Lund correctly predicts that N_2-A generates larger droplets compared to CO_2-A. This figure also shows that the gradient boosting model closely predicts the measured SMD. However, the model of Lund significantly overestimates the droplet sizes for both CO_2-A and N_2-A. The shortcomings of this model are attributed to the fact that (1) the effects of relative velocity between the ligaments and the surrounding gas medium as well as acceleration of the liquid at the liquid-gas interface that becomes considerable due to the bubble burst are not accounted for in this model, and (2) it

does not consider the effect of secondary atomization. In addition, the gas-assisted atomization near the critical point triggers a sudden increase in the diffusion and a drop in surface tension that have not been accounted for in the literature to date.

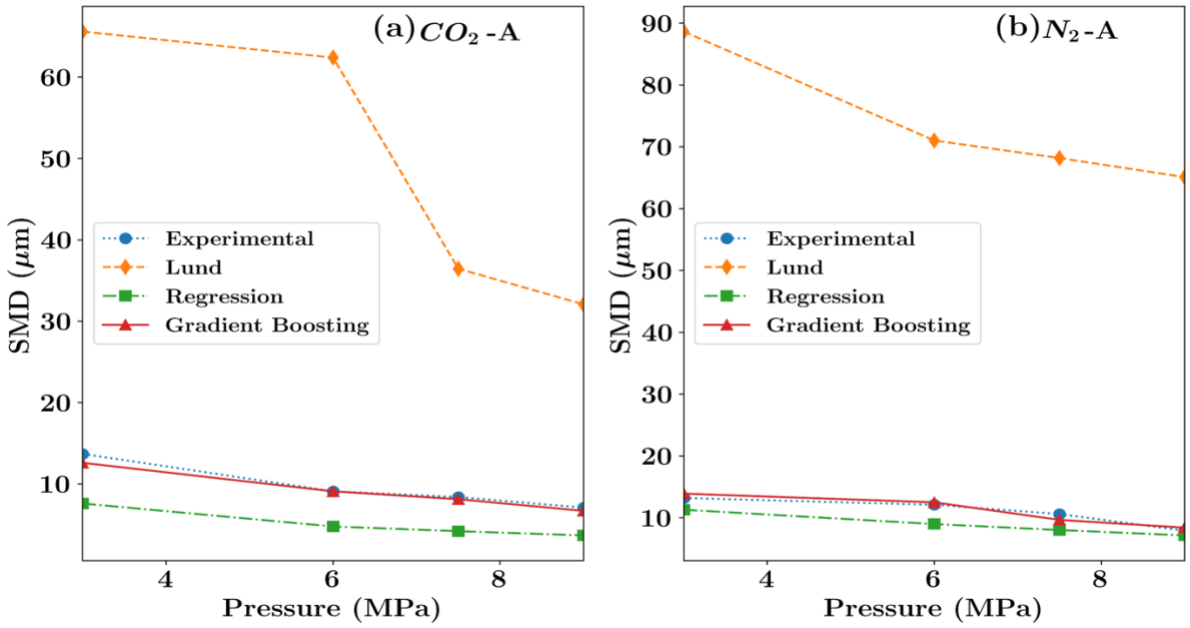

Figure 41. Comparison of SMD predicted by the Lund, multiple-regression and gradient boosting models with the experimental measurements as a function of injection pressure, at T_{inj} = 25 °C, GLR = 0.02, and L = 10 cm for (a) CO_2-A and (b) N_2-A.

3.3.8 Secondary Breakup Regimes

Comparing the Lund SMD model predictions with the experimental measurements revealed that secondary atomization is one of the key players in dictating the final size of the droplets that form downstream of the injection nozzle. In addition, as **Figure 33** suggests, the droplet sizes significantly vary with distance from the nozzle for both subcritical and supercritical pressures. At 7.5 MPa injection pressure, however, a very uniform distribution of the droplets was observed. Thus, in this section, we focus on different secondary atomization regimes that involve

the deformation of the droplets resulted from the primary breakup of the liquid jet. According to the experimental data in the literature, the secondary droplet breakup mechanisms have been categorized into five different modes based on the Weber number (*We*) and Ohnesorge number (*Oh*). [199, 219] *We* is defined as the ratio of inertial to surface tension forces as $We = \frac{\rho_g u_l{}^2 D}{\sigma}$, where ρ_g and σ represent the ambient gas density and surface tension of the gas-water mixture and u_l corresponds to the ligament velocity and *D* is the characteristic length, i.e. the ligament diameter that is closely related to the diameter of the primary droplets [220]. *We* is commonly used to analyze the likelihood of ligaments and droplets undergoing further breakup; however, the viscous effects affect the breakup regime governed by *We*. Viscosity retards droplet deformation by dissipating the incoming energy to the liquid. [199] *Oh* calculated as $Oh = \frac{\mu_l}{\sqrt{\rho_l \sigma D}}$, denotes the ratio of viscous to surface tension forces where ρ_l and μ_l represent the density and viscosity of the gas-water mixture. With an increase in viscosity, *We* required for initiating the breakup increases. Oscillatory deformation, i.e., vibrational breakup mode occurs for *We* less than 12. At these conditions, the inertial forces are not strong enough to completely overcome the surface tension at the liquid-gas interface. Although the droplets undergo mild deformation, they might not experience further breakup. [221] however, oscillations at the natural frequency of the droplet might generate a few droplets comparable to the size of the parent droplet. For *We* between 12 to 20, droplets experience the bag breakup mode, which entails the deformation of the droplets into a thin balloon-like structure that further shatters into smaller droplets. [222] For *We* between 20 to 80, different modes of breakup (aka multimode regime) have been observed. Finally, for *We* between 80 to 800, the shear breakup regime that involves deformation of the droplet into a thin

disk-shaped structure and deflection of the periphery of this disk into smaller droplets downstream of the flow is expected. [223] Droplets with *We* greater than 800 fall under the catastrophic breakup regime where parent droplets experience extreme deformation into various-shape fragments and small droplets. [219] This phenomenon typically occurs in internal combustion engines and shock tubes where the liquid is injected into a very high-pressure environment. The values reported for the critical *We* varies in the literature. In this study, the critical *We* is adopted from Chryssakis et al. [223]

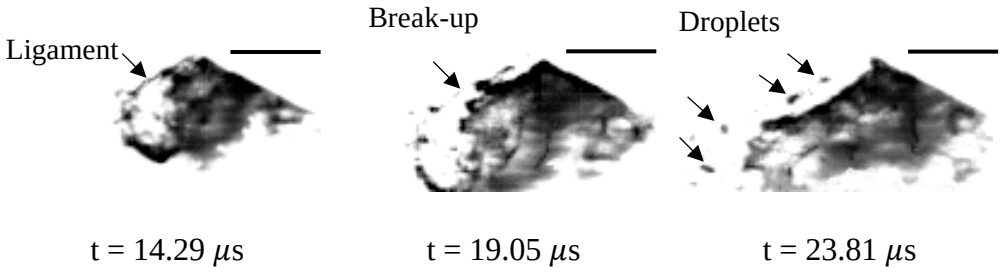

Figure 42. High-speed images (420,000 fps): visualizing the ligament breakup and droplet formation in CO_2-A: P_{inj}= 7.5 MPa, T_{inj}=19 °C and GLR= 0.2. The scale bar (100 $\boldsymbol{\mu}$m) is identical for all images.

To generate the secondary breakup map based on the aforementioned breakup regimes, the diameter of the ligaments is used as the characteristic length obtained from the high-speed images. **Figure 42** depicts the breakup of a ligament into multiple primary droplets resulted from CO_2-A at 7.5 MPa and 19 ºC. By inspecting this figure, we realized that the size of the primary droplets (~8.9 μm) is very close to the diameter of the ligament (~10.1 μm) before the breakup. Since such primary droplets may not be as visible as in **Figure 42** for other cases, we approximated the primary droplet sizes with the ligament diameter. Finally, to calculate the liquid velocity, we

manually tracked the ligaments identified in the high-speed images in the consecutive frames and measured the distance the ligament tips traveled over each time interval.

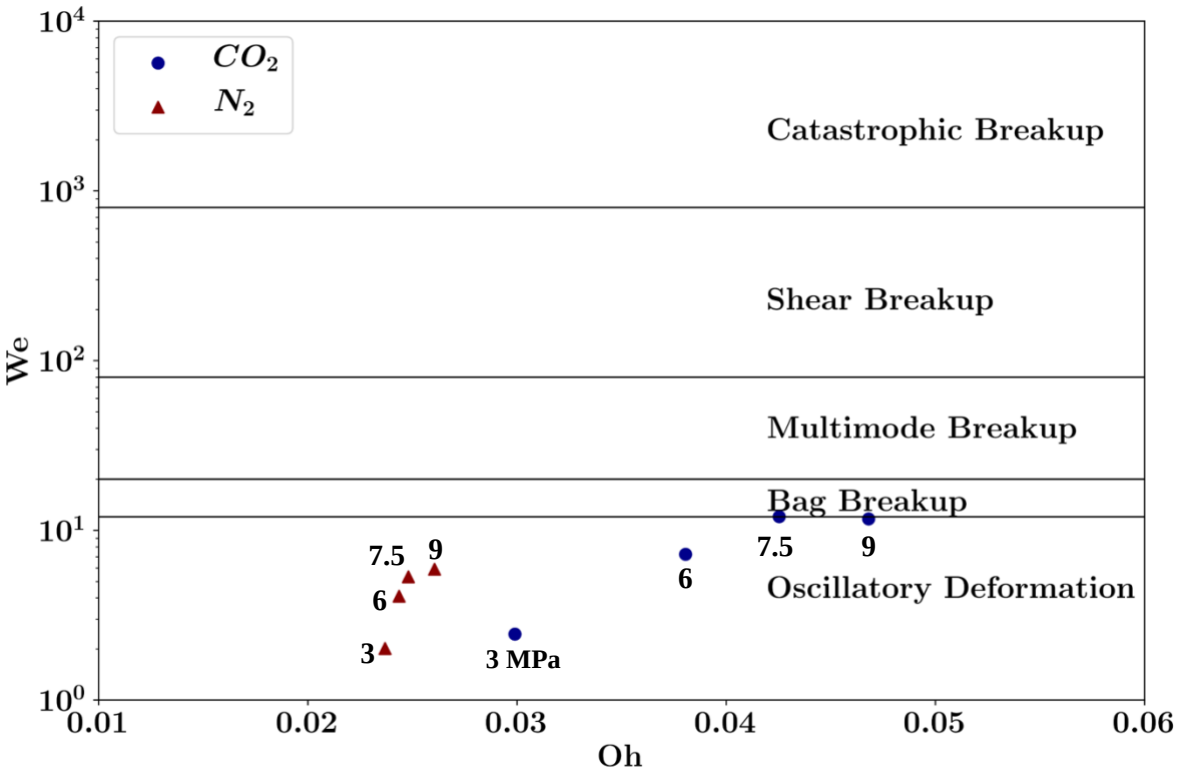

Figure 43. Map of the secondary breakup regime as a function of *We* and *Oh*. The experimental measurements represent injection pressures of P_{inj}= 3, 6, 7.5, and 9 MPa, T_{inj}= 25 ºC, GLR= 0.2 for CO_2-A and N_2-A.

Figure 43 illustrates the map of the secondary breakup regime as a function of *We* and *Oh* numbers for our experimental measurements that fall under Oh < 0.06 implying that the inertia forces are dominant to viscous forces. [152] According to this segmentation, the breakup of liquid droplets for N_2-A (at all injection pressures) and CO_2-A (at subcritical pressures) undergo the oscillatory vibration that might create secondary droplets the same size as the primary droplet they originated from. Especially for low *Oh* flows as in this study, drop distortion and vibration is the

key destabilization mechanism of the primary droplets. *We* increases at higher injection pressures as (1) it increases the relative velocity between the liquid and gas and (2) the dissolution of CO_2 in water leads to surface tension reduction with an increase in pressure. Thus, the highest *We* is achieved for the CO_2-A at 7.5 and 9 MPa injection pressure, which also results in the smallest SMDs as expected. At critical and supercritical pressures (i.e., 7.5 and 9 MPa, respectively), the droplet breakup regime shifts toward the bag breakup regime. It is noted that the secondary breakup map has been structured based on the experimental observation of droplet breakup exposed to a stream of high-speed surrounding gas or a high-pressure. On the other hand, comparing the size of the ligaments before breakup at 7.5 and 9 MPa obtained from the high-speed images (**Table 2**) with SMD at 10 cm with respect to the nozzle depicts about 80% reduction in the size of the liquid fragmentations at GLR equal to 0.2. At lower pressures where the breakup map suggests oscillatory deformation, the droplet size reduction is about 50%. Therefore, these observations suggest that a subsequent breakup is involved that causes the SMD to be much smaller than expected from the oscillatory and bag breakup regimes. Thus, the drag force imposed by the ambient air is not entirely responsible for initiating the breakup and the critical *We* is not suitable for describing the droplet breakup in gas-assisted atomization. A similar conclusion was earlier drawn for the analysis of the effervescent atomization. [196] Since the main mechanism behind the droplet breakup in this study is due to the degassing and burst of the bubbles of the dissolved gas, the subsequent droplet breakup is linked to relatively large local and spontaneous forces exerted from the expanding bubble that breaks up the parent droplets into much smaller droplets at a very short timescale. Measurements of droplet velocities and morphology of the child droplets

are further needed to better understand the subsequent breakup mechanism of the primary droplets in gas-assisted atomization systems that is beyond this work.

3.4 Deposition of Particle-Laden Droplets Created by SAA

3.4.1 CNC carrier droplet characterization

Fundamental understanding of the effect of different spray parameters and physical properties of the injection mixture on the size of carrier droplets that is especially crucial for designing the nanoparticle delivery system that was fully discussed in previous section led to design of experiments for this part. Here the fine and homogenous droplets that are created by the SAA system are used to inject and deposit CNC-laden droplets on a solid substrate that further evaporate and leave nanostructures with different morphologies that will be investigated.

The laser diffraction system is used for real-time measurementof SMD at 10, 15, and 20 cm axially located downstream of the nozzle. These points are selectedto fully represent the whole spray plume. **Figure 44** plots the measured SMD as a function of GLRfor different injection pressures and axial locations. It is observed in **Figure 44 (a-c**) that for each injection pressure, the mean droplet size decreases as GLR increases and the rate of SMD reductiondecreases with an increase in GLR and reaches a plateau at the GLR of 0.2. At this point, increasingGLR does not have a noticeable effect on the SMD and hence this value (i.e., GLR= 0.2) is selectedfor spray deposition experiments.

At each GLR and axial distance, increasing the injection pressure results in the formation of droplets with smaller sizes. This is owed to the higher solubility of CO_2 in water and lower interfacial tension of CO_2-water mixture at higher pressures as was indicated in **Table. 3**. The

combined effects enhance the primary breakup of the liquid jet due to the burst of dissolved gas bubbles and surface capillary breakup. As a result, the variation of droplet sizes by changing injection pressure is more evident in cases where measurement is performed closer to the nozzle (i.e., 10 cm axial distance in **Figure 44a**) compared to measurements further away from the injectionorifice (i.e., 15 and 20 cm from the orifice in **Figure 44b,** and **44c**). It is also evident that for each injectionpressure, increasing the axial distance between the injection orifice and SMD probe from 10 cm in **Figure 44a** to 20 cm in **Figure 44c**, results in smaller mean droplet sizes and their size does not vary significantly with GLR. This can be attributed to the "secondary breakup" of droplets that occursat locations further away from the nozzle. The secondary breakup is referred to a process in whichthe droplets exposed to high shear forces breakup into multiple smaller droplets.

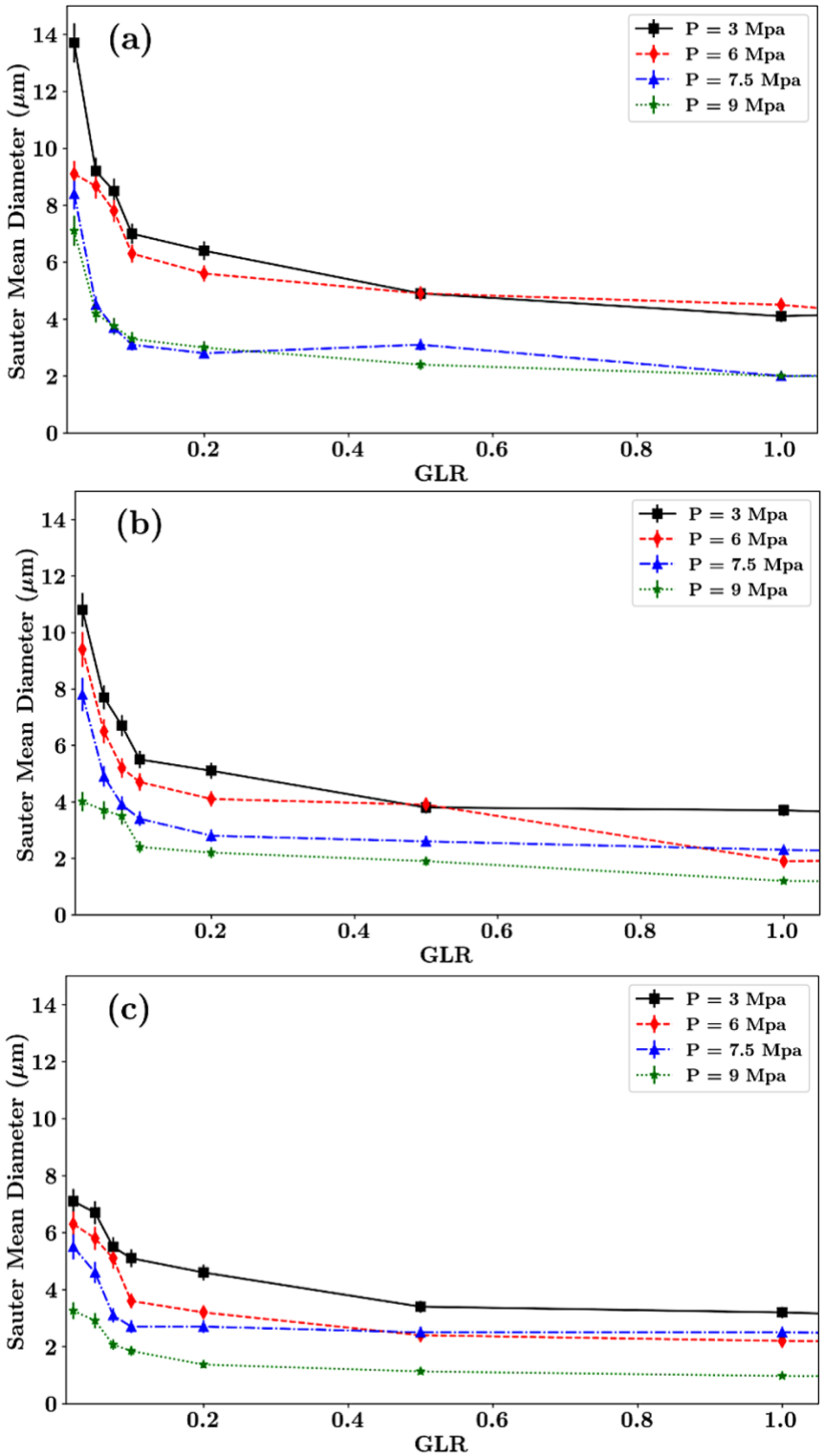

Figure 44. SMD measurements as a function of GLR for different injection pressures and an axial distanceof (a) 10 cm, (b) 15 cm, and (c) 20 cm from injection orifice.

Figure 45a shows the measured SMD as a function of injection pressure at 1 cm axial distancewith respect to the nozzle and for three different concentrations of CNC in the suspension (i.e., 0.2, 0.5, and 2wt%). Similar to **Figure 44**, increasing the injection pressure reduces the droplet sizes. The droplet sizes breakup into smaller droplets at locations further away from the orifice due to the secondary breakup. The sharpest decrease in the droplet is achieved at 7.5 MPa injection pressure that is close to the critical pressure of the CO_2-water mixture. The proximity to the criticalpressure enhances the diffusivity of CO_2 in water and the creation of more bubbles inside water upon injection that enhances the atomization process and reduces the droplet size. Further increasing the injection pressure to 9 MPa has a negligible effect on the droplet size. This can be attributed to the maximum diffusion coefficient of CO_2 in water that occurs at 7.5 MPa, [224] whichin turn results in minimum surface tension value for the water-CO_2 mixture at this pressure. [225] Inaddition, increasing the concentration of nanoparticles in the injection mixture, from 0.2wt% to 2wt%, increases the overall size of the carrier droplets. The viscosity of the aqueous suspension increases from 1.2 to 4 mPa.s by increasing the concentration from 0.2 to 2wt%. This enhancement (~three-fold) in viscosity of the injection mixture leads to an average of ~54% growth in droplet sizes of the spray. It is well established that an increase in liquid viscosityresults in the formation of larger droplets as it suppresses the breakup process by dampening the interfacial perturbations between the liquid and gas upon injection that eventually break it up to multiple droplets. [226, 227] The direct effect of droplet sizes on the dynamics of solvent evaporationwhich in turn influences the assembly of nanoparticles and architecture of nanostructures formedon the substrate is discussed in the next section.

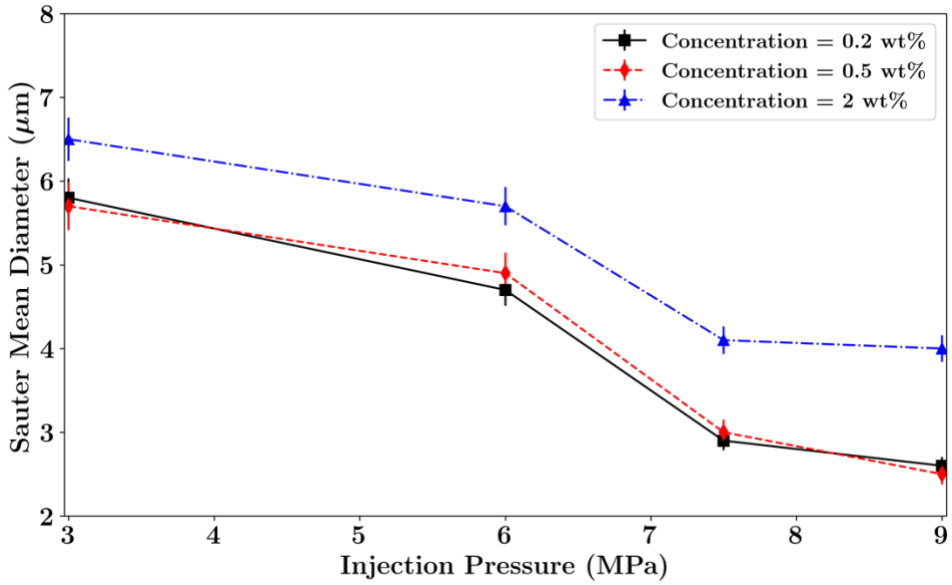

Figure 45. SMD as a function of pressure for different CNC concentrations measured at an axial distance of 15cm and GLR=0.2.

3.4.2 Nanostructure patterns

In this section, we discuss the CNC patterns that form after the evaporation of the liquid droplets generated through atomization of the aqueous CNC suspension. We study the effects of different process parameters on the created nanostructure on a glass substrate. **Figure 46** visualizes the polarized micrographs of otherwise transparent CNC nanostructures that are formed on the substrate upon droplet evaporation for different injection pressures. The glass substrates are 1cm by 1cm. **Figure 46** illustrates the architecture of nanostructures for various injection pressures for 0.2wt% (left column) and 2wt% (right column) CNC concentration. The main pattern of assembled nanostructures in these top-view micrographs can be categorized in one of the three shapes: (1) ring-shape, where the majority of nanoparticles accumulate along the edge of the evaporating droplet, (2) homogenous distribution, where particles scatter across the surface area of the evaporating droplet, and (3) transition stage, where there is still a distinct ring-shape structure and

some particles are also scattered within the center of the evaporating droplet. It is illustrated in **Figure 46a1-d1** that regardless of the injection pressure, the droplets with diameters smaller than ~5.5 μmexhibit a homogenous distribution, while droplets larger than ~7.5 μm have generated a ring- shaped structure, and droplets with diameter sizes in between the two thresholds (i.e., between 5.5to 7.5 μm) represent a transition between the two identified regimes. All three patterns were observed for all injection pressures as the droplet size distribution envelopes the detected thresholds. In **Figure 46a2-d2** that illustrate droplets with a higher concentration of CNC particles (i.e., 2wt%), the homogenous distribution, transition, and ring structure occurs for < 9.5 μm, ~9.5-11.5 μm, and > 11.5 μm droplet sizes, respectively. It is noted that at least 6 images were taken at different locations of the same substrate; all of which were in great agreement with the threshold detected in these figures.

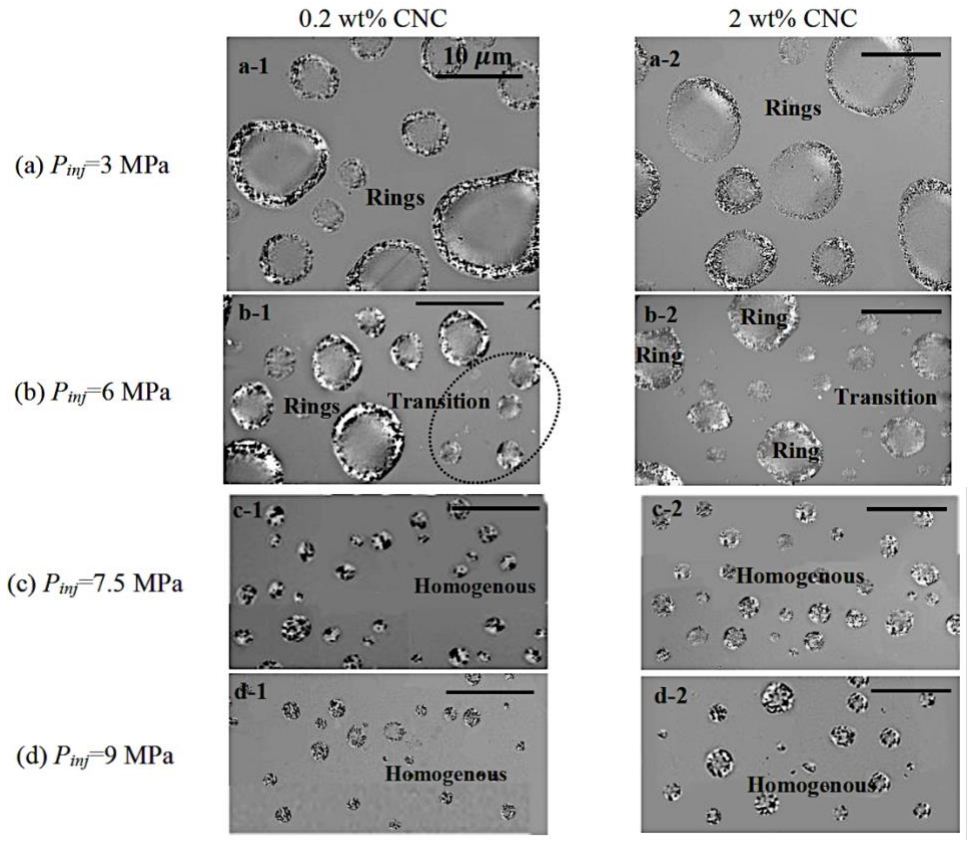

Figure 46. Polarized microscopy of CNC patterns after evaporation of water in CNC aqueous suspension droplets on a glass substrate located at 15cm axial distance for 0.2 wt% CNC concentration for (a-1) 3 MPa, (b-1) 6 MPa, (c-1) 7.5 MPa, and (d-1) 9 MPa injection pressures and 2 wt% CNC concentration for (a-2) 3 MPa, (b-2) 6 MPa, (c-2) 7.5 MPa, and (d-2) 9 MPa injection pressures. The 10 μm scale bar is identical in all images.

Figure 47 demonstrates the profile/height measurements of assembled nanostructures upon evaporation for droplet sizes varying from 5 to 13 μm and different concentrations (0.2wt%, 0.5wt%, 2wt%). Combined with top-view micrographs presented in **Figure 46**, they provide a 3D realization of the shape of assembled CNC nanostructures. In **Figure 47**, the droplets have been injected at 9 MPa. We discussed the effect of injection pressure on the nanoparticle patterns in **Figure 46** and showed that droplets with the same size and concentration shared the same pattern regardless of the injection pressure. The profilometry height measurements indicate that

nanostructures represent a ring, disk, or dome shape. A ring pattern that is identified with two peaks on the heightprofile is referred to the accumulation of nanoparticles along the edge of the droplet (labeled as “ring” in the top view in **Figure 46**). A dome forms when nanoparticles are captured at the interface during evaporation and mainly remained in the center after droplet evaporation i.e., only one peakis observed on the height profile. The dome structure was identified as “transition” in the top viewdepicted in **Figure 46**. Finally, a disk pattern forms when the height profile is nearly flat at the center. This indicates nanoparticles are scattered more uniformly across the surface area of the droplet compared to the dome and ring and. The disk pattern was identified as “homogenous” in the top view **Figure 46**. **Figure 47** shows that by decreasing the droplet size from 13 µm (red) down to5 µm (blue), the assembly of particles transits from ring-shape to a dome-shape structure for all CNC concentrations. The 9µm droplet (green) represents the transition between ring to a disk- shape structure. By increasing the concentration of CNC, the transition from a ring structure to disk occurs at larger droplet sizes. As will be discussed in the next section, the droplet size and concentration directly affect the evaporation rate of the solvent, which in turn influences the particle advection and diffusion and ultimately the nanoparticle patterns.

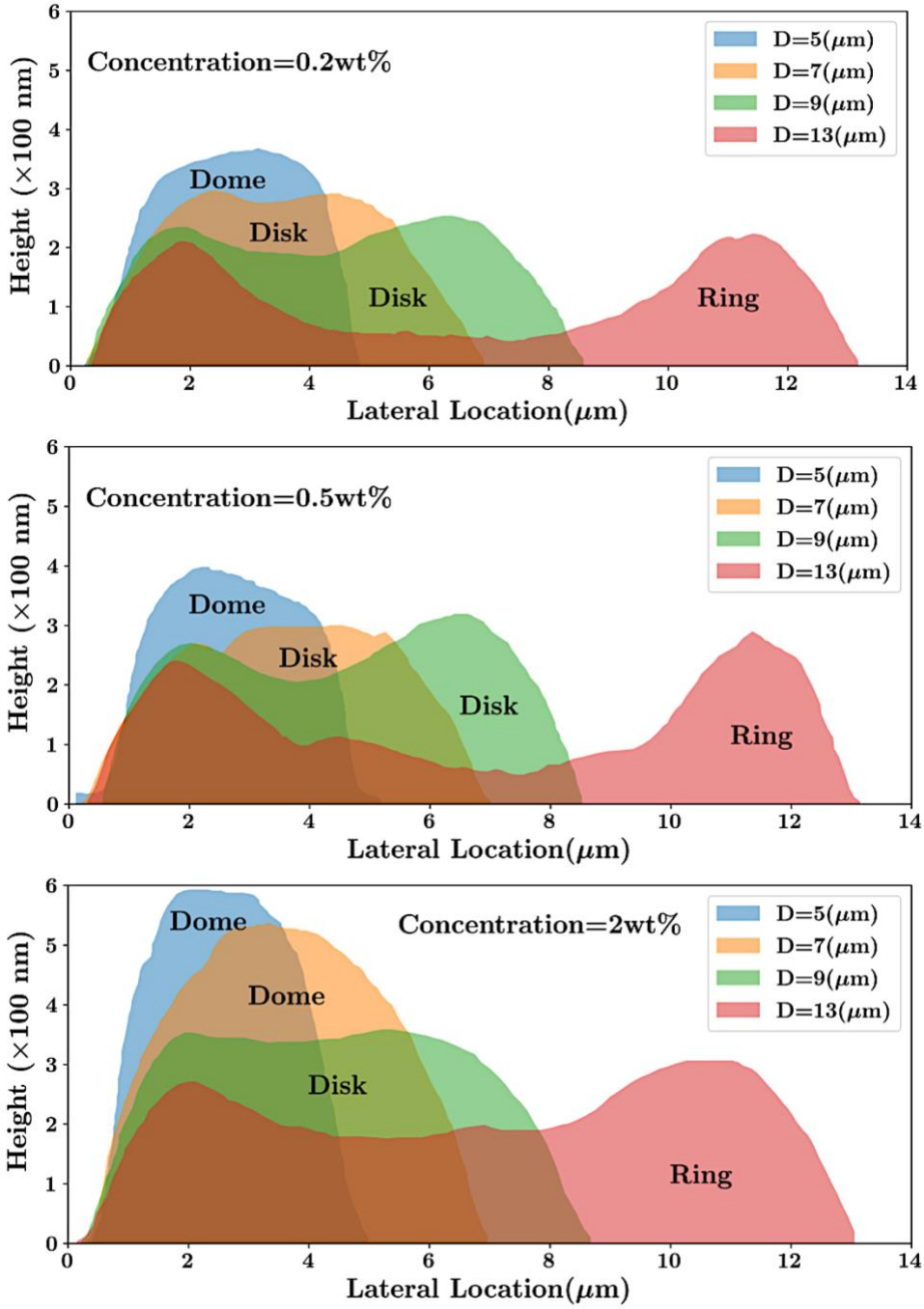

Figure 47. Profilometer height measurement of CNC nanostructures created on substrate after evaporationof water in droplets as a function of droplet diameter. CNC concentrations are 0.2, 0.5, and 2wt% and theinjection pressure is 9 MPa.

In summary, by controlling the droplet sizes we can engineer the desired pattern (ring, dome, disk) for different concentrations. The use of SCO_2 enables achieving a very uniform distribution of droplet sizes within the spray that facilitates achieving a uniform distribution of CNC with the desired pattern on the substrate. The injection pressure can directly control the overall size of droplets within the spray plum and can be adjusted to the size requirements of the specific application where the spray deposition system is being used. To quantitatively demonstrate the control over the nanostructure patterns with the injection pressure Dv90 measurement using laser diffraction method is plotted vs. injection pressure for variable concentrations plotted in **Figure 48**. Dv90 indicates the mean diameter size that represents 90% of the total volume of the existing liquid droplets **Figure 48** shows that at 7.5 MPa injection pressure and 0.2wt% CNC concentration, 90% of droplets are smaller than 4 μm in size. Based on the microscopic images and height profilometry, droplet sizes smaller than 4 μm will represent a homogenous nanoparticle distribution. As a result, most of the deposited nanostructures will exhibit a disk-shape structure. The information from this measurement combined with detailed discussions on the 3D architectureof fabricated micro/nanostructures have important implications in designing practical deposition systems to ensure that majority (> 90%) of droplets fall under a certain category (i.e., ring versus homogenous distribution).

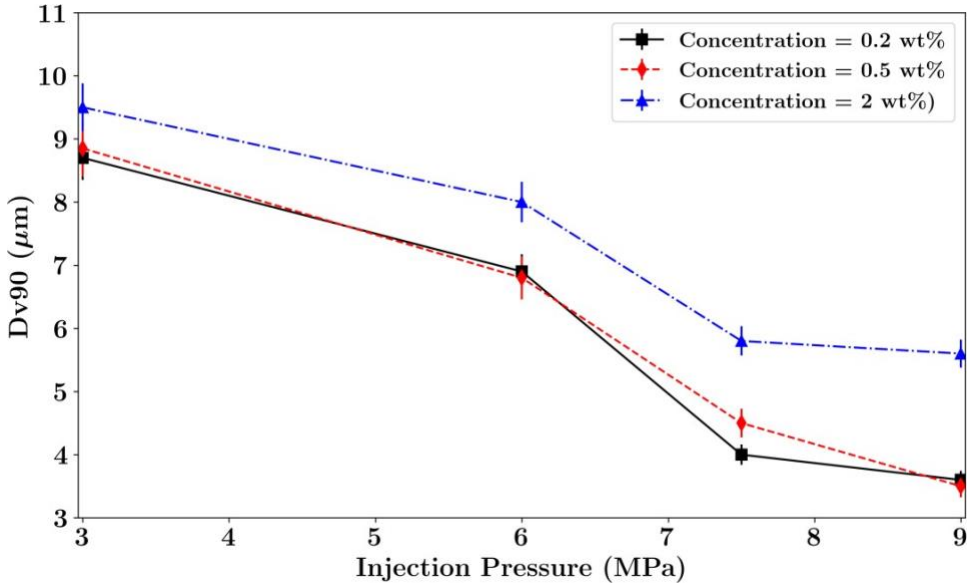

Figure 48. Dv90 as a function of injection pressure for different CNC concentrations measured at an axial distance of 15cm and GLR=0.2.

3.4.3 Evaporation-induced nanoparticle assembly

In this section, we will explore the CNC assembly in micron-size evaporating droplets. [228, 229] In order to find the link between the dynamics of droplet evaporation and the formation of a specific pattern upon evaporation, two main parameters are identified: (1) droplet evaporation ratethat is linked to the convective transport of CNC as the droplet edge recedes back during droplet evaporation; and (2) the Brownian diffusion rate of CNC in water. It has been shown that in the absence of other competing mechanisms e.g., external forces, special treatment of the substrate orsolvent, the competition between the convective and diffusive transport of particles dictates the final pattern after droplet evaporation. [230] The ratio of the convective to diffusive transport of particles during water evaporation is represented by the non-dimensional Péclet ($Pe= r^2/Dte$) number, where '*r' is* the droplet radius*, 'D'* is the particle mass diffusivity in the liquid phase and'*te'* is the droplet evaporation time. For millimeter-sized droplets, it has been shown

[231] that the ring pattern is typically favored for *Pe* >1 as the convective rate surpasses the diffusive rate. A reduction in the *Pe*, which implies a diffusion-dominated transport, is known to mitigate the ring formation toward a more uniform particle distribution. [232]

Our SMD measurements of the spray suggest that the droplet sizes are below 20 microns for which measuring the droplet evaporation rate is experimentally very challenging. As an alternative approach, there are various mathematical and analytical models to calculate the evaporation rate of a sessile droplet. [233-235] Larson's model (Equation 6), which is applicable for semispherical sessile droplets, is commonly used as one of the most accurate models that has been verified empirically. [233] This model is more accurate when the Bond number is smaller than 0.1 ($Bo = \frac{\rho g R h_0}{\sigma}$) and the Capillary number ($Ca = \frac{\mu u_r}{\sigma}$) is smaller than 1. *Bo* is the ratio of the gravitational to surface tension forces and accounts for the initial shape of the droplet whereas *Ca* is the ratio of viscous to capillaryforces and accounts for deformation of the droplet during evaporation. Here ρ, g, R, h_0, σ, μ, and u_r are the density, gravitational acceleration, contact line radius, initial droplet height, liquid-air surface tension, liquid viscosity, and average radial velocity due to evaporation, respectively. Wefirst compare the experimentally measured evaporation rate for a 1 μl droplet (~ 1 mm in radius) deposited on a glass substrate with the predictions of the Larson's model. The evaporation rate hasbeen measured with a timer at room condition (i.e., 25℃ temperature and ~40% relative humidity).Comparing the *Bo* (~0.07) and *Ca* (O(10^{-8})) for the largest droplet (i.e., 1mm radius) indicates thatthe droplet has a spherical cap shape and satisfies the requirement for using the Larson's model (Equation 6):

$$\dot{m}(t) = -\pi R D(1 - H) C_v(0.27\theta + 1.3) \quad (6)$$

Where R, D, H, C_v, and θ are the droplet radius (1mm), water vapor diffusivity (2.42E-05 m/s), relative humidity (40%), saturated water vapor concentration [236] (23.2 g/mm^3), and droplet contact angle (0.369 rad), respectively. The contact angle is measured on an image that is taken normal toa back-illuminated droplet deposited on a solid substrate. Larson's model predicts 709 seconds fora 1 mm droplet to evaporate and our experimental measurement indicated 718 seconds, which is in close agreement with the model prediction. The translational diffusion coefficient of CNC in DI-water measured by DLS for 0.2, 0.5, and 2wt% concentration is 7.18×10^{-12}, 6.7×10^{-12}, and 4.3×10^{-12} m^2/s, respectively. The diffusion coefficient reduces with concentration due to the packed space hindering the freedom of particles to transport. [237] We use this data along with the evaporation rate obtained from Larson's model and droplet sizes captured by the laser diffraction measurements to calculate *Pe*.

Figure 49 shows the calculated *Pe* as a function of droplet size for different CNC concentrations. By increasing the droplet size for each concentration, the evaporation time is also increased while the diffusion coefficient is constant for the same concentration. This results in higher *Pe* at higher concentrations. According to **Figure 49**, the corresponding *Pe* for a droplet size of13 μm is 1.27, 1.37, and 2.13, for 0.2, 0.5, and 2.0 wt% concentration, respectively. *Pe* >1 indicates the domination of the convective transport of CNC particles towards the edge of the droplet induced by the evaporation of DI-water and formation of a ring-shape structure as was depicted in **Figure 47**. Droplets within the 6-8 μm diameter range have an average *Pe* of 0.7, 0.8, and 1 for 0.2, 0.5, and 2.0 wt% concentration, respectively. These cases where convective and diffusion rates arealmost equal were identified as the transition between ring and dome shape structures in **Figure**

46. It is noted that Peclet does not provide a complete picture of the pattern engineering phenomenon and cannot describe the assembled patterns for droplets smaller than 3 μm. For instance, *Pe* for 0.2 and 0.5 wt% CNC in a 3 µm-droplet is almost similar (0.33, 0.34), however, the patterns are different. This can be either due to the fact that for small droplets where the ration of surface area to the volume is large, evaporation time does not follow the Larson's model and Peclet cannot be calculated accordingly. In addition, as evaporation advances in extremely small droplets (i.e., ~5 nm in diameter) the Knudsen number gets larger than 0.01, where continuum approximation does not stand, and regular Navier-Stokes equations cannot be applied. Knudsen number (Kn) is defined as the ratio of the mean free path line of moving particles to a physical length scale within the system (i.e., droplet radius). In these cases, molecular dynamic (MD) simulations, Lattice-Boltzmann, and statistical analyses are powerful tools to study the evaporation induced self-assembly of particles, and this has been one of the areas highlighted in future directions of this research.

It is noted that pure CNC is almost hydrophilic, and thus tends to form a ring. However, various observed patterns for different concentrations and different droplet sizes imply that in addition to the particle shape, level of hydrophilicity, the droplet size, and particle mass concentration also play a role in determining the final pattern. For instance, **Figure 47** showed that fora 9 µm-droplet, the pattern changed from a ring at 0.2 and 0.5wt% to a disk at 2wt%. Our results showed that increasing the ratio of mass concentration to droplet size tends to change the pattern from ring to dome as the particles are captured at the interface between the evaporating liquid and the surrounding air before they get a chance to accumulate at the droplet periphery and dry as a dome or disk after liquid evaporation.

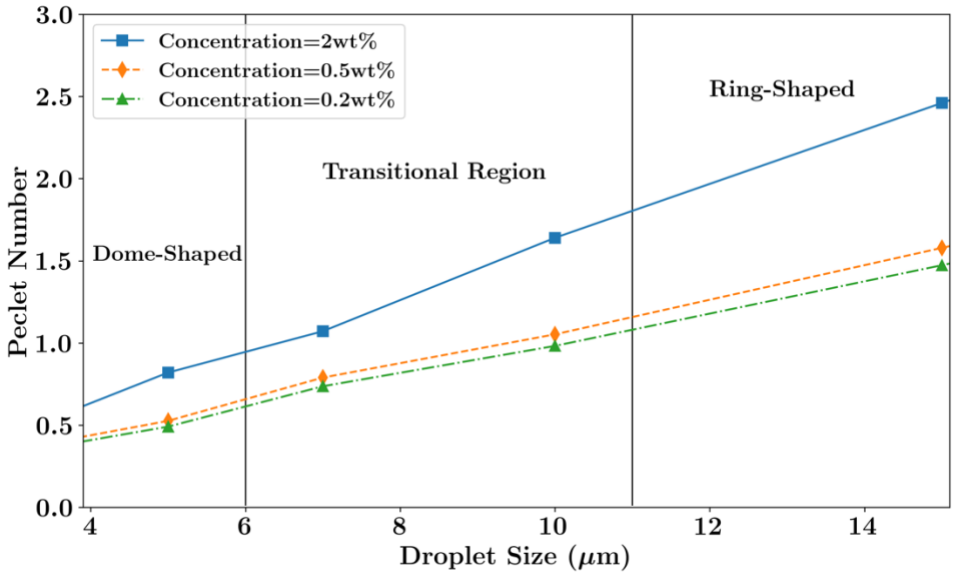

Figure 49. Peclet number as a function of droplet sizes for different CNC concentrations.

3.5 Evaporation Induced Self-Assembly of Hybrid Nanoparticle Systems

Achieving desired performance from self-assembly of nanoparticles (NPs) is very challenging due to the complex nature of interactions among the constituent building blocks. Understanding the self-assembly of nano-colloids through evaporation of particle-laden droplets to fabricate tailored functional and multi-material nanostructures is one of the major goals of this research. The particle-particle and particle-solvent interactions, as well as the hydrodynamic forces within an evaporative droplet (i.e., capillary and Marangoni flow) are the main driving factors that define the formation of the final nanostructure. In this section, a nanoparticle-agnostic approach that allows the fabrication of nanostructures with precisely engineered patterns is introduced. Evaporative droplets of aqueous suspensions of Carbon Nanotubes (CNTs), Graphene Nanoplatelets (GNPs) and Boron Nitride Nanotubes (BNNTs) represent NPs of different elemental

composition (i.e., carbonaceous and ceramic) with different sizes and shapes (i.e., nanotube, nanoplatelets) are investigated. CNCs are utilized as a platform to make hybrid nanoparticle systems (HNPS) of CNC and the secondary NP (i.e., CNC-CNT, CNC-GNP and CNC-BNNT). This section capitalizes on fundamental understanding of the repulsive-attractive interactions in this hybrid system and their effects on the final patterns that are created.

3.5.1 Hybrid nanoparticle system formation

The first step in formation of a hybrid system of CNC and CNT/GNP/BNNT nanoparticles is dispersion and stabilization of these NPs in DI-water as the solvent and understanding their 'weak' amphiphilic interactions. CNC has proved to be efficient in dispersing and stabilizing hydrophobic pristine CNTs, GNPs, and BNNTs in water without the need for functionalization or using a dispersant agent as shown in **Figure 50a**. CNCs poses abundant hydroxyl groups (-OH) that form hydrogen bonds with water molecules, and negatively charged sulfate half-ester groups, that make them a great agent to disperse the hydrophobic nanoparticles (GNP, CNT, and BNNT) in water. It is evident in this figure (**Figure 50a**) that in the absence of CNC, the hydrophobic CNT, GNP and BNNT settle in a few minutes after the sonication, while they remain stable and dispersed in water in the presence of CNC even after months from sonication. **Figures 5b** and **51c** show the efficacy of CNC in dispersing otherwise sedimented hydrophobic CNTs, GNPs and BNNTs in water by investigating the ξ-potential data and dynamic light scattering (DLS) measurements of HNPSs with different mass ratios in water. Higher electrical potential at the interface of the dispersed colloids and the solvent (i.e., higher zeta potential values) indicates higher hydrophilicity of HNPS and is desirable for stability of HNPS dispersion. However, it should be analyzed in conjunction with the DLS measurements, which is an indication of the size

of the colloid that is formed. Changing the ratio of CNC in the HNPS, alters the magnitude of the negative charge (ξ-potential value), suggesting it controls and tailors the degree of amphiphilicity of these hybrid systems in water. Increasing the ratio of CNC in all the HNPSs, increases the hydrophilicity of the system (**Figure 50b**), while decreasing this ratio results in formation of hydrophobic HNPSs. Maximum value of electrical potential for GNP-CNC, CNT-CNC and BNNT-CNC hybrids is achieved at 1:4 (61 mV), 1:1 (52 mV) and 1:20 (59 mV) ratios respectively, exhibiting higher electrical charge on their surface compared to CNC (51 mV) itself. These ratios also exhibit the smallest hydrodynamic diameters. The optimum dispersion in water is the result of increased hydrophilicity of hybrid colloids at a specific ratio with smallest hydrodynamic diameters. These measurements can quantify the degree of hydrophilicity of the HNPS and distinguish the CNC-NP ratio that best disperses in water. However, in order to find the other end of the spectrum and determine the degree of hydrophobicity, Z-potential test cannot be performed as HNPSs immediately sediment in water. As a result, in samples with lower ratios of CNC to NP, water contact angle (WCA) measurements are performed to show the relationship between NPs mass fraction and HNPS hydrophobicity by depositing a pure water droplet on a thin film of HNPS. Increasing the mass ratios of CNT, GNP, or BNNT to CNC's in the HNPS, increases WCA, indicating that hydrophobicity of HNPS increases (**Figure 50d**). The WCA measurement was performed on all various ratios of HNPS films, and the plot only shows the "hydrophilic-dominant" sample next to the "hydrophilic-hydrophobic-balanced" ones (i.e., CNT-CNC (5:1), GNP-CNC (12:1), BNNT-CNC (1:1)). These measurements show that regardless of the shape, size or type of the NPs, by changing the mass fraction of constituent NPs the amphiphilicity degree of HNPSs can be engineered.

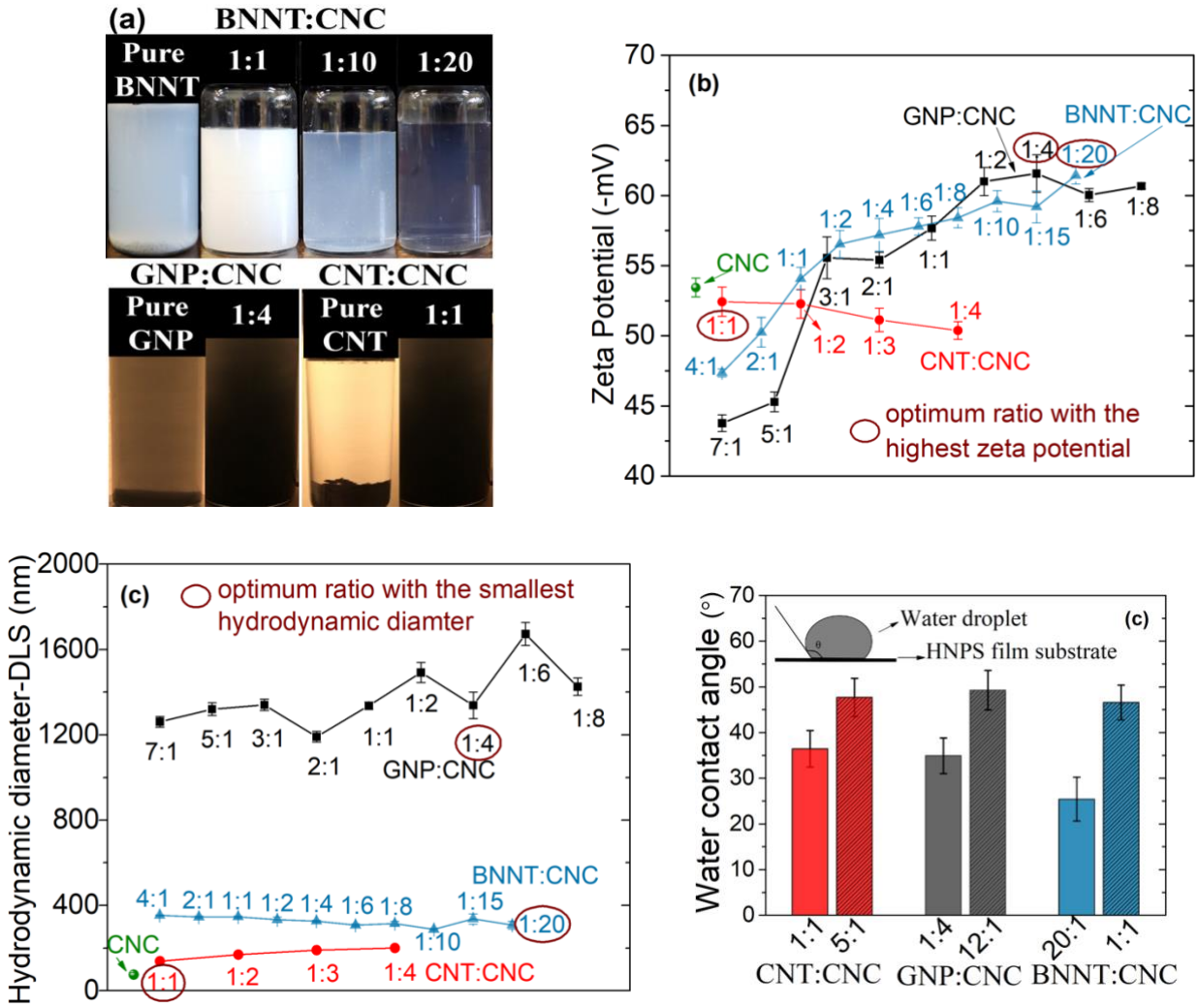

Figure 50. (a) Dispersion and stability of HNPSs with different ratios in DI-water, (b) zeta-potential, (c) hydrodynamic diameter, and (d) Water contact angle measurement on HNPS films with different ratios.

3.5.2 Morphology of nanostructures created through evaporation of droplets

After understanding the role of CNC in defining and engineering the amphiphilicity degree of aqueous colloidal suspensions of HNPS and recognizing the corresponding ratio of the two ends of amphiphilicity spectrum, the next step is to deposit droplets containing these NPs on a substrate and study the resultant self-assembly of system upon evaporation. It is worth noting that the

interaction of HNPS with substrate is another aspect affecting the final assembly. However, a neutral substrate (i.e., glass) has been used in all of the experiments to keep the wettability of the substrate constant and benchmark this effect. **Figure 51** shows microscopy images of the patterns created upon evaporation of droplets with hydrophilic (based on ξ-potential measurements) dominant and hydrophobic (based on contact angle measurements) dominant CNC to NPs ratios deposited on a glass substrate. Since CNCs are transparent crystals, polarized light is used in microscopy to better visualize them in the hybrids (white shiny features). In addition, SEM images and height profile measurements of the created nanostructures are presented to better visualize and quantify these structures.

Starting from the hydrophilic-dominant ratios (i.e., GNP-CNC 1:4, CNT-CNC 1:1, BNNT-CNC 1:20), a ring-shaped structure (CRE) is deposited along the edge of droplet as can be seen in **Figures 51a, 51i** and **51e**. Since the border of droplet pins to the substrate upon deposition, as evaporation advances across the surface, an outward capillary flow initiates to compensate for the mass loss along the contact line and drags the Nano-colloids toward the edges [238]. In a hydrophilic sample, these colloids are uniformly dispersed in water and possess a large surface energy, indicated by high electrical charge (according to ξ-potential measurement). Their strong attraction to water molecules along with their small hydrodynamic diameter (according to DLS measurement) facilitates their migration towards the edge of droplet by the capillary flow. The outward capillary flow that initiates upon evaporation of the solvent, pulls the CNC-bonded NPs towards the contact line, and accumulates them at the periphery. Taking a closer look within the ring (i.e., magnified images) better reveals the accumulation of previously dispersed HNPSs in this region after completion of evaporation.

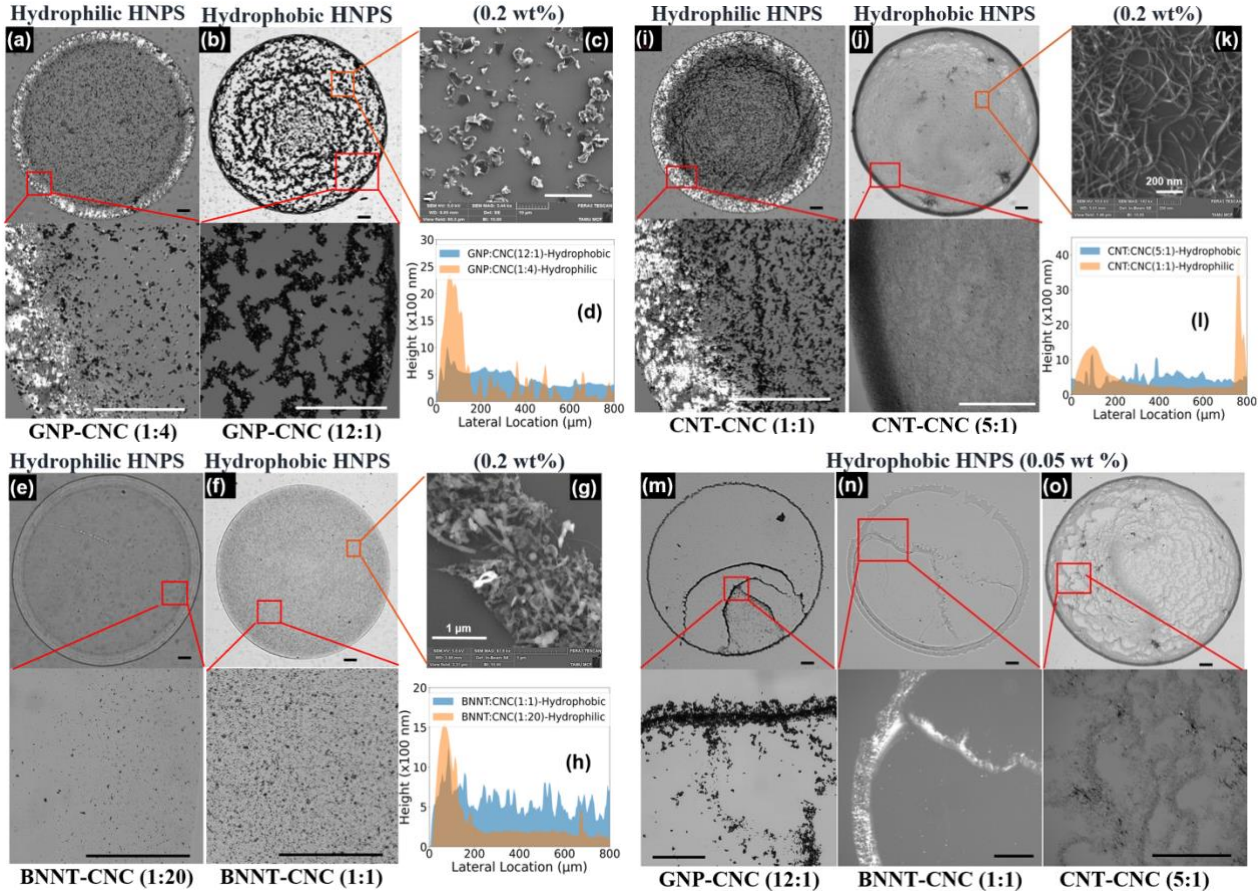

Figure 51. HNPS patterns vs. NPs' ratio and concentration. Effect of ratio of NPs to CNC labeled as (m:n) at 0.2 wt% concentration: GNP-CNC: (a) Hydrophilic-dominant HNPS, (b) hydrophobic-dominant HNPS, (c) SEM image of hydrophobic state, and (d) height distribution from edge to center of droplet (blue is hydrophobic- and orange is hydrophilic-dominant). (e)-(h) and (i)-(l) similar to (a)-(d) for BNNT-CNC and CNT-CNC, respectively. Effect of HNPS concertation: hydrophobic states of (m) GNP-CNC, (n) BNNT-CNT, and (o) CNT-CNC at 0.05 wt% concentration. Non-specified scale bar: 15 μm.

Decreasing the ratio of CNC in the HNPS and shifting the amphiphilicity of the system towards hydrophilic-hydrophobic-balanced state, reduces the electrical charge on the surface of the HNPSs (from ξ-potential data). At this point, the ring structure disappears and the loose-packed aggregates that are formed, create a disk-like structure (**Figures 51b**, **51j** and **51f**). The aggregated HNPSs oppose the outward capillary flow and mainly trap in the air-liquid interface of the droplet.

As evaporation proceeds, these HNPSs move with the interface and deposit across the surface area of the droplet, forming a disk structure. The pattern transition (from ring to disk) is best represented in the profilometry measurements in **Figures 51d**, **51l** and **51h**. In the hydrophilic-dominant ratios (orange-colored region), the maximum height is achieved at the edge as the NPs reside along the periphery of the droplet. Hydrophilic-hydrophobic-balanced ratios (blue-colored region) on the other hand show a uniform height distribution from edge to the center of the droplet. It is interesting to note that WCA of all HNPSs that formed a disk-shaped nanostructure is 47˚±2 independent of their type (**Figure 50d**). SEM micrographs of the same samples in **Figures 51c**, **51k** and **51g** visualize the morphology of HNPS and the structures they create. The monolayer distribution of hydrophobic-dominant CNT-CNC 5:1, GNP-CNC 12:1 and BNNT-CNC 1:1 samples is evident in these SEM figures, where the GNP-CNC, CNT-CNC and BNNT-CNC hybrids are laid on the substrate. Decreasing the concentration of nanoparticles in the aqueous suspension alters the final pattern, as there is not enough HNPS to cover the whole surface area of the droplet and a pining/depinning mechanism acts along the three-phase interface of the droplet. The inward lateral capillary flow drags the edge of the droplet inward, while the friction force opposes this movement. These two forces alternatively overcome each other and form the stranded structures illustrated in **Figures 51m**, **51n** and **51o** [112, 239]. Increasing the concentration (i.e., number of HNPS in the suspension) pins the periphery of droplet to the substrate and suppresses this effect. The observations in **Figure 51** indicate the crucial role of amphiphilicity degree and concentration of NPs in defining the final pattern that is formed on the substrate. In the next section we will discuss the effect of amphiphilicity on the intermolecular force balance that defines the architecture of the

assembled nanostructures regardless of the hydrodynamic forces induced by evaporation of the water.

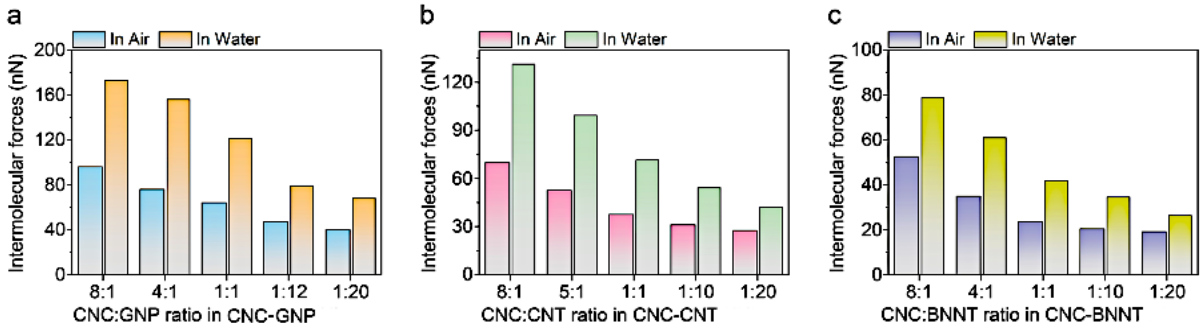

Figure 52. Intermolecular force measurement by AFM for HNPS of various mass ratios of (a) CNC-GNP, (b) CNC-CNT, and (c) CNC-BNNT, in air and in water.

3.5.3 Force balance investigation

To analyze and quantify the interactions among NPs and investigate the force balance in different HNPSs, AFM measurements are performed. **Figure 52** shows the intermolecular forces among HNPSs with different mass ratios (i.e., amphiphilicity degree) that are measured by coating the tip of AFM, both in air and water. The reported forces are the resultant force of all intermolecular adhesive and repulsive interactions (i.e., Van der Waals, electrostatic, hydrogen bond, capillary forces, and physical interactions, etc.) that the HNPS-coated tip of the AFM experiences in tapping (approaching and detaching) the HNPS film on the substrate. It is evident in **Figure 52** that increasing the ratio of CNC in the CNC-NP hybrid increases the intermolecular force in both mediums. Although the magnitude of forces is higher when the HNPSs are immersed in water, the trend of changing the force with the ratio of CNC in HNPS is similar for both air and water measurements. The molecules of CNC attach to CNT, GNP and BNNT through strong covalent bonds between hydroxyl groups on CNC and defected regions of the CNT, GNP and

BNNT [240], as well as polar-π interactions between CH in CNC and carbon rings in GNP and CNT, [241] and BN in BNNT. However, as we mentioned earlier, the strong covalent bonds do not participate in the self-assembly. The attractive force in hydrophilic-dominant GNP-CNC system (i.e., ring-shaped nanostructure) is 153.6nN in water and 76.5nN in air, while it decreases to 78.5nN and 48.4nN for hydrophilic-hydrophobic-balanced GNP-CNC (i.e., disk-shaped nanostructure) in water and air, respectively (**Figure 52a**). Hydrophilic-dominant and hydrophilic-hydrophobic-balanced CNC-CNT have an attractive intermolecular force of 99.3nN and 71.4nN in water, and 52.6nN and 37.6nN in air, respectively (**Figure 52b**). The intermolecular forces in hydrophilic-dominant and hydrophilic-hydrophobic-balanced CNC-BNNT system are ~42nN and 26.1nN n water and 23.6nN and ~19nN in air, respectively (**Figure 52c**), which are smaller than intermolecular forces in carbonaceous HNPSs due to less interaction of CNC molecules with BN ceramic NPs.

The higher force in hydrophilic HNPSs (i.e., higher ratio of CNC) that is measured with AFM is the result of an increase in attractive forces, from the competition between repulsive electrostatic forces and van der Waals, polar, or hydrogen bonds [242] all in form of attractive forces; and it is the amphiphilicity degree that determines the prevailing force. For example, in CNC-GNP 8:1 and 1:20 hybrids, the intermolecular forces in water are 85% and 76% higher than air due to the hydrogen bonds that HNPSs have with water (polar protic solvents with hydrogen atom connected to electronegative atom, e.g., O). The difference (85% vs 76%) is also due to higher amount of CNC molecules in the hydrophilic-dominant HNPS that increases the number of hydrogen bonds with water. AFM measurements presented in **Figure 52** prove that the intermolecular force balance and the corresponding 3D nanostructures that are fabricated is

governed by HNMS amphiphilicity degree, and hydrodynamic forces do not alter its overall trend. Force measurements also reveal that polar solvents form hydrogen bonds with HNPS. However, hydrogen bonds are directional forces [243] that are responsible to orient the HNPSs in the repulsive-attractive-directional force balance that engineers the final pattern of the self-assembly process. AFM results report the resultant intermolecular forces, but individual attractive, repulsive, and directional forces must be distinguished using molecular dynamic (MD) simulations which is beyond the scope of this research.

3.5.4 Functionality of multi-material nanostructures

CNC, GNP, CNT and BNNT have been extensively studied and proven as excellent choices as coating, reinforcement, or additive agents to improve mechanical, chemical, electrical, and thermal properties in various fields. [244-246] Hybrid nanoparticle systems are a new frontier in efficiently tailoring the properties and adding multi-functionalities. In order to highlight the importance of fundamental understanding of the self-assembly process of multi-material systems and the architecture of 3D nanostructures that they create on the functionality, the electrical conductivity of CNC-GNP and CNC-CNT with different amphiphilicity degrees (ring- and disk-shaped nanostructures) investigated. Droplets containing CNC-GNP and CNC-CNT, with amphiphilicity degrees according to **Figure 50**, were deposited to cover the glass substrate with either all rings or all disks upon completion of evaporation. The sheet electrical resistivity of the nanostructures was then measured as shown in **Figure 53**. Pure pristine CNT and GNP were fabricated as a film for comparison and data validation and exhibit the lowest sheet resistivity as was expected. Higher resistivity (lower conductivity) is recorded for hydrophilic-dominant CNC-

GNP (4-1) and CNC-CNT (1-1) that form a ring-shaped nanostructure in which conductive GNPs and CNTs only exist in the periphery. By shifting to more hydrophobic state and depositing disk-shaped nanostructure with CNC-GNP (1-12) and CNC-CNT (1-5) hybrids, the sheet resistivity decreases (conductivity of samples increases). This is due to the spread of the network of conductive NPs over the whole surface area of the droplet that enables movement of electrons. These results highlight the functionality of these multi-material coatings and capability of tailoring this functionality.

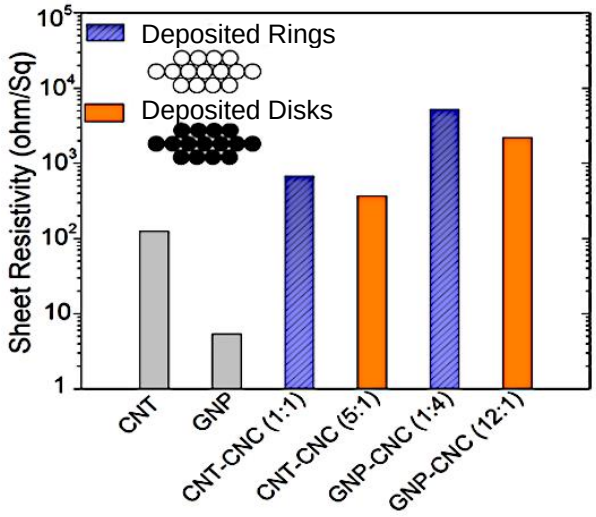

Figure 53. Sheet electrical resistivity of HNPSs with different amphiphilicity degrees.

3.5.5 Multi-material nanostructures deposited through SAA

Finally, in this section, nano-colloidal droplets containing GNP-CNC that are created by the SAA system are deposited on a glass substrate and the patterns of assembled nanostructures upon evaporation, as well as their functionality is characterized. **Figure 54** demonstrates the spray

deposited GNP-CNC nanostructures, using different concentration of the 12-1 GNP to CNC ratio to prevent formation of ring-shaped structures. A stencil mask [247, 248] was placed on the substrate prior to injection to get deposition only on desired places. The substrates were then used to investigate the functionality of deposited HNPS. **Figure 55** shows the corresponding polarized microscopic images of the deposited nanostructures. It is interesting that the assembled GNP-CNC structures that cover the whole area of a relatively large substrate (25mm by 76mm) are consistent with the patterns that were observed in a single GNP-CNC droplet in **Figure 51b**. This pattern is achieved by utilizing hydrophobic-dominant ratio of GNP-CNC system, and regardless of the deposition system (SAA or manual pipette deposition) similar morphology is observed in the evaporation induced assembly of NPs.

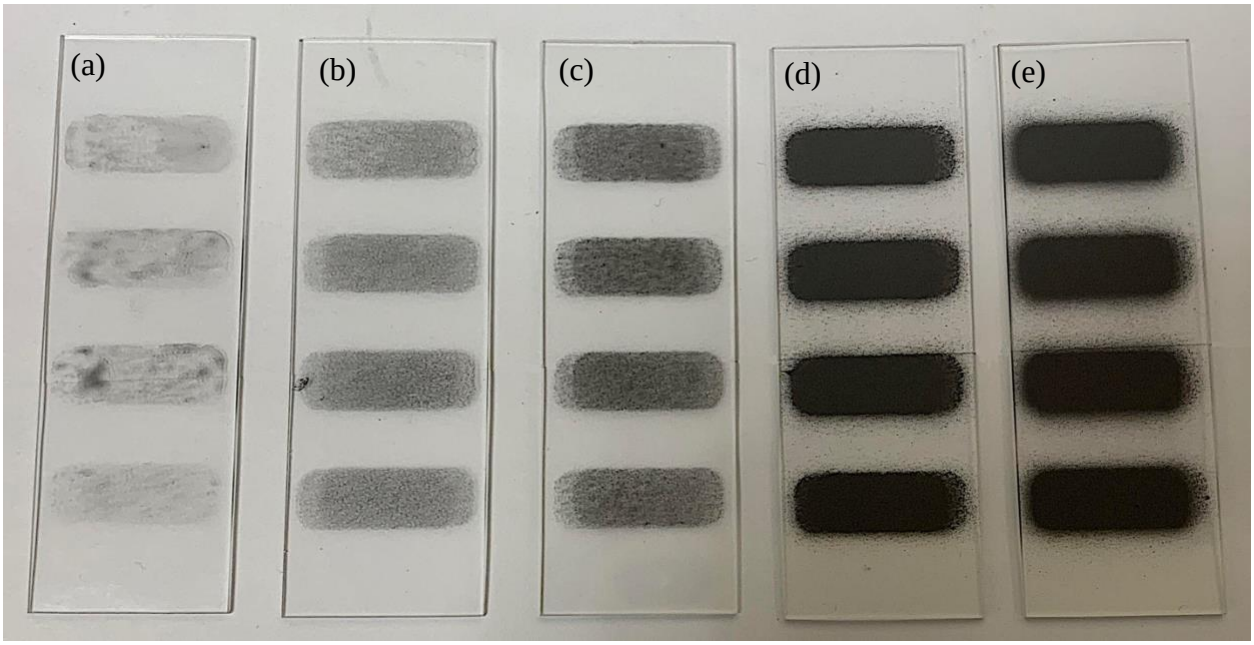

Figure 54. (a) 0.2wt%, (b) 1wt%, (c) 3wt%, (d) 10wt%, GNP-CNC deposited with 30 μm droplets, and (e) 10wt% GNP-CNC (12-1) deposited with 18 μm droplets. Droplets are created by SAA system. The 20scale bar is identical on all images.

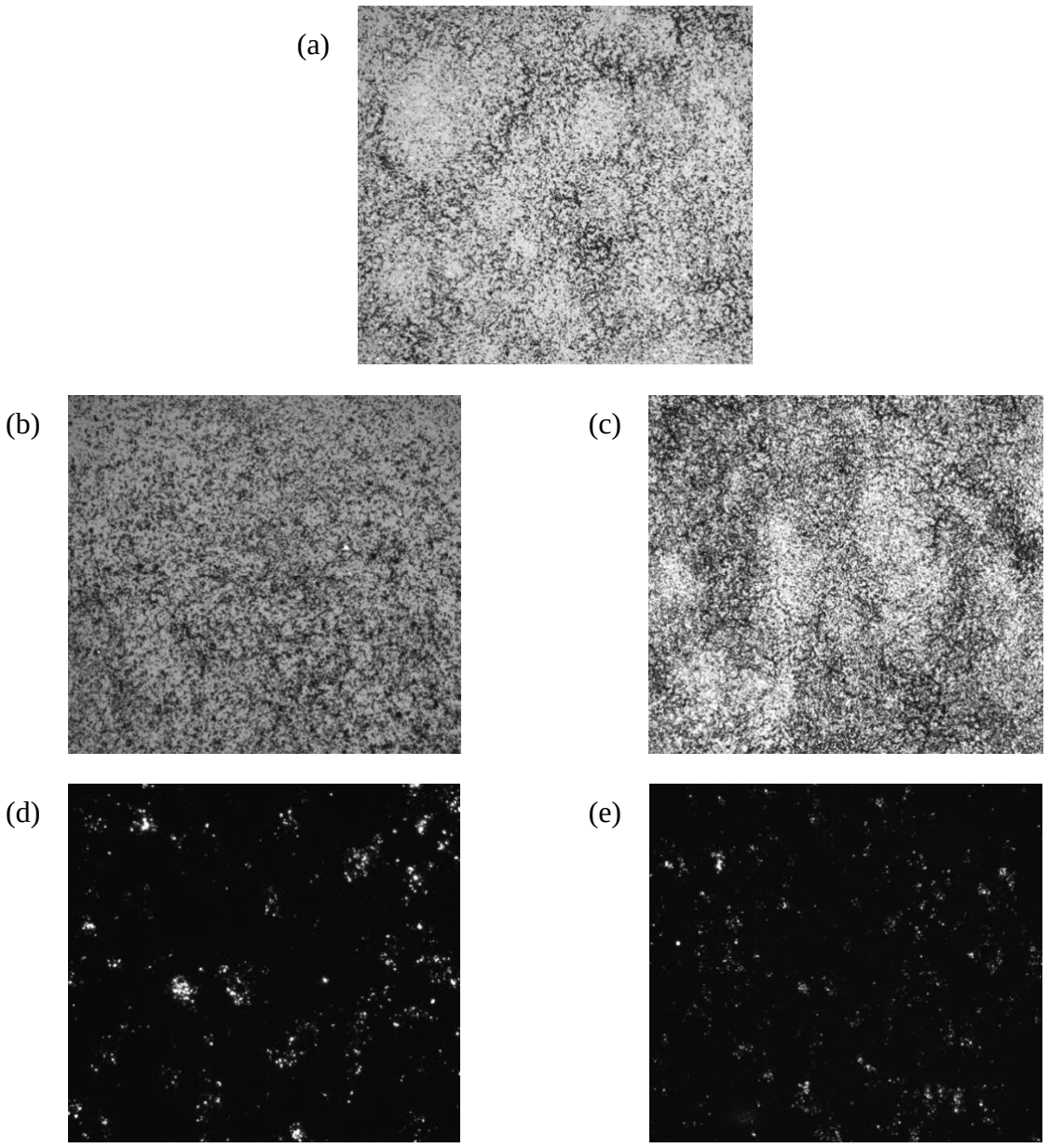

Figure 55. Polarized microscopic images of (a) 0.2wt%, (b) 1wt%, (c) 3wt%, (d) 10wt%, GNP-CNC (12-1) deposited with 30 μm droplets, and (e) 10wt% GNP-CNC (12-1) deposited with 18 μm droplets. The scale bar is identical on all images.

To better understand the 3D structure of the deposited HNPSs, profilometry measurements are performed, as illustrated in **Figure 56**. By increasing the concentration of HNPS in the injected

mixture, the thickness of the deposited structures increases from ~1.5μm in 0.2wt% to ~5μm in 10wt% sample. In addition, the 10wt% HNPS that has been delivered with smaller droplets (18 μm compared to 30 μm) shows a smoother deposition indicating the efficacy of engineering process parameters (i.e., spray settings and material composition) in tailoring the surface properties (i.e., surface roughness).

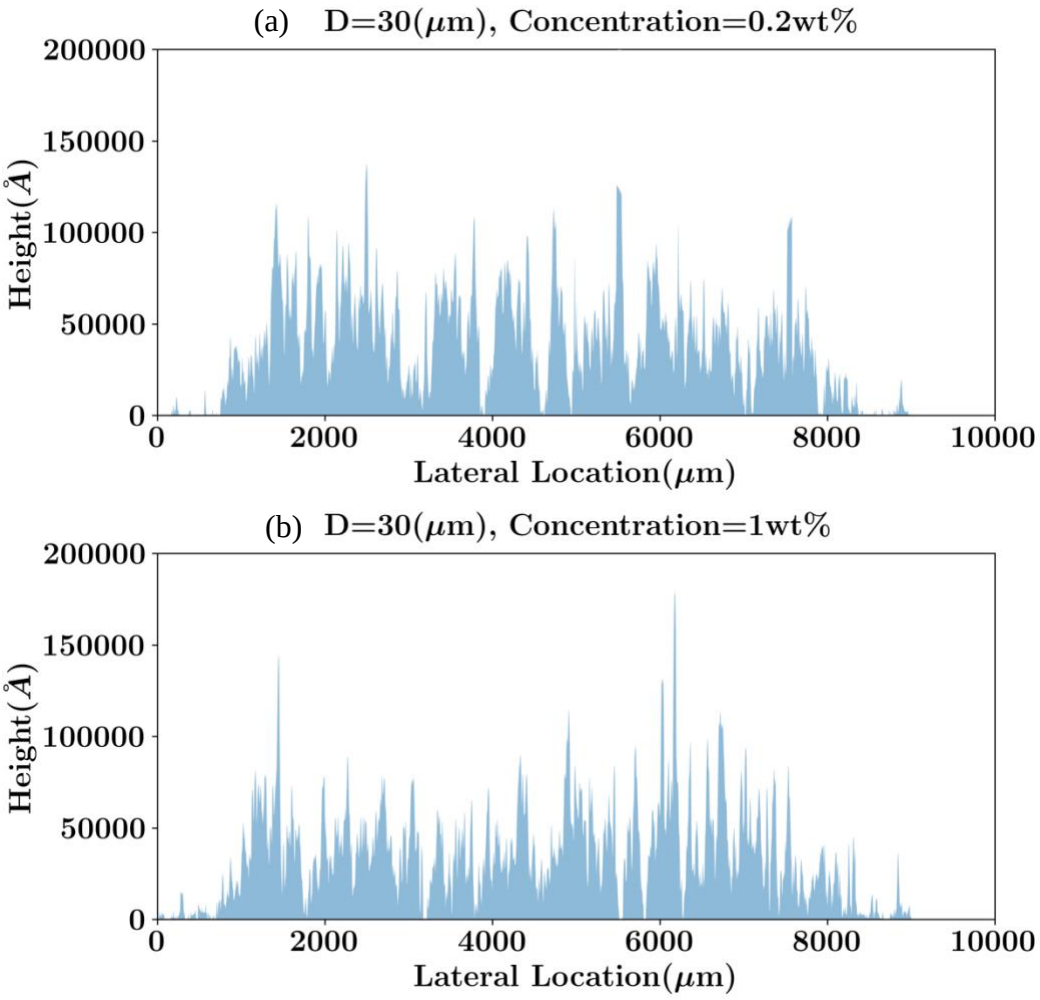

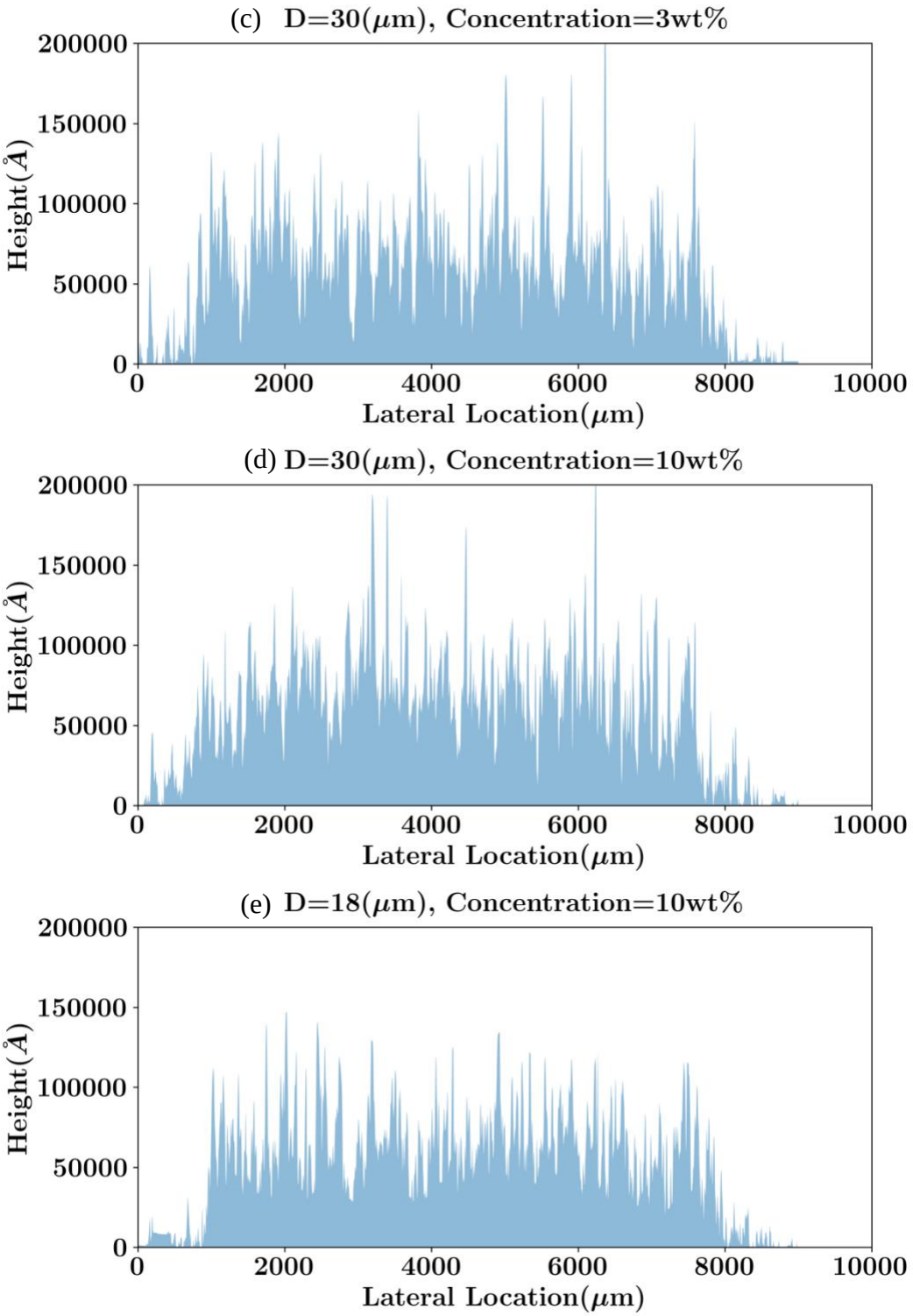

Figure 56. Profilometry of (a) 0.2wt%, (b) 1wt%, (c) 3wt%, (d) 10wt%, GNP-CNC deposited with 30 ***μ***m droplets, and (e) 10wt% GNP-CNC (12-1) deposited with 18 ***μ***m droplets.

As it has been discussed before (in Section 3.5.4), the multi-material systems that are deposited exhibit different functionalities (i.e., structural, electrical, thermal, etc.) depending on the NPs that form the HNPS. **Table 9** compares the sheet electrical resistivity of the samples in **Figure 54** measured with a four-point probe. Depositions with lower concentrations of HNPS (i.e., 0.2wt%, 1wt%, and 3wt%) did not allow the passage of electrical current, as there is not enough material on the substrate to make a continuous network of conductive GNPs. This can be remedied by increasing the injection duration to deposit more material. Both 10wt% samples allow the passage of the electrical current, and the sample created by smaller droplets shows lower resistivity compared to the one fabricated by larger droplets. This is due to the smoother surface and better connectivity of the GNP grid on the substrate. This again shows the highly tunability of the system in achieving desired outcome, from material selection to the functionality and degree of the functionality that can be reached. The novel multi-material deposition system is not only highly tailorable to the desired outcome, but it is very precise (i.e., nano-scale deposition resolution), simple, fast (i.e., millisecond time scales) and compatible with any material and substrate. Main takeaways, specific applications and future direction of this research are further discussed in the next section.

Table 9. Sheet electrical resistivity measurements

Sample	**Sheet Resistivity (Ohm/Sq)**
Pure GNP	5.38
10wt% GNP-CNC (12-1), deposited by 18 μm carrier droplets	970
10wt% GNP-CNC (12-1), deposited by 30 μm carrier droplets	1890

4. SUMMARY AND CONCLUSION

This research investigates engineering bottom-up fabrication of functional multi-material nanostructures through evaporation-induced self-assembly of nano-colloidal droplets created and deposited through supercritical assisted atomization system. For this purpose, feasibility of integration and efficacy of controlled deposition of droplets containing cellulosic nanoparticles (i.e., CNC) to improve the functionality and properties of 3D printed as well as composite parts was fully studied first, and below are the main conclusions from these studies:

- Real-time incorporation of CNC within polymer parts during 3D printing by spraying aqueous CNC suspensions through an atomization system working with pressurized air in an FDM printer was proved feasible.
- Assessing the thermomechanical properties and interlayer adhesion of CNC-ABS samples indicates that spraying the aqueous suspension of CNC with 0.5–1 wt% concentrations significantly improve the tensile strength and modulus by 33% and 20% in longitudinal and transverse printing direction, respectively and the interlayer shear strength by 44%.
- This improvement indicates the nano-stitching effect of CNC to improve the adhesion between adjacent layers and thus the ultimate strength. This proves that spraying the aqueous CNC suspensions during 3D printing is an efficient yet simple technique to effectively disperse and distribute CNC to improve the properties of 3D-printed polymers, and thus is a departure from status quo where nanomaterials are added to the filaments through costly processing methods.

- Utilizing cellulose nanocrystals in glass fiber coatings demonstrates improvement in interfacial interactions in epoxy composites. Improvements previously achieved at lab scale are matched or exceeded herein using two industrially scalable methods.
- Spray coating (SC) provided up to a 37% improvement in IFSS over uncoated fibers and up to an 18% improvement over fibers that were dip coated (DC) in equivalent coating formulations. Additionally, TGA revealed distinct decomposition peaks for SC fibers. This suggests more interactions between CNCs in SC fibers.

Second, the focus shifted towards fundamental understanding of the breakup mechanisms and droplet formation in supercritical CO_2 assisted atomization system as an efficient and fast way of creating fine and homogenous droplets that deliver the nanoparticles on targeted locations within the substrate. This section was extremely crucial to fine tune the parameters that define the deposition parameters and characteristics of the carrier droplets. Main findings from this section are summarized below:

- The primary breakup mechanism for CO_2-assisted atomization is governed by the formation, growth, and burst of the dissolved CO_2 in water that appears as a bulged liquid core close to the nozzle that squeezes the liquid into forming long ligaments and eventually shatters the liquid core.
- Near the critical pressure of CO_2-water mixture, the solubility of CO_2 is enhanced noticeably and increasing the temperature further lowers the surface tension where both effects promote atomization.

- The lowest SMD is captured at 7.5 MPa where CO_2 solubility reached a maximum. Operation at critical pressure leads to the finest and the most homogenous droplet size distribution that does not vary with temperature noticeably.
- The SMD for CO_2-A decreases with an increase in pressure and GLR. At pressures above the critical pressure, relative span factor (RSF) increases; and droplet sizes remain almost unchanged for GLRs above one. Therefore, applying excessive pressure above critical pressure and further increasing the gas mass flow rate do not lead to finer and a more homogenous droplet size distribution.
- For CO_2-water mixture injected at the critical pressure (7.5 MPa) and at subcritical temperatures (20ºC and 25ºC), increasing the temperature reduces the solubility and increases the droplet size while interfacial tension does not vary drastically. At supercritical temperatures (35ºC and 40ºC), increasing the temperature beyond the critical temperature enhances the atomization by lowering the surface tension while the solubility does not change drastically. The overall spray features include smaller liquid length, wider spray angle, and smaller SMD for CO_2-A for all test cases.

Comprehensive understanding of the underlying mechanisms in the SAA enabled deposition of CNC carrier droplets that were created using this system and investigating the evaporation induced self-assembly of CNCs and the nanostructures that they leave on a glass substrate. Below is a summary of main conclusions from this study:

- Microscopic visualization of the assembled nanoparticles on the substrates illustrates that morphology of nanostructures falls into three main categories: (1) ring-shape pattern, where the majority of nanoparticles accumulate along the edge of the evaporating droplet,

(2) homogenous distribution or disk pattern, where particles scatter more uniformly across the surface area of the evaporating droplet, and (3) transition stage, where there is still a distinct ring-shape structure yet some particles are scattered within the edges of the evaporating droplet.

- The profilometry height measurements combined with micrographs provide a 3D visualization of the assembled nanostructure and show that they either form a ring, disk, or dome-shaped architecture. Increasing the mass concentration to droplet size ratio shifts the morphology of assembled nanoparticles from ring to dome as the particles are trapped at the liquid-air interface before they get a chance to move towards the edge of the droplet.
- For each CNC concentration and regardless of the injection pressure, there is a droplet size threshold range above which the assembled nanostructures exhibit a ring pattern and below that they exhibit a homogenous distribution. For concentration of 0.2wt%, the lower and upper bounds of the threshold are 5.5 μm and 7.5 μm, respectively while for 2wt% CNC concentration these values increase to 9.5 μm and 11.5 μm, respectively.
- The injection pressure on the other hand dictates the size of the majority of droplets within the spray plume and can be used to design a system where the bulk of droplets fall under one of the identified nanostructure patterns.
- The size of the carrier droplets strictly influences the evaporation rate of solvent in particle-carrier droplets upon deposition on the substrate. The evaporation rate in turn, affects the prevalence of convective to diffusive transport of particles that is represented by Peclet number.

- The evaporation time is prolonged by increasing the droplet size for each concentration, which results in *Pe* >1 that indicates the higher rate of convective transport of particles to diffusive transport leading to accumulation of particles along the periphery of the droplet and formation of a ring-shaped structure. At *Pe* <1 where the diffusive movement of CNCs is dominant, a dome-shaped structure is formed for all tested concentrations. At *Pe* ~1, droplets fall in the transitional region where both ring and dome-shaped structures are observed.

Finally, cellulose nanocrystals are utilized as a platform to program the self-assembly process and tailor the formation of the final created structure. CNC-bonded nanoparticles form a hybrid system that regardless of the size, shape or elemental composition of the involved NPs can control the patterns that are left on the substrate. Main conclusions from this section are summarized below:

- SEM and polarized microscopic visualization and profilometry measurements showed that depending on the amphiphilicity degree of the HNPS, which is defined by the ratio of CNC to CNT, GNP or BNNT, as well as the concentration of these hybrids in the suspension, the final structure can take a form of a ring or dis-shaped structure.
- AFM measurements correlated the pattern of evaporation-induced self-assembly to the amphiphilicity degree by comparing the resultant intermolecular forces among molecules of CNC, water, and NPs. AFM was used to measures the resultant forces of all 'weak' interactions that a self-assembly system probe along. It was shown that the main intermolecular forces in patterning are van der Waals (attractive), electrostatic repulsion (repulsive) and hydrogen bonds (directional).

- Finally, sheet electrical resistivity of droplets containing HNPSs of different ratios deposited on a glass substrate demonstrated the efficacy of tailoring the pattern of nanostructure on the functionality of the deposited hybrid material. While hydrophilic-dominant disk-shaped CNC-CNT and CNC-GNP have higher sheet resistivity, moving toward more hydrophobic HNPS ratios shift the shape of nanostructure to a disk-shape structure where conductive NPs are better connected, and they can lower the electrical resistivity of the sample.

This research introduces a nanoparticle-agnostic approach for precisely controlling the bottom-up fabrication of nanostructure in evaporation-induced self-assembly systems. It also highlights the importance of engineering the self-assembly on the functionality of the final multi-material systems. The immediate application of engineering the morphology of evaporation induced self-assembly of nanoparticles that are created through supercritical assisted atomization of nano-colloidal droplets are: (i) graded functionality and (ii) uniform/homogenous coatings. Precise control over the concentration and ratio of materials within the hybrid nanomaterials systems and on-demand tailoring this balance enable us to deposit selective quantities and materials in specific locations and hence accommodates design for graded properties. The combination of materials that we can control and have studied provide structural, electrical, thermal, magnetic, optical, audio, etc. properties.

Further investigating the deposition, nanostructure formation, refining the system and properties of the final patterns that are formed, and their functionalities are among the areas that can be focused. Below is a list of potential areas that can be studied in future works:

- An immediate application of the nanostructure engineering process that has been developed in this work is the deposition of functional micro-patterns and coatings is specifically important in confined spaces such as wearable devices (e.g., Apple watch, Fitbit, …), where functionality is required in a limited space and packed structures. Consumable electronics market is moving toward smaller and thinner form factors, and more slick designs, which makes shifting away from conventional part manufacturing and use of nano/micro-structures inevitable. For example, fabrication and investigation of antennas that require to wrap around other structures are just one example where conductive lines with specific dimensional resolution and structures are deposited on flexible substrates in an interesting area of study. Our group has started working on this topic by depositing hybrid system of GNP-CNC on foldable substrates (both fabric and plastic) using the SAA system with a stencil mask to get the required geometrical design for antenna.
- Fabrication of conductive lines on unconventional substrates (e.g., rollable, foldable, stretchable, etc.) is another fast-growing and interesting area of work. Conductive lines on flexible substrates that stretch require more sophisticated design. Entangled CNTs create a conductive grid/network/line that stays intact and does not break even when the substrate is stretched (entangled CNTs act like a spring that conform to deformations of the substrate, instead of brittle conductive lines that disconnect the electrical current). The work in this area has also been started in our research group using the conductive HNPS and SAA system developed in this research, and electrical properties of deposited nanostructures are being characterized.

- Substrates made from nanocellulose are widely used in optically transparent screens and flexible devices. Depositing conductive lines (e.g., with CNT or GNP) with controlled patterns can be achieved using our methodology with the understanding that CNC which is the platform to tailor the amphiphilicity and hence distribution of secondary nanoparticle is available outside the droplet and on the substrate as well and material composition of the hybrid nanoparticle system needs to be adjusted accordingly.
- As this technology becomes more mature, new horizons in micro 3D printing might appear, where combinations of rings and disks on top of each other can create unique and complicated 3-dimensional structures.
- In general, controlled multi-material deposition and pattern engineering are each a powerful module in fabricating unique geometrical features with functional materials. Imagine depositing CNC-CNT rings on top of each other on a substrate to resemble micro-hollow-pillars that not only have electrical conductivity properties, but also act as a structural feature on the substrate for thermal management and cooling properties by providing micro-fluidic flow channels. Another example is deposition of disks with desired thicknesses that not only define the roughness and texture of the surface but also add functional material properties embedded in the deposited disks.

REFERENCES

1. C. Joachim, J.K. Gimzewski, Aviram,A.J. Nature. Electronics using hybrid-molecular and mono-molecular devices, Nature. 408 (2000) 541-548.
2. Y. Chen,A.J.E. Pepin. Nanofabrication: Conventional and nonconventional methods, Electrophoresis. 22 (2001) 187-207.
3. A. Mills, S.J.J.o.p. Le Hunte,p.A. Chemistry. An overview of semiconductor photocatalysis, 108 (1997) 1-35.
4. B.D. Gates, Q. Xu, M. Stewart, D. Ryan, C.G. Willson,G.M.J.C.r. Whitesides. New approaches to nanofabrication: molding, printing, and other techniques, Chemical reviews. 105 (2005) 1171-1196.
5. T. Betancourt,L.J.I.j.o.n. Brannon-Peppas. Micro-and nanofabrication methods in nanotechnological medical and pharmaceutical devices, International journal of nanomedicine. 1 (2006) 483.
6. S.E. Gratton, S.S. Williams, M.E. Napier, P.D. Pohlhaus, Z. Zhou, K.B. Wiles, B.W. Maynor, C. Shen, T. Olafsen,E.T.J.A.o.c.r. Samulski. The pursuit of a scalable nanofabrication platform for use in material and life science applications, Accounts of chemical research. 41 (2008) 1685-1695.
7. S. Qi,D. Craig. Recent developments in micro-and nanofabrication techniques for the preparation of amorphous pharmaceutical dosage forms, Advanced Drug Delivery Reviews. 100 (2016) 67-84.
8. C. Rockstuhl,F.J.A.P.L. Lederer. Photon management by metallic nanodiscs in thin film solar cells, 94 (2009) 213102.
9. L. Fan, C. Wang, M. Chen,B.J.J.o.P.S. Zhu. Recent development of ceria-based (nano) composite materials for low temperature ceramic fuel cells and electrolyte-free fuel cells, Journal of Power Sources. 234 (2013) 154-174.
10. G.Y. Tseng,J.C.J.S. Ellenbogen. Toward nanocomputers, 294 (2001) 1293-1294.
11. K. Luo, Z. Shi, J. Lai,A.J.A.P.L. Majumdar. Nanofabrication of sensors on cantilever probe tips for scanning multiprobe microscopy, 68 (1996) 325-327.
12. K. Luo, Z. Shi, J. Varesi, A.J.J.o.V.S. Majumdar, T.B. Microelectronics, M. Nanometer Structures Processing,Phenomena. Sensor nanofabrication, performance, and conduction mechanisms in scanning thermal microscopy, 15 (1997) 349-360.
13. F. Zabihi, M.J.J.o.C.T. Eslamian,Research. Substrate vibration-assisted spray coating (SVASC): significant improvement in nano-structure, uniformity, and conductivity of PEDOT: PSS thin films for organic solar cells, 12 (2015) 711-719.
14. Y.-Q. Wang, L. Gu, Y.-G. Guo, H. Li, X.-Q. He, S. Tsukimoto, Y. Ikuhara,L.-J.J.J.o.t.A.C.S. Wan. Rutile-TiO2 nanocoating for a high-rate Li4Ti5O12 anode of a lithium-ion battery, 134 (2012) 7874-7879.
15. H.T. Phan, N. Caney, P. Marty, S. Colasson,J. Gavillet. Surface wettability control by nanocoating: the effects on pool boiling heat transfer and nucleation mechanism, International Journal of Heat and Mass Transfer. 52 (2009) 5459-5471.

16. A. Biswas, I.S. Bayer, A.S. Biris, T. Wang, E. Dervishi, F.J.A.i.c. Faupel,i. science. Advances in top–down and bottom–up surface nanofabrication: Techniques, applications & future prospects, Advances in colloid interface science. 170 (2012) 2-27.
17. D. Mijatovic, J.C. Eijkel,A.J.L.o.a.C. van den Berg. Technologies for nanofluidic systems: top-down vs. bottom-up—a review, 5 (2005) 492-500.
18. Y. Xia,G.M.J.A.r.o.m.s. Whitesides. Soft lithography, 28 (1998) 153-184.
19. B.D. Gates, Q. Xu, J.C. Love, D.B. Wolfe,G.M.J.A.R.M.R. Whitesides. Unconventional nanofabrication, Annu. Rev. Mater. Res. 34 (2004) 339-372.
20. P. Dumon, W. Bogaerts, V. Wiaux, J. Wouters, S. Beckx, J. Van Campenhout, D. Taillaert, B. Luyssaert, P. Bienstman,D.J.I.P.T.L. Van Thourhout. Low-loss SOI photonic wires and ring resonators fabricated with deep UV lithography, IEEE Photonics Technology Letters. 16 (2004) 1328-1330.
21. A. Bertsch, H. Lorenz, P.J.S. Renaud,A.A. Physical. 3D microfabrication by combining microstereolithography and thick resist UV lithography, Sensors
Actuators A: Physical Science. 73 (1999) 14-23.
22. B.J.J.J.o.v.s. Lin,technology. Deep UV lithography, 12 (1975) 1317-1320.
23. F. Watt, A. Bettiol, J. Van Kan, E. Teo,M.J.I.J.o.N. Breese. Ion beam lithography and nanofabrication: a review, 4 (2005) 269-286.
24. J.J.J.o.V.S. Melngailis, T.B.M. Processing,Phenomena. Focused ion beam technology and applications, 5 (1987) 469-495.
25. M. Horák, K. Bukvišová, V. Švarc, J. Jaskowiec, V. Křápek,T.J.S.r. Šikola. Comparative study of plasmonic antennas fabricated by electron beam and focused ion beam lithography, Scientific reports. 8 (2018) 1-8.
26. M.J.B. Altissimo. E-beam lithography for micro-/nanofabrication, Biomicrofluidics. 4 (2010) 026503.
27. Y.J.M.E. Chen. Nanofabrication by electron beam lithography and its applications: A review, Microelectronic Engineering. 135 (2015) 57-72.
28. T. Ito,S.J.N. Okazaki. Pushing the limits of lithography, Nature. 406 (2000) 1027-1031.
29. E. Spille,R. Feder, X-ray lithography. X-ray Optics, Springer, 1977, pp. 35-92.
30. J. Foresi, P.R. Villeneuve, J. Ferrera, E. Thoen, G. Steinmeyer, S. Fan, J. Joannopoulos, L. Kimerling, H.I. Smith,E.J.n. Ippen. Photonic-bandgap microcavities in optical waveguides, Nature. 390 (1997) 143-145.
31. M. Marko, C. Hsieh, R. Schalek, J. Frank,C.J.N.m. Mannella. Focused-ion-beam thinning of frozen-hydrated biological specimens for cryo-electron microscopy, 4 (2007) 215-217.
32. L.A. Giannuzzi,F.A.J.M. Stevie. A review of focused ion beam milling techniques for TEM specimen preparation, Micron. 30 (1999) 197-204.
33. S.Y. Chou, C. Keimel,J.J.N. Gu. Ultrafast and direct imprint of nanostructures in silicon, Nature. 417 (2002) 835-837.
34. Q.H. Wang, Z. Jin, K.K. Kim, A.J. Hilmer, G.L. Paulus, C.-J. Shih, M.-H. Ham, J.D. Sanchez-Yamagishi, K. Watanabe,T.J.N.c. Taniguchi. Understanding and controlling the substrate effect on graphene electron-transfer chemistry via reactivity imprint lithography, 4 (2012) 724.

35. S.Y. Chou, P.R. Krauss, P.J.J.J.o.V.S. Renstrom, T.B. Microelectronics, M. Nanometer Structures Processing,Phenomena. Nanoimprint lithography, Journal of Vacuum Science. 14 (1996) 4129-4133.
36. L.J.J.A.m. Guo. Nanoimprint lithography: methods and material requirements, Advanced materials. 19 (2007) 495-513.
37. S.Y. Chou, P.R. Krauss, P.J.J.J.o.V.S. Renstrom, T.B. Microelectronics, M. Nanometer Structures Processing,Phenomena. Nanoimprint lithography, 14 (1996) 4129-4133.
38. D.S. Ginger, H. Zhang,C.A.J.A.C.I.E. Mirkin. The evolution of dip-pen nanolithography, Angewandte Chemie International Edition. 43 (2004) 30-45.
39. R.D. Piner, J. Zhu, F. Xu, S. Hong,C.A.J.s. Mirkin. " Dip-pen" nanolithography, 283 (1999) 661-663.
40. K. Salaita, Y. Wang,C.A.J.N.n. Mirkin. Applications of dip-pen nanolithography, 2 (2007) 145-155.
41. R. Garcia, A.W. Knoll,E.J.N.n. Riedo. Advanced scanning probe lithography, Nature nanotechnology. 9 (2014) 577.
42. G.-Y. Liu, S. Xu,Y.J.A.o.C.R. Qian. Nanofabrication of self-assembled monolayers using scanning probe lithography, 33 (2000) 457-466.
43. K. Ariga, J.P. Hill,Q.J.P.C.C.P. Ji. Layer-by-layer assembly as a versatile bottom-up nanofabrication technique for exploratory research and realistic application, Physical Chemistry. 9 (2007) 2319-2340.
44. S.M.J.C.r. George. Atomic layer deposition: an overview, Chemical reviews. 110 (2010) 111-131.
45. P.J. Cowdery-Corvan, D.H. Levy, S.F. Nelson, D.C. Freeman,T.D. Pawlik, *Process for atomic layer deposition*. 2012, Google Patents.
46. M. Ritala,M. Leskelä, Atomic layer deposition. Handbook of Thin Films, Elsevier, 2002, pp. 103-159.
47. A. Reina, X. Jia, J. Ho, D. Nezich, H. Son, V. Bulovic, M.S. Dresselhaus,J.J.N.l. Kong. Large area, few-layer graphene films on arbitrary substrates by chemical vapor deposition, 9 (2009) 30-35.
48. Y.H. Lee, X.Q. Zhang, W. Zhang, M.T. Chang, C.T. Lin, K.D. Chang, Y.C. Yu, J.T.W. Wang, C.S. Chang,L.J.J.A.m. Li. Synthesis of large-area MoS2 atomic layers with chemical vapor deposition, Advanced materials. 24 (2012) 2320-2325.
49. J.E. Mahan. Physical vapor deposition of thin films, (2000).
50. Y. Kong, D. Yu, B. Zhang, W. Fang,S.J.A.P.L. Feng. Ultraviolet-emitting ZnO nanowires synthesized by a physical vapor deposition approach, Applied Physics Letters. 78 (2001) 407-409.
51. L.L. Hench,J.K.J.C.r. West. The sol-gel process, Chemical reviews. 90 (1990) 33-72.
52. Y.-H. Kim, J.-S. Heo, T.-H. Kim, S. Park, M.-H. Yoon, J. Kim, M.S. Oh, G.-R. Yi, Y.-Y. Noh,S.K.J.N. Park. Flexible metal-oxide devices made by room-temperature photochemical activation of sol–gel films, 489 (2012) 128-132.
53. H.T. Maune, S.-p. Han, R.D. Barish, M. Bockrath, W.A. Goddard III, P.W. Rothemund,E.J.N.n. Winfree. Self-assembly of carbon nanotubes into two-dimensional geometries using DNA origami templates, 5 (2010) 61-66.

54. Y.Y. Pinto, J.D. Le, N.C. Seeman, K. Musier-Forsyth, T.A. Taton,R.A.J.N.L. Kiehl. Sequence-encoded self-assembly of multiple-nanocomponent arrays by 2D DNA scaffolding, 5 (2005) 2399-2402.
55. G.M. Whitesides,B.J.S. Grzybowski. Self-assembly at all scales, 295 (2002) 2418-2421.
56. Z. Nie, A. Petukhova,E.J.N.n. Kumacheva. Properties and emerging applications of self-assembled structures made from inorganic nanoparticles, 5 (2010) 15-25.
57. D. Philp,J.F.J.A.C.I.E.i.E. Stoddart. Self-assembly in natural and unnatural systems, 35 (1996) 1154-1196.
58. J. Cai, L. Zhang, S. Liu, Y. Liu, X. Xu, X. Chen, B. Chu, X. Guo, J. Xu,H.J.M. Cheng. Dynamic self-assembly induced rapid dissolution of cellulose at low temperatures, Macromolecules. 41 (2008) 9345-9351.
59. G.A. Ozin, K. Hou, B.V. Lotsch, L. Cademartiri, D.P. Puzzo, F. Scotognella, A. Ghadimi,J.J.M.T. Thomson. Nanofabrication by self-assembly, 12 (2009) 12-23.
60. S. Lindsay, Introduction to nanoscience. Oxford University Press, 2010.
61. H. Minemawari, T. Yamada, H. Matsui, J.y. Tsutsumi, S. Haas, R. Chiba, R. Kumai,T. Hasegawa. Inkjet printing of single-crystal films, Nature. 475 (2011) 364-367.
62. P. Calvert. Inkjet printing for materials and devices, Chemistry of materials. 13 (2001) 3299-3305.
63. R.D. Deegan, O. Bakajin, T.F. Dupont, G. Huber, S.R. Nagel,T.A. Witten. Capillary flow as the cause of ring stains from dried liquid drops, Nature. 389 (1997) 827.
64. P.J. Yunker, T. Still, M.A. Lohr,A.J.N. Yodh. Suppression of the coffee-ring effect by shape-dependent capillary interactions, 476 (2011) 308-311.
65. L. Bansal, P. Seth, B. Murugappan,S.J.A.P.L. Basu. Suppression of coffee ring:(Particle) size matters, Applied Physics Letters. 112 (2018) 211605.
66. M. Anyfantakis, Z. Geng, M. Morel, S. Rudiuk,D.J.L. Baigl. Modulation of the coffee-ring effect in particle/surfactant mixtures: the importance of particle–interface interactions, Langmuir. 31 (2015) 4113-4120.
67. A. Crivoi,F.J.L. Duan. Elimination of the coffee-ring effect by promoting particle adsorption and long-range interaction, Langmuir. 29 (2013) 12067-12074.
68. P.J. Yunker, T. Still, M.A. Lohr,A.G. Yodh. Suppression of the coffee-ring effect by shape-dependent capillary interactions, Nature. 476 (2011) 308-311. https://doi.org/10.1038/nature10344.
69. S. Huang, M.-L. Vignolles, X.D. Chen, Y. Le Loir, G. Jan, P. Schuck, R.J.T.i.f.s. Jeantet,technology. Spray drying of probiotics and other food-grade bacteria: A review, 63 (2017) 1-17.
70. A. Gharsallaoui, G. Roudaut, O. Chambin, A. Voilley,R.J.F.r.i. Saurel. Applications of spray-drying in microencapsulation of food ingredients: An overview, 40 (2007) 1107-1121.
71. C.G. Drosou, M.K. Krokida,C.G.J.D.t. Biliaderis. Encapsulation of bioactive compounds through electrospinning/electrospraying and spray drying: A comparative assessment of food-related applications, 35 (2017) 139-162.
72. A. Singh,G.J.A.d.d.r. Van den Mooter. Spray drying formulation of amorphous solid dispersions, 100 (2016) 27-50.

73. J. Broadhead, S. Edmond Rouan, C.J.D.d. Rhodes,i. pharmacy. The spray drying of pharmaceuticals, 18 (1992) 1169-1206.
74. V. Dugas, J. Broutin,E.J.L. Souteyrand. Droplet evaporation study applied to DNA chip manufacturing, 21 (2005) 9130-9136.
75. S. Shariatnia, A. Veldanda, S. Obeidat, D. Jarrahbashi,A.J.C.P.B.E. Asadi. Atomization of cellulose nanocrystals aqueous suspensions in fused deposition modeling: A scalable technique to improve the strength of 3D printed polymers, 177 (2019) 107291.
76. I. Kuznetsov, M. Greenfield, Y. Mehta, W. Merchan-Merchan, G. Salkar,A.J.A.e. Saveliev. Increasing the solar cell power output by coating with transition metal-oxide nanorods, 88 (2011) 4218-4221.
77. F.C.J.S.e.m. Krebs,s. cells. Fabrication and processing of polymer solar cells: A review of printing and coating techniques, 93 (2009) 394-412.
78. C. Girotto, B.P. Rand, J. Genoe, P.J.S.e.m. Heremans,s. cells. Exploring spray coating as a deposition technique for the fabrication of solution-processed solar cells, 93 (2009) 454-458.
79. D. Zhao, T. Liu, J.G. Park, M. Zhang, J.-M. Chen,B.J.M.E. Wang. Conductivity enhancement of aerosol-jet printed electronics by using silver nanoparticles ink with carbon nanotubes, 96 (2012) 71-75.
80. J.A. Paulsen, M. Renn, K. Christenson,R. Plourde. *Printing conformal electronics on 3D structures with Aerosol Jet technology*. in *2012 Future of Instrumentation International Workshop (FIIW) Proceedings*. 2012. IEEE.
81. S. Matthews,B. James. Review of thermal spray coating applications in the steel industry: part 1—hardware in steel making to the continuous annealing process, Journal of thermal spray technology. 19 (2010) 1267-1276.
82. A. Moridi, S.M. Hassani-Gangaraj, M. Guagliano,M.J.S.E. Dao. Cold spray coating: review of material systems and future perspectives, 30 (2014) 369-395.
83. G.J.S. Barbezat,C. Technology. Advanced thermal spray technology and coating for lightweight engine blocks for the automotive industry, 200 (2005) 1990-1993.
84. P.L. Fauchais, J.V. Heberlein,M.I. Boulos, Wire arc spraying. Thermal Spray Fundamentals, Springer, 2014, pp. 577-629.
85. I. Gedzevicius,A.J.J.o.M.P.T. Valiulis. Analysis of wire arc spraying process variables on coatings properties, 175 (2006) 206-211.
86. N.T. Dinh, E. Sowade, T. Blaudeck, S. Hermann, R.D. Rodriguez, D.R. Zahn, S.E. Schulz, R.R. Baumann,O.J.C. Kanoun. High-resolution inkjet printing of conductive carbon nanotube twin lines utilizing evaporation-driven self-assembly, 96 (2016) 382-393.
87. Z. Zhang,W.J.J.o.M.C.C. Zhu. Controllable fabrication of a flexible transparent metallic grid conductor based on the coffee ring effect, 2 (2014) 9587-9591.
88. D. Bugakova, V. Slabov, E. Sergeeva, M. Zhukov, A.J.C. Vinogradov, S.A. Physicochemical,E. Aspects. Comprehensive characterization of TiO2 inks and their application for inkjet printing of microstructures, (2019) 124146.
89. T. Seifert, E. Sowade, F. Roscher, M. Wiemer, T. Gessner,R.R. Baumann. Additive manufacturing technologies compared: morphology of deposits of silver ink using inkjet and aerosol jet printing, Industrial Engineering Chemistry Research. 54 (2015) 769-779.

90. N. Wilkinson, M. Smith, R. Kay,R. Harris. A review of aerosol jet printing—a non-traditional hybrid process for micro-manufacturing, The International Journal of Advanced Manufacturing Technology. 105 (2019) 4599-4619.
91. J. Kawakita, H. Katanoda, M. Watanabe, K. Yokoyama, S.J.S. Kuroda,C. Technology. Warm Spraying: An improved spray process to deposit novel coatings, 202 (2008) 4369-4373.
92. S. Kuroda, J. Kawakita, M. Watanabe, K. Kim, R. Molak,H. Katanoda, Current status and future prospects of warm spray technology. Future Development of Thermal Spray Coatings, Elsevier, 2015, pp. 163-206.
93. R.B.J.P. Heimann,Applications. Plasma-spray coating, (1996) 2.
94. X. Cao, R. Vassen, S. Schwartz, W. Jungen, F. Tietz,D.J.J.o.t.E.C.S. Stöever. Spray-drying of ceramics for plasma-spray coating, 20 (2000) 2433-2439.
95. D. Ke, A.A. Vu, A. Bandyopadhyay,S.J.A.b. Bose. Compositionally graded doped hydroxyapatite coating on titanium using laser and plasma spray deposition for bone implants, 84 (2019) 414-423.
96. T. Watanabe, T. Sato,A.J.T.S.F. Nezu. Electrode phenomena investigation of wire arc spraying for preparation of Ti-Al intermetallic compounds, 407 (2002) 98-103.
97. L. Pawlowski, The science and engineering of thermal spray coatings. John Wiley & Sons, 2008.
98. P. Fauchais, M. Vardelle, A. Vardelle,S.J.J.o.T.S.T. Goutier. What do we know, what are the current limitations of suspension plasma spraying?, 24 (2015) 1120-1129.
99. J.R. Davis, Handbook of thermal spray technology. ASM international, 2004.
100. B. Fotovvati, N. Namdari, A.J.J.o.M. Dehghanghadikolaei,M. Processing. On coating techniques for surface protection: a review, 3 (2019) 28.
101. H.P.J.J.o.I.S. Le,Technology. Progress and trends in ink-jet printing technology, 42 (1998) 49-62.
102. J.C. Carter, R.M. Alvis, S.B. Brown, K.C. Langry, T.S. Wilson, M.T. McBride, M. Myrick, W.R. Cox, M.E. Grove, B.W.J.B. Colston,Bioelectronics. Fabricating optical fiber imaging sensors using inkjet printing technology: A pH sensor proof-of-concept, 21 (2006) 1359-1364.
103. S.C. Chang, J. Liu, J. Bharathan, Y. Yang, J. Onohara,J.J.A.M. Kido. Multicolor organic light-emitting diodes processed by hybrid inkjet printing, 11 (1999) 734-737.
104. S.-Y. Han, D.-H. Lee, G.S. Herman,C.-H.J.J.o.D.T. Chang. Inkjet-printed high mobility transparent–oxide semiconductors, 5 (2009) 520-524.
105. H.M. Haverinen, R.A. Myllylä,G.E.J.A.P.L. Jabbour. Inkjet printing of light emitting quantum dots, 94 (2009) 073108.
106. H.M. Haverinen, R.A. Myllyla,G.E.J.J.o.d.t. Jabbour. Inkjet printed RGB quantum dot-hybrid LED, 6 (2010) 87-89.
107. T. Kawase, T. Shimoda, C. Newsome, H. Sirringhaus,R.H.J.T.s.f. Friend. Inkjet printing of polymer thin film transistors, 438 (2003) 279-287.
108. J. Ebert, E. Özkol, A. Zeichner, K. Uibel, Ö. Weiss, U. Koops, R. Telle,H.J.J.o.d.r. Fischer. Direct inkjet printing of dental prostheses made of zirconia, 88 (2009) 673-676.

109. X. Cui, T. Boland, D. DD'Lima, M.J.R.p.o.d.d. K Lotz,formulation. Thermal inkjet printing in tissue engineering and regenerative medicine, 6 (2012) 149-155.
110. T. Boland, T. Xu, B. Damon,X.J.B.J.H.N.T. Cui. Application of inkjet printing to tissue engineering, 1 (2006) 910-917.
111. V.X. Nguyen,K.J.J.P.R.L. Stebe. Patterning of small particles by a surfactant-enhanced Marangoni-Bénard instability, 88 (2002) 164501.
112. C. Seo, D. Jang, J. Chae,S.J.S.r. Shin. Altering the coffee-ring effect by adding a surfactant-like viscous polymer solution, 7 (2017) 500.
113. M. Dicuangco, S. Dash, J.A. Weibel,S.V.J.A.P.L. Garimella. Effect of superhydrophobic surface morphology on evaporative deposition patterns, 104 (2014) 201604.
114. L. Cui, J. Zhang, X. Zhang, Y. Li, Z. Wang, H. Gao, T. Wang, S. Zhu, H. Yu,B.J.S.M. Yang. Avoiding coffee ring structure based on hydrophobic silicon pillar arrays during single-drop evaporation, 8 (2012) 10448-10456.
115. D. Mampallil, H. Eral, D. Van Den Ende,F.J.S.M. Mugele. Control of evaporating complex fluids through electrowetting, 8 (2012) 10614-10617.
116. D. Mampallil, J. Reboud, R. Wilson, D. Wylie, D.R. Klug,J.M.J.S.m. Cooper. Acoustic suppression of the coffee-ring effect, 11 (2015) 7207-7213.
117. D. Mampallil, H.B.J.A.i.c. Eral,i. science. A review on suppression and utilization of the coffee-ring effect, 252 (2018) 38-54.
118. M. Hedges,A.B. Marin. *3D Aerosol jet printing-Adding electronics functionality to RP/RM*. in *DDMC 2012 conference*. 2012.
119. N.A. Azarova, J.W. Owen, C.A. McLellan, M.A. Grimminger, E.K. Chapman, J.E. Anthony,O.D. Jurchescu. Fabrication of organic thin-film transistors by spray-deposition for low-cost, large-area electronics, Organic Electronics. 11 (2010) 1960-1965. https://doi.org/10.1016/j.orgel.2010.09.008.
120. P. Sarobol, A. Cook, P.G. Clem, D. Keicher, D. Hirschfeld, A.C. Hall,N.S. Bell. Additive manufacturing of hybrid circuits, Annual Review of Materials Research. 46 (2016) 41-62.
121. E. Jabari,E.J.C. Toyserkani. Micro-scale aerosol-jet printing of graphene interconnects, Carbon. 91 (2015) 321-329.
122. C. Goth, S. Putzo,J. Franke. *Aerosol Jet printing on rapid prototyping materials for fine pitch electronic applications*. in *2011 IEEE 61st Electronic Components and Technology Conference (ECTC)*. 2011. IEEE.
123. E.B. Secor. Principles of aerosol jet printing, Flexible and Printed Electronics. 3 (2018) 035002.
124. G. Yu, J. Li, J. Zhao, L. Yue, X. Chang,C. Sung. An experimental study of kerosene combustion in a supersonic model combustor using effervescent atomization, Proceedings of the Combustion Institute. 30 (2005) 2859-2866. https://doi.org/10.1016/j.proci.2004.07.050.
125. X. Li,C. Wang. Engineering nanostructured anodes via electrostatic spray deposition for high performance lithium ion battery application, Journal of Materials Chemistry A. 1 (2013) 165-182. https://doi.org/10.1039/c2ta00437b.

126. X. Hou,K.L. Choy. Processing and Applications of Aerosol-Assisted Chemical Vapor Deposition, Chemical vapor deposition. 12 (2006) 583-596. https://doi.org/10.1002/cvde.200600033.
127. G. Della Porta, C. De Vittori,E. Reverchon. Supercritical assisted atomization: a novel technology for microparticles preparation of an asthma-controlling drug, Aaps Pharmscitech 6(2005) E421-E428. https://doi.org/10.1208/pt060352.
128. S. Leroux, C. Dumouchel, M.J.A. Ledoux,sprays. The stability curve of Newtonian liquid jets, Atomization. 6 (1996).
129. D. Guildenbecher, C. López-Rivera,P.J.E.i.F. Sojka. Secondary atomization, Experiments in Fluids. 46 (2009) 371.
130. A.H. Lefebvre. Energy considerations in twin-fluid atomization, Journal of Engineering for Gas Turbines and Power 114 (1992) 89-96.
131. T. Roesler, A.J.I.J.o.T. Lefebvre,J. Engines. Studies on aerated-liquid atomization, 6 (1989) 221-230.
132. D. Ju, X. Jia, Z. Huang, X. Qiao, J. Xiao,Z.J.F. Huang. Comparison of atomization characteristics of model exhaust gas dissolved diesel and gasoline, Fuel. 182 (2016) 928-934.
133. E. Sher, T. Bar-Kohany, A.J.P.i.e. Rashkovan,c. science. Flash-boiling atomization, 34 (2008) 417-439.
134. D.C. Huffman, *Internal mix air atomizing spray nozzle*. 1998, Google Patents.
135. R.B. Myers, R.T. Bailey, D.R. Burley, S. Feeney, B.J. Gray,D.W. Johnson, *Extended wear life low pressure drop right angle single exit orifice dual-fluid atomizer with replaceable wear materials*. 1996, Google Patents.
136. P.D. Hede, P. Bach,A.D.J.C.E.S. Jensen. Two-fluid spray atomisation and pneumatic nozzles for fluid bed coating/agglomeration purposes: A review, Chemical Engineering Science. 63 (2008) 3821-3842.
137. A.H. Lefebvre,V.G. McDonell, Atomization and sprays. CRC press, 2017.
138. J.T.J.J.P.S.T. Joshi. A review on micronization techniques, Pharmaceutical Sci Technol. 3 (2011) 651-681.
139. L. Stabile, C.V. Trassierra, G. Dell'Agli, G.J.A. Buonanno,A.Q. Research. Ultrafine particle generation through atomization technique: the influence of the solution, 13 (2013) 1667-1677.
140. Z. Huang, S. Yiming, S. Shiga, H. Nakamura, T.J.A. Karasawa,Sprays. The orifice flow pattern, pressure characteristics, and their effects on the atomization of fuel containing dissolved gas, Atomization and Sprays. 4 (1994). https://doi.org/10.1615/AtomizSpr.v4.i2.10.
141. J.W. Tom,P.G. Debenedetti. Particle formation with supercritical fluids—a review, Journal of Aerosol Science. 22 (1991) 555-584. https://doi.org/10.1016/0021-8502(91)90013-8.
142. C. Costa, T. Casimiro,A. Aguiar-Ricardo. Optimization of supercritical CO2-assisted atomization: phase behavior and design of experiments, Journal of Chemical Engineering Data. 63 (2018) 885-896.

143. J.W. Tom,P.G. Debenedetti. Formation of bioerodible polymeric microspheres and microparticles by rapid expansion of supercritical solutions, Biotechnology progress. 7 (1991) 403-411. https://doi.org/10.1021/bp00011a004.
144. R. Sievers. Formation of aqueous small droplet aerosols assisted by supercritical carbon dioxide, Aerosol Science and Technology. 30 (1999) 3-15.
145. E. Reverchon, *Process for the production of micro and/or nano particles*. 2007, Google Patents.
146. E. Reverchon,G. Della Porta. Micronization of antibiotics by supercritical assisted atomization, The Journal of supercritical fluids. 26 (2003) 243-252. https://doi.org/10.1016/S0896-8446(02)00162-6.
147. E. Reverchon. Supercritical-assisted atomization to produce micro-and/or nanoparticles of controlled size and distribution, Industrial engineering & chemistry research. 41 (2002) 2405-2411. https://doi.org/10.1021/ie010943k.
148. H.-B. Xiong, J. Lin,Z.-F. Zhu. Three-dimensional simulation of effervescent atomization spray, Atomization Sprays. 19 (2009). https://doi.org/10.1615/AtomizSpr.v19.i1.50.
149. Z. Huang, Y. Shao, S. Shiga,H. Nakamura. Controlling mechanism and resulting spray characteristics of injection of fuel containing dissolved gas, Journal of Thermal Science. 3 (1994) 191-199. https://doi.org/10.1007/BF02653122.
150. X. Jiang, G. Siamas, K. Jagus,T. Karayiannis. Physical modelling and advanced simulations of gas–liquid two-phase jet flows in atomization and sprays, Progress in energy combustion science. 36 (2010) 131-167. https://doi.org/10.1016/j.pecs.2009.09.002.
151. K. Pougatch, M. Salcudean, E. Chan,B. Knapper. A two-fluid model of gas-assisted atomization including flow through the nozzle, phase inversion, and spray dispersion, International Journal of Multiphase Flow. 35 (2009) 661-675. https://doi.org/10.1016/j.ijmultiphaseflow.2009.03.001.
152. D.C.K. Rao, S. Karmakar,S.J.S.R. Basu. Atomization characteristics and instabilities in the combustion of multi-component fuel droplets with high volatility differential, 7 (2017) 1-15.
153. G. Caputo, S. Liparoti, R. Adami, E.J.I. Reverchon,e.c. research. Use of supercritical CO2 and N2 as dissolved gases for the atomization of ethanol and water, Industrial engineering chemistry research. 51 (2012) 11803-11808.
154. L. Qian, J. Lin,H.J.J.o.t.s.t. Xiong. A fitting formula for predicting droplet mean diameter for various liquid in effervescent atomization spray, 19 (2010) 586-601.
155. H. Simmons. The prediction of Sauter mean diameter for gas turbine fuel nozzles of different types, (1980).
156. M. Lund, P.E. Sojka, A.H. Lefebvre,P. Gosselin. Effervescent atomization at low mass flow rates. Part I: The influence of surface tension, Atomization Sprays. 3 (1993). https://doi.org/10.1615/AtomizSpr.v3.i1.40.
157. C.J.Z.A.M.M. Weber. Disintegration of liquid jets, 1 (1931) 136-159.
158. J. Sutherland, P.E. Sojka,M.W. Plesniak. Ligament-controlled effervescent atomization, Atomization Sprays. 7 (1997). https://doi.org/10.1615/AtomizSpr.v7.i4.40.
159. A.M. Sterling,C.J.J.o.F.M. Sleicher. The instability of capillary jets, 68 (1975) 477-495.

160. J. Lin, L. Qian,H.J.P.t. Xiong. Relationship between deposition properties and operating parameters for droplet onto surface in the atomization impinging spray, 191 (2009) 340-348.
161. J.B. Mooney,S.B.J.A.r.o.m.s. Radding. Spray pyrolysis processing, 12 (1982) 81-101.
162. R. Vehring, W.R. Foss,D.J.J.o.A.S. Lechuga-Ballesteros. Particle formation in spray drying, 38 (2007) 728-746.
163. K. Sollohub,K.J.J.o.p.s. Cal. Spray drying technique: II. Current applications in pharmaceutical technology, 99 (2010) 587-597.
164. J. Raula, H. Eerikäinen,E.I.J.I.j.o.p. Kauppinen. Influence of the solvent composition on the aerosol synthesis of pharmaceutical polymer nanoparticles, 284 (2004) 13-21.
165. Y. Wei, Y.-H. Huang, K.-C. Cheng,Y.-L.J.S.R. Song. Investigations of the Influences of Processing Conditions on the Properties of Spray Dried Chitosan-Tripolyphosphate Particles loaded with theophylline, 10 (2020) 1-12.
166. E.J.I. Reverchon,e.c. research. Supercritical-assisted atomization to produce micro-and/or nanoparticles of controlled size and distribution, 41 (2002) 2405-2411.
167. R.J. Moon, A. Martini, J. Nairn, J. Simonsen,J. Youngblood. Cellulose nanomaterials review: structure, properties and nanocomposites, Chemical Society Reviews. 40 (2011) 3941-3994.
168. F. Hansen, V. Brun, E. Keller, T. Wegner, M. Meador,L. Friedersdorf. Cellulose nanomaterials—a path towards commercialization workshop report, (2014).
169. L. Peponi, D. Puglia, L. Torre, L. Valentini, J.M.J.M.S. Kenny,E.R. Reports. Processing of nanostructured polymers and advanced polymeric based nanocomposites, 85 (2014) 1-46.
170. F.M. De Sciarra,P. Russo, Experimental Characterization, Predictive Mechanical and Thermal Modeling of Nanostructures and Their Polymer Composites. William Andrew, 2018.
171. J. Taylor,J.J.E.i.F. Hoyt. Water jet photography—techniques and methods, 1 (1983) 113-120.
172. R.P. Benedict, Fundamentals of temperature, pressure, and flow measurements. John Wiley & Sons, 1984.
173. J. Swithenbank, J. Beer, D. Taylor, D. Abbot,G. McCreath. *A laser diagnostic technique for the measurement of droplet and particle size distribution*. in *14th aerospace sciences meeting*. 1976.
174. K.F. Maassen, F. Poursadegh,C.L. Genzale. *Spectral Microscopy Imaging System for High-Resolution and High-Speed Imaging of Fuel Sprays*. in *Internal Combustion Engine Division Fall Technical Conference*. 2019. American Society of Mechanical Engineers.
175. V. Kirsch, M. Reddemann, J. Palmer,R. Kneer. *Zooming into primary breakup mechanisms of high-pressure automotive sprays*. in *Ilass Europe. 28th european conference on Liquid Atomization and Spray Systems*. 2017. Editorial Universitat Politècnica de València.
176. S. Shariatnia, A. Veldanda, S. Obeidat, D. Jarrahbashi,A. Asadi. Atomization of cellulose nanocrystals aqueous suspensions in fused deposition modeling: A scalable technique to improve the strength of 3D printed polymers, Composites Part B: Engineering. 177 (2019). https://doi.org/10.1016/j.compositesb.2019.107291.

177. C.J.E.i.f. Dumouchel. On the experimental investigation on primary atomization of liquid streams, 45 (2008) 371-422.
178. S. Shafiei-Sabet, W. Hamad,S.J.C. Hatzikiriakos. Ionic strength effects on the microstructure and shear rheology of cellulose nanocrystal suspensions, 21 (2014) 3347-3359.
179. M. Bercea,P. Navard. Shear Dynamics of Aqueous Suspensions of Cellulose Whiskers, Macromolecules. 33 (2000) 6011-6016. https://doi.org/10.1021/ma000417p.
180. S. Shafiei-Sabet, W.Y. Hamad,S.G.J.L. Hatzikiriakos. Rheology of nanocrystalline cellulose aqueous suspensions, 28 (2012) 17124-17133.
181. B.D. Miller, *Digital Holographic Diagnositcs of Aerated-liquid Jets in a Subsonic Crossflow*. 2006, Oklahoma State University.
182. N. Yildirim,S.J.M. Shaler. A study on thermal and nanomechanical performance of cellulose nanomaterials (CNs), 10 (2017) 718.
183. M. Suzuki, C.A.J.P.D. Wilkie,Stability. The thermal degradation of acrylonitrile-butadiene-styrene terpolymei as studied by TGA/FTIR, 47 (1995) 217-221.
184. C. Miao,W.Y.J.C. Hamad. Cellulose reinforced polymer composites and nanocomposites: a critical review, 20 (2013) 2221-2262.
185. L. Ma, Y. Zhang, Y. Meng, P. Anusonti-Inthra,S. Wang. Preparing cellulose nanocrystal/acrylonitrile-butadiene-styrene nanocomposites using the master-batch method, Carbohydrate Polymers. 125 (2015) 352-359. https://doi.org/https://doi.org/10.1016/j.carbpol.2015.02.062.
186. E. Haque, S. Shariatnia, T.-J. Jeong, D. Jarrahbashi, A. Asadi, T. Harris, R.J. Moon,K. Kalaitzidou. Scalable coating methods for enhancing glass fiber–epoxy interactions with cellulose nanocrystals, Cellulose. (2021) 1-16.
187. S. Shariatnia, A. Asadi,D. Jarrahbashi. Experimental analysis of supercritical-assisted atomization, Physics of Fluids. 33 (2021) 013314.
188. L.W. Diamond,N.N.J.F.p.e. Akinfiev. Solubility of CO2 in water from− 1.5 to 100 C and from 0.1 to 100 MPa: evaluation of literature data and thermodynamic modelling, 208 (2003) 265-290.
189. R. Sun, W. Hu,Z.J.J.o.s.c. Duan. Prediction of nitrogen solubility in pure water and aqueous NaCl solutions up to high temperature, pressure, and ionic strength, 30 (2001) 561-573.
190. G. Lorenzetto,A.H.J.A.j. Lefebvre. Measurements of drop size on a plain-jet airblast atomizer, 15 (1977) 1006-1010.
191. F. Tewes,F.J.T.J.o.P.C.B. Boury. Formation and Rheological Properties of the Supercritical CO2− Water Pure Interface, 109 (2005) 3990-3997.
192. S. Bachu, D.B.J.J.o.C. Bennion,E. Data. Interfacial tension between CO2, freshwater, and brine in the range of pressure from (2 to 27) MPa, temperature from (20 to 125) C, and water salinity from (0 to 334 000) mg· L− 1, 54 (2009) 765-775.
193. P. Chiquet, J.-L. Daridon, D. Broseta, S.J.E.C. Thibeau,Management. CO2/water interfacial tensions under pressure and temperature conditions of CO2 geological storage, 48 (2007) 736-744.

194. W. Yan, G.-Y. Zhao, G.-J. Chen, T.-M.J.J.o.C. Guo,E. Data. Interfacial tension of (methane+ nitrogen)+ water and (carbon dioxide+ nitrogen)+ water systems, 46 (2001) 1544-1548.
195. M. McBride-Wright, G.C. Maitland, J.M.J.J.o.C. Trusler,E. Data. Viscosity and density of aqueous solutions of carbon dioxide at temperatures from (274 to 449) K and at pressures up to 100 MPa, 60 (2014) 171-180.
196. M. Zaremba, J. Kozák, M. Malý, L. Weiß, P. Rudolf, J. Jedelský,M.J.I.J.o.M.F. Jícha. An experimental analysis of the spraying processes in improved design of effervescent atomizer, 103 (2018) 1-15.
197. A. Kourmatzis, A. Lowe,A.J.J.o.E.E. Masri. Conditioned analysis of effervescent atomization, 143 (2017) 04017019.
198. D.L. Siebers, *Liquid-Phase Fuel Penetration in Diesel Sprays*. 1998, SAE International.
199. G. Faeth, L.-P. Hsiang,P.-K.J.I.J.o.M.F. Wu. Structure and breakup properties of sprays, 21 (1995) 99-127.
200. S. Sovani, P. Sojka, A.J.P.i.e. Lefebvre,c. science. Effervescent atomization, 27 (2001) 483-521.
201. J. Sauter, Die Grössenbestimmung der im Gemischnebel von Verbrennungskraftmaschinen vorhandenen Brennstoffteilchen:(Mitteilung aus d. Labor. f. techn. Physik d. Techn. Hochsch. München); mit 26 Abb. u. 8 Zahlentaf. VDI-Verlag, 1926.
202. M. Prokop,R.J.R.A.E. Kejklicek. Effect of adjuvants on spray droplet size of water, 48 (2002) 144-148.
203. G.I.J.P.o.t.R.S.o.L.S.A.M. Taylor,P. Sciences. The instability of liquid surfaces when accelerated in a direction perpendicular to their planes. I, 201 (1950) 192-196.
204. R. Bellman,R.H.J.Q.o.A.M. Pennington. Effects of surface tension and viscosity on Taylor instability, 12 (1954) 151-162.
205. J.C. Beale, R.D.J.A. Reitz,sprays. Modeling spray atomization with the Kelvin-Helmholtz/Rayleigh-Taylor hybrid model, 9 (1999).
206. L. Rayleigh, *On the instability of jets Proc. of the London Math*. 1878, Soc.
207. S. Chandrasekhar, Hydrodynamic and hydromagnetic stability. Courier Corporation, 2013.
208. D.D. Joseph, J. Belanger,G.J.I.J.o.M.F. Beavers. Breakup of a liquid drop suddenly exposed to a high-speed airstream, 25 (1999) 1263-1303.
209. D. Jarrahbashi,W.A. Sirignano. Vorticity dynamics for transient high-pressure liquid injection, Physics of Fluids. 26 (2014) 101304. https://doi.org/10.1063/1.4895781.
210. P. Marmottant,E.J.J.o.f.m. Villermaux. On spray formation, 498 (2004) 73-111.
211. D.G. Bonett,T.A.J.P. Wright. Sample size requirements for estimating Pearson, Kendall and Spearman correlations, 65 (2000) 23-28.
212. J. Hauke,T.J.Q.g. Kossowski. Comparison of values of Pearson's and Spearman's correlation coefficients on the same sets of data, 30 (2011) 87-93.
213. J.H.J.A.o.s. Friedman. Greedy function approximation: a gradient boosting machine, (2001) 1189-1232.
214. J.H.J.C.s. Friedman,d. analysis. Stochastic gradient boosting, 38 (2002) 367-378.
215. D. Nielsen, *Tree boosting with xgboost-why does xgboost win" every" machine learning competition?* 2016, NTNU.

216. T. Chen,C. Guestrin. *Xgboost: A scalable tree boosting system*. in *Proceedings of the 22nd acm sigkdd international conference on knowledge discovery and data mining*. 2016.
217. C.J.U.h.w.c.n.e.h.v.t.M.b.s.g.b.p. Li. A gentle introduction to gradient boosting, (2016).
218. T. Chen, T. He, M. Benesty, V. Khotilovich,Y.J.R.p.v.-. Tang. Xgboost: extreme gradient boosting, (2015) 1-4.
219. L.-P. Hsiang,G.J.I.J.o.M.F. Faeth. Drop deformation and breakup due to shock wave and steady disturbances, 21 (1995) 545-560.
220. D. Jarrahbashi, W.A. Sirignano, P.P. Popov,F. Hussain. Early spray development at high gas density: hole, ligament and bridge formations, Journal of Fluid Mechanics. 792 (2016) 186-231. https://doi.org/10.1017/jfm.2016.71.
221. D. Guildenbecher, C. López-Rivera,P.J.E.i.F. Sojka. Secondary atomization, 46 (2009) 371.
222. C. Chryssakis, D.N. Assanis,C. Bae, *Development and validation of a comprehensive CFD model of diesel spray atomization accounting for high Weber numbers*. 2006, SAE Technical Paper.
223. C. Chryssakis, D.N.J.A. Assanis,Sprays. A unified fuel spray breakup model for internal combustion engine applications, 18 (2008).
224. F. Tewes,F. Boury. Formation and Rheological Properties of the Supercritical CO2− Water Pure Interface, The Journal of Physical Chemistry B. 109 (2005) 3990-3997. https://doi.org/10.1021/jp046019w.
225. S. Bachu,D.B. Bennion. Interfacial tension between CO2, freshwater, and brine in the range of pressure from (2 to 27) MPa, temperature from (20 to 125) C, and water salinity from (0 to 334 000) mg· L− 1, Journal of Chemical Engineering Data. 54 (2009) 765-775. https://doi.org/10.1021/je800529x.
226. L. Bouse, I. Kirk,L. Bode. Effect of spray mixture on droplet size, Transactions of the ASAE. 33 (1990) 783-0788.
227. P. Dayal, M.S. Shaik,M. Singh. Evaluation of different parameters that affect droplet-size distribution from nasal sprays using the Malvern Spraytec®, Journal of pharmaceutical sciences. 93 (2004) 1725-1742.
228. L. Govor, G. Reiter, G. Bauer,J. Parisi. Nanoparticle ring formation in evaporating micron-size droplets, Applied physics letters. 84 (2004) 4774-4776.
229. G. Lu, H. Hu, Y. Duan,Y. Sun. Wetting kinetics of water nano-droplet containing non-surfactant nanoparticles: A molecular dynamics study, Applied Physics Letters. 103 (2013) 253104.
230. R. Vehring. Pharmaceutical particle engineering via spray drying, Pharmaceutical research. 25 (2008) 999-1022.
231. Y. Wei. Effect of particles on evaporation of droplet containing particles, (2015).
232. D. Mampallil,H.B. Eral. A review on suppression and utilization of the coffee-ring effect, Adv Colloid Interface Sci. 252 (2018) 38-54. https://doi.org/10.1016/j.cis.2017.12.008.
233. H. Hu,R.G. Larson. Evaporation of a sessile droplet on a substrate, The Journal of Physical Chemistry B. 106 (2002) 1334-1344.
234. T.A. Nguyen,A.V. Nguyen. Increased evaporation kinetics of sessile droplets by using nanoparticles, Langmuir. 28 (2012) 16725-16728.

235. H. Hu,R.G. Larson. Analysis of the microfluid flow in an evaporating sessile droplet, Langmuir. 21 (2005) 3963-3971.
236. R. Weast,M.J.C. Astle, Boca Raton, Fla. CRC Handbook of chemistry and physics 62nd ed, (1981).
237. J. Van Rie, C. Schütz, A. Gençer, S. Lombardo, U. Gasser, S. Kumar, G.n. Salazar-Alvarez, K. Kang,W. Thielemans. Anisotropic diffusion and phase behavior of cellulose nanocrystal suspensions, Langmuir. 35 (2019) 2289-2302.
238. R.D. Deegan, O. Bakajin, T.F. Dupont, G. Huber, S.R. Nagel,T.A.J.N. Witten. Capillary flow as the cause of ring stains from dried liquid drops, 389 (1997) 827.
239. J. Xu, J. Xia, S.W. Hong, Z. Lin, F. Qiu,Y.J.P.r.l. Yang. Self-assembly of gradient concentric rings via solvent evaporation from a capillary bridge, 96 (2006) 066104.
240. S. Shariatnia, A.V. Kumar, O. Kaynan,A. Asadi. Hybrid Cellulose Nanocrystals-Bonded Carbon Nanotubes/Carbon Fiber Polymer Composites for Structural Applications, ACS Applied Nano Materials. (2020).
241. S. Shariatnia, A.V. Kumar, O. Kaynan,A. Asadi. Hybrid Cellulose Nanocrystal-Bonded Carbon Nanotubes/Carbon Fiber Polymer Composites for Structural Applications, ACS Applied Nano Materials. (2020). https://doi.org/10.1021/acsanm.0c00785.
242. V. Khoshkava,M.R. Kamal. Effect of drying conditions on cellulose nanocrystal (CNC) agglomerate porosity and dispersibility in polymer nanocomposites, Powder Technology. 261 (2014) 288-298. https://doi.org/https://doi.org/10.1016/j.powtec.2014.04.016.
243. A. Shahi,E. Arunan. Why are Hydrogen Bonds Directional?, Journal of Chemical Sciences. 128 (2016) 1571-1577. https://doi.org/10.1007/s12039-016-1156-3.
244. Y. Zhou, P. Wu, Z. Cheng, J. Ingram,S. Jeelani. Improvement in electrical, thermal and mechanical properties of epoxy by filling carbon nanotube, Express polymer letters. 2 (2008) 40-48. https://doi.org/10.3144/expresspolymlett.2008.6.
245. C. Zhi, Y. Bando, T. Terao, C. Tang, H. Kuwahara,D. Golberg. Towards thermoconductive, electrically insulating polymeric composites with boron nitride nanotubes as fillers, Advanced Functional Materials. 19 (2009) 1857-1862. https://doi.org/10.1002/adfm.200801435.
246. S. Chandrasekaran, C. Seidel,K. Schulte. Preparation and characterization of graphite nano-platelet (GNP)/epoxy nano-composite: Mechanical, electrical and thermal properties, European Polymer Journal. 49 (2013) 3878-3888. https://doi.org/10.1016/j.eurpolymj.2013.10.008.
247. P.B. Agarwal, R. Sharma, D. Mishra, N.K. Thakur, A. Agarwal, A.J.A.A.M. Ajayaghosh,Interfaces. Silicon Shadow Mask Technology for Aligning and In Situ Sorting of Semiconducting SWNTs for Sensitivity Enhancement: A Case Study of NO2 Gas Sensor, 12 (2020) 40901-40909.
248. L. Lei, A.R. Gamboa, C. Kuznetsova, S. Littlecreek, J. Wang, Q. Zou, J.D. Zahn,J.P.J.S.r. Singer. Self-limiting electrospray deposition on polymer templates, 10 (2020) 1-9.